Extensional Rheology and Electric Field Control: Strategies for Electrospinning Scale-Up

by

Étienne BEAUDOIN

MANUSCRIPT-BASED THESIS PRESENTED TO ÉCOLE DE TECHNOLOGIE SUPÉRIEURE IN PARTIAL FULFILLEMENT FOR THE DEGREE OF DOCTOR OF PHILOSOPHY
PH. D.

MONTREAL, NOVEMBER 20, 2025.

ÉCOLE DE TECHNOLOGIE SUPÉRIEURE
UNIVERSITÉ DU QUÉBEC

BOARD OF EXAMINERS

THIS THESIS HAS BEEN EVALUATED

BY THE FOLLOWING BOARD OF EXAMINERS

Mrs. Nicole R. Demarquette, thesis supervisor
Mechanical Engineering Department at École de technologie supérieure

Mr. Ricardo J. Zednik, co-supervisor
Mechanical Engineering Department at École de technologie supérieure

Mrs. Marlène Sanjosé, president of the board of examiners
Aerospace Engineering Department at École de technologie supérieure

Mr. Éric David, member of the jury
Mechanical Engineering Department at École de technologie supérieure

Mr. Jean-Marie Raquez, external evaluator
Chemical Engineering Department at Polytechnique Montréal

THIS THESIS WAS PRESENTED AND DEFENDED

IN THE PRESENCE OF BOARD OF EXAMINERS AND PUBLIC

ON NOVEMBER 10, 2025

AT ÉCOLE DE TECHNOLOGIE SUPÉRIEURE

ACKNOWLEDGMENTS

I would like to deeply thank everyone who helped me in this journey.

I would first like to express my sincere gratitude to Prof. Nicole R. Demarquette, who offered me the opportunity to pursue research under her supervision. Her guidance, trust, and support made this journey possible. I am also thankful to my co-supervisor, Prof. Ricardo Zednik, for his advice and encouragement throughout this work, and to Mazen Samara, for his wise comments, insightful questions, and motivating support.

I would like to acknowledge the members of my jury, Prof. Marlène Sanjosé, Prof. Éric David, and Prof. Jean-Marie Raquez, for their time, feedback, and valuable perspectives on this thesis.

My thanks also go to the researchers and technical staff who facilitated my work. I am especially grateful to Nabil, Claude-Daniel, and Michel, as well as to all the staff of the Department of Mechanical Engineering at ÉTS for their invaluable support.

I also acknowledge the use of ChatGPT (OpenAI) to assist with grammar correction, language polishing, and rephrasing during the preparation of this manuscript (any remaining mistakes are, of course, mine).

I would also like to thank my colleagues and friends, whose stimulating conversations and welcome distractions kept me grounded along the way. I am especially grateful to my life partner, Daria, whose constant support, encouragement, and steadfast presence have been my anchor. I am also thankful to Mauricio, Atefe, Chloé, and Manon, whose humor and companionship at ÉTS brought lightness to the most demanding days of research. Finally, I am deeply thankful to François, Nicolas, Matt, and Marie-Pierre, whose friendship brought joy and balance to my life throughout these years.

Above all, I wish to express my deepest gratitude to my family. To my father, whose confidence in me never wavered and whose constant support has always been a guiding presence. To my mother, whose love and values continues to accompany me and shape who I am, and to my brother and sister for their unconditional support. Most importantly, to my son, whose love, resilience, and joy give meaning to everything I do. May you always find strength in your uniqueness, this work is dedicated to you.

RHÉOLOGIE EN EXTENSION ET CONTRÔLE DU CHAMP ÉLECTRIQUE : STRATÉGIES POUR LA MISE À L'ÉCHELLE DE L'ÉLECTROFILAGE

Étienne BEAUDOIN

RESUMÉ

Les nanofibres polymériques connaissent un intérêt croissant pour la filtration, les capteurs et les applications biomédicales. L'électrofilage constitue une méthode polyvalente pour produire de telles fibres avec une morphologie contrôlée, mais son passage à des échelles de production plus larges demeure limité par une productivité intrinsèquement faible. Une simple augmentation du débit d'alimentation entraîne une dégradation de la morphologie des fibres, ce qui montre que la mise à l'échelle exige de nouvelles stratégies. Cette thèse s'attaque à deux défis majeurs : l'adaptation des propriétés rhéologiques des solutions polymériques afin d'optimiser la formation des fibres, et la réduction des non-uniformités du champ électrique dans les systèmes multi-aiguilles, responsables de la déstabilisation des jets et de la baisse de qualité des fibres obtenues.

La première voie de recherche porte sur la rhéologie. Un rhéomètre à bris capillaire en extension (CaBER) a été conçu sur mesure pour caractériser des solutions viscoélastiques de faible viscosité adaptées à l'électrofilage. Des expériences menées sous humidité contrôlée, appuyées par un modèle évaporation–diffusion, ont montré que l'évaporation du solvant influence fortement la dynamique d'amincissement du filament, allongeant artificiellement le temps de relaxation mesuré par un durcissement en traction induit par l'évaporation. Des études systématiques sur la distribution des masses molaires ont révélé que la fraction de chaînes longues détermine l'élasticité en extension des solutions et la morphologie des fibres électrofilées. De plus, le « dopage élastique », obtenu par l'ajout d'une fraction infime de polymère de masse molaire élevée, a permis la formation de fibres à partir d'une matrice de faible masse molaire autrement non filable, conduisant également à un quintuplement du débit de polymère tout en préservant la qualité des fibres.

La seconde voie de recherche concerne la mise à l'échelle par électrofilage multi-aiguilles. Une configuration linéaire de vingt aiguilles a été étudiée, et des plaques parallèles utilisées comme électrodes auxiliaires ont été introduites pour homogénéiser le champ électrique. Il a été démontré par simulations par éléments finis et par expériences que cette approche stabilise les trajectoires des jets, uniformise le dépôt des fibres et permet un contrôle précis de l'épaisseur des membranes. Cette configuration a permis d'augmenter par un facteur vingt le taux de production tout en maintenant une qualité de fibres comparable à celle obtenue par électrofilage à aiguille unique.

Dans l'ensemble, ces travaux démontrent que la combinaison du contrôle rhéologique des formulations polymériques et de l'optimisation du champ électrique constitue une approche efficace pour la mise à l'échelle de la production de nanofibres. Cette recherche contribue à faire progresser l'électrofilage des études de laboratoire vers des débits compatibles avec les besoins industriels.

Mots-clés : électrofilage, nanofibres, solutions polymériques, rhéologie en extension, rhéomètre à bris capillaire en extension (CaBER)

EXTENSIONAL RHEOLOGY AND ELECTRIC FIELD CONTROL: STRATEGIES FOR ELECTROSPINNING SCALE-UP

Étienne BEAUDOIN

ABSTRACT

Polymeric nanofibers are increasingly used in filtration, sensing, and biomedical applications. Electrospinning offers a versatile route to produce such fibers with controlled morphology, but its adoption beyond the laboratory remains limited by intrinsically low productivity. Simply increasing the flow rate collapses fiber morphology, showing that scale-up requires new strategies. This thesis addresses two critical challenges: tailoring the rheological properties of polymer solutions to optimize fiber formation, and mitigating electric field non-uniformities in multi-needle systems that destabilize jets and compromise product quality.

The first research path focuses on rheology. A custom Capillary Breakup Extensional Rheometer (CaBER) was designed for low-viscosity viscoelastic solutions relevant to electrospinning. Controlled-humidity experiments and an evaporation–diffusion model revealed that solvent evaporation strongly biases filament thinning, conflating intrinsic relaxation time with evaporation-driven strain hardening. Systematic studies on molecular weight distribution showed that long-chain content governs extensional elasticity and fiber morphology. Crucially, elastic doping, with a trace fraction of high-molecular-weight polymer, enabled fiber formation from an otherwise unspinnable low-molecular-weight matrix, leading to a fivefold increase in polymer throughput while preserving fiber quality.

The second research path addresses scale-up via multi-needle electrospinning. A linear twenty-needle array was investigated, and parallel plates as auxiliary electrodes were introduced to homogenize the electric field. Finite element simulations and experiments demonstrated that this approach stabilizes jet trajectories, uniformizes fiber deposition, and enables precise control of membrane thickness. This configuration achieved a twentyfold increase in production rate while maintaining fiber quality comparable to single-needle electrospinning.

Together, these findings demonstrate that combining rheological control of solution formulations with electric field optimization provides a practical and scalable framework for

nanofiber production. This work advances electrospinning from laboratory-scale studies toward industrially relevant throughput.

Keywords: electrospinning, nanofibers, polymer solutions, extensional rheology, Capillary Breakup Extensional Rheometer (CaBER)

TABLE OF CONTENTS

Page

LIST OF TABLES

LIST OF FIGURES

Page

LIST OF ABREVIATIONS

BOM	Bill of materials
CaBER	Capillary breakup extensional rheometer
DMF	Dimethylformamide
DOS	Dripping-onto-substrate
FDM	Fused deposition modeling
MWD	Molecular weight distribution
PEG	Poly(ethylene glycol)
PEO	Poly(ethylene oxide)
PLA	Poly(lactic acid)
PDI	Polydispersity index
PVDF	Poly(vinylidene difluoride)
ROJER	Rayleigh–Ohnesorge jetting extensional rheometer
ROI	Region of interest
SBS	Solution blow spinning
SEM	Scanning electron microscopy
SRM	Slow retraction method

LIST OF SYMBOLS

Latin letters

C	Polymer concentration of solution
D	Diffusion coefficient
D	Electric displacement field
D(t)	Filament diameter as function of time
E	Electric field strength
J	Evaporation coefficient
k_g	Mass transfer coefficient
M_n	Number-average molecular weight
M_w	Weight-average molecular weight
M_1	Solvent molar mass
N_r	Number of radial nodes
P_s	Saturation vapor pressure
P_∞	Solvent vapor pressure
R	Radius of the filament
R_{mid}	Filament radius at the pinching point
R_g	Universal gas constant
RH	Relative humidity
r	Radial node
$\tilde{r}$	Normalized radial coordinate $r/R(t)$
t	Time

t_0, t_1, t_2, t_3	Characteristic times
t_c	Critical time to breakup
T	Absolute temperature
V	Electric potential

Greek Letters

α	Fitting constant
Δt	Time step
η	Viscosity
η_0	Zero-shear viscosity
η_e	Extensional viscosity
η_s	Shear viscosity
λ	Relaxation time
ρ	Solvent density
ρ_v	Volumetric charge density
σ	Surface tension
ϕ	Polymer concentration inside the filament
ϕ_0	Initial polymer concentration inside the filament

INTRODUCTION

Polymeric nanofibers have attracted increasing attention over the past few decades owing to their high surface area, tunable porosity, and versatility in applications ranging from biomedical scaffolds and sensors to advanced membranes for air and water filtration. Among the various processing methods, electrospinning has become the most widely adopted technique because it offers fine control over fiber morphology and material composition. However, electrospinning in its conventional single-needle configuration is inherently limited by very low production rates, typically on the order of 0.01–2 g/h. This low throughput, combined with the sensitivity of fiber morphology to operating parameters such as solution flow rate, has restricted electrospinning to laboratory-scale applications and hindered its industrial adoption. Scaling up electrospinning therefore requires more than simply increasing flow rates: it demands a deeper understanding of the physical mechanisms governing fiber formation and new strategies to maintain product quality at higher yields.

The stability and continuity of the electrospun jet are strongly influenced not only by processing parameters but also by the extensional rheology of the polymer solution, which dictates how the fluid resists stretching during jet formation. Because electrospinning involves predominantly extensional rather than shear flows, understanding this behavior is essential for predicting and controlling fiber morphology, especially as production rates are increased during scale-up. However, extensional properties are far more challenging to measure than shear viscosity, particularly for the low-viscosity and often volatile polymer solutions used in electrospinning. Capillary Breakup Extensional Rheometry (CaBER) provides a direct means of probing filament thinning dynamics, yet its application to electrospinning-relevant solutions is hindered by several limitations: the lack of commercially available instruments, the susceptibility of measurements to artifacts arising from solvent evaporation, and the complex influence of molecular weight distribution and long-chain content on extensional rheological properties.

On the processing side, one of the most direct routes to increasing throughput is the use of multi-needle systems. In principle, this approach retains the versatility of single-needle electrospinning while scaling production linearly with the number of needles. In practice, however, electric field interference between adjacent jets results in non-uniform field distributions, jet deflections, and variations in fiber morphology and membrane thickness. Without effective control of the electric field, multi-needle electrospinning cannot deliver reliable fiber quality, which limits its broader use.

This thesis addresses these two bottlenecks by combining solution rheology with process engineering. On the rheology side, the work begins with the design and construction of a custom Capillary Breakup Extensional Rheometer (CaBER) tailored to the low-viscosity viscoelastic solutions typical of electrospinning. The methodology is then refined through controlled-environment experiments and evaporation–diffusion modeling, which make it possible to decouple intrinsic material properties from evaporation-driven artifacts. Finally, the influence of molecular weight distribution and long-chain content is systematically investigated to show how formulation, through elastic doping and blend design, can be tuned to enable fiber formation at higher polymer throughput. On the processing side, the thesis targets the scale-up of electrospinning by mitigating electric-field non-uniformities in multi-needle arrays. The conception and implementation of auxiliary electrodes is introduced and validated through finite-element simulations and experiments, demonstrating stabilized jet trajectories and uniform fiber deposition. Together, these advances provide an integrated framework for scaling up electrospinning while maintaining control over fiber morphology and product quality.

Following this introduction, Chapter 1 provides the literature review, covering the background on nanofibers, electrospinning, and extensional rheology using CaBER, and presents the state of the art relevant to each of the research themes developed in the thesis. Chapter 2 defines the main and specific objectives, while Chapter 3 details the general methodology, including materials, processing, and characterization techniques. Chapters 4 through 7 present the research contributions: (4) the design of a custom CaBER device, (5) controlled-environment

CaBER and evaporation modeling, (6) the influence of polymer formulation and elastic doping on electrospinnability, and (7) the optimization of electric field uniformity in multi-needle arrays. The thesis concludes with a general discussion and perspectives for scalable nanofiber production.

CHAPTER 1

LITTERATURE REVIEW

In this chapter, the Background section introduces the fundamental concepts necessary for understanding this thesis, namely nanofiber materials, the electrospinning process and its parameters, and the principles of Capillary Breakup Extensional Rheometry (CaBER). Building on this foundation, the State of the Art section examines four research areas that correspond directly to the themes developed in the subsequent research chapters: (1) the design and operation of CaBER instruments, (2) the influence of controlled environments and solvent evaporation during CaBER experiments, (3) the impact of molecular weight distribution and long-chain content on the extensional rheology and electrospinnability of polymer solutions, and (4) strategies for scaling up electrospinning, with a focus on mitigating electric field non-uniformities in multi-needle systems.

1.1 Background

1.1.1 Nanofibers

Fibers are elongated structures characterized by a high aspect ratio, with lengths much greater than their diameters. When assembled, they can be woven, knitted, braided, or, if bonded without weaving, formed into nonwoven fabrics. Nonwovens are webs of fibers consolidated through mechanical entanglement, thermal bonding, or chemical bonding, without the regular interlacing found in woven textiles. In most cases, the fibers are randomly oriented within the web. This structure gives nonwovens a combination of controlled porosity, surface functionality, and mechanical compliance, enabling their use in applications such as filtration media, hygiene products, medical textiles, and protective clothing.

The modern nonwovens industry emerged in the mid-twentieth century, when the term “nonwovens” (*Vliesstoffe*) began to be adopted by European manufacturers (Albrecht, Fuchs,

& Kittelmann, 2003; Russell, 2007). Since then, production capacity has expanded rapidly, with nonwovens becoming essential to healthcare products, geotextiles, filtration systems, automotive components, packaging, and many other sectors. In all these applications, the choice of the fibrous form is motivated by its porosity, surface characteristics, and mechanical properties.

Historically, fibers were derived exclusively from natural materials such as cotton, linen, silk, and wool, each with advantages and limitations (Russell, 2007; Yarin, Pourdeyhimi, & Ramakrishna, 2014a). Industrial demand for improved performance and reliability led to the development of manmade fibers in the late nineteenth and early twentieth centuries. Early synthetic filaments were produced using melt, wet, and dry spinning processes, enabling large-scale production of viscose rayon, nylon, polyester, and other polymers (Albrecht et al., 2003). These methods were later refined to produce finer filaments, including microfibers with diameters below 10 μm. Processes such as melt blowing and spunbonding made it possible to manufacture nonwoven webs at high throughput, meeting the needs of filtration, hygiene, and other applications where finer fiber diameters and increased surface area were beneficial.

By the late twentieth century, several methods had been developed to produce fibers with diameters below one micron, giving rise to the field of nanofibers. Techniques such as template synthesis, phase separation, and self-assembly demonstrated the feasibility of fabricating fibers in the tens to hundreds of nanometers range (Z.-M. Huang, Zhang, Kotaki, & Ramakrishna, 2003; D. Li & Xia, 2004). Among these, electrospinning emerged as the most versatile, capable of producing continuous nanofibers from a wide range of polymers. The process was first patented by Formhals in 1934 (Formhals, 1934), but received limited attention until Baumgarten demonstrated the production of ultrafine fibers using an electrostatic field in 1971 (Baumgarten, 1971). Foundational work by Larrondo and Manley in 1981 on melt electrospinning (L. Larrondo & Manley, 1981a, 1981b, 1981c) and by Doshi and Reneker in 1995 on solution electrospinning (Jayesh Doshi & Reneker, 1995) established the technique as a practical route to submicrometer fibers with controllable morphology. In solution electrospinning, the lower viscosity compared to polymer melts allows greater jet stretching,

enabling the production of finer fibers (Z.-M. Huang et al., 2003; Yarin, Pourdeyhimi, & Ramakrishna, 2014b). This ability to achieve submicrometer diameters with a wide range of polymer-solvent systems has made solution electrospinning a central focus for research into advanced nanofiber materials. Compared to their microfiber counterparts, these finer structures offer notable performance gains in existing fiber-based applications, primarily due to their high surface-area-to-volume ratio and the small pore sizes achievable in their assemblies. Such characteristics can enhance filtration efficiency, improve the effectiveness of surface functionalization, and allow more precise control over permeability in membranes and scaffolds.

While laboratory-scale electrospinning has demonstrated the capability to produce nanofibers tailored for specific uses, translating the process to large-scale industrial production remains a challenge. Throughput limitations, process stability, and uniformity of fiber morphology are persistent obstacles. The industrial history of fiber production shows that such challenges can be overcome. Melt blowing and spunbonding are examples of processes that successfully transitioned from laboratory concepts to high-volume manufacturing in response to market demand (Yarin et al., 2014a). However, for solution electrospinning of nanofibers, this transition has not yet been realized at a comparable scale. The present thesis focuses on addressing this gap, with the objective of developing strategies to scale-up electrospinning while maintaining control over fiber properties. To set the stage for these developments, the following section describes the electrospinning process in detail, outlining its operating principles and the key parameters that govern fiber formation.

1.1.2 Electrospinning

Electrospinning is a versatile technique for producing continuous fibers with diameters ranging from the micrometer to the nanometer scale. In this process, a polymer solution is elongated under a high electric field and undergoes solidification through solvent evaporation, forming fibrous mats with controlled morphology. This section describes the typical setup and operating principles of solution electrospinning, followed by an overview of the parameters,

grouped into three categories: solution, process, and ambient conditions, that influence jet behavior and, consequently, fiber quality and morphology.

A conventional electrospinning setup, as shown in Figure 1.1a, consists of a feeding system, typically a syringe pump delivering the polymer solution to a spinneret (often a metallic needle), a high-voltage power supply to establish the electric field, and a collector, often grounded, where the fibers are deposited. At the spinneret tip, the polymer liquid first forms a pendant droplet that elongates under the electrostatic stress generated by the applied field. When the electrostatic stress exceeds the resisting surface tension of the liquid, a charged jet erupts, and the liquid at the base of the jet assumes the conical geometry known as the Taylor cone (Taylor, 1964; Yarin, Koombhongse, & Reneker, 2001b), as illustrated in Figure 1.1b. This jet undergoes stretching in multiple stages: initial narrowing in the Taylor cone, further elongation along a relatively straight segment, also illustrated in Figure 1.1b, and rapid thinning during the subsequent bending and whipping instabilities, as represented in Figure 1.2. During its flight, solvent evaporation progressively solidifies the jet, leading to fiber deposition on the collector (Ramakrishna, Fujihara, Teo, Lim, & Ma, 2005).

Figure 1.1c and Figure 1.1d show electrospun poly(ethylene oxide) (PEO) fibers with markedly different diameters, illustrating the broad range of morphologies achievable with this technique. Such variation results from the combined influence of parameters that can be broadly classified into three categories: solution parameters, processing parameters, and ambient conditions, as presented in Table 1.1 Electrospinning parameters by category. Solution parameters include the polymer-solvent composition and key physicochemical properties such as viscosity, elasticity, and surface tension. Processing parameters encompass the applied voltage, solution flow rate, and spinneret-to-collector distance. Ambient conditions include temperature and humidity, which affect solvent evaporation and jet solidification. Understanding how these factors interact makes it possible to tailor fiber morphology and properties for specific applications. The following three subsections detail the influence of each parameter group on electrospinning outcomes.

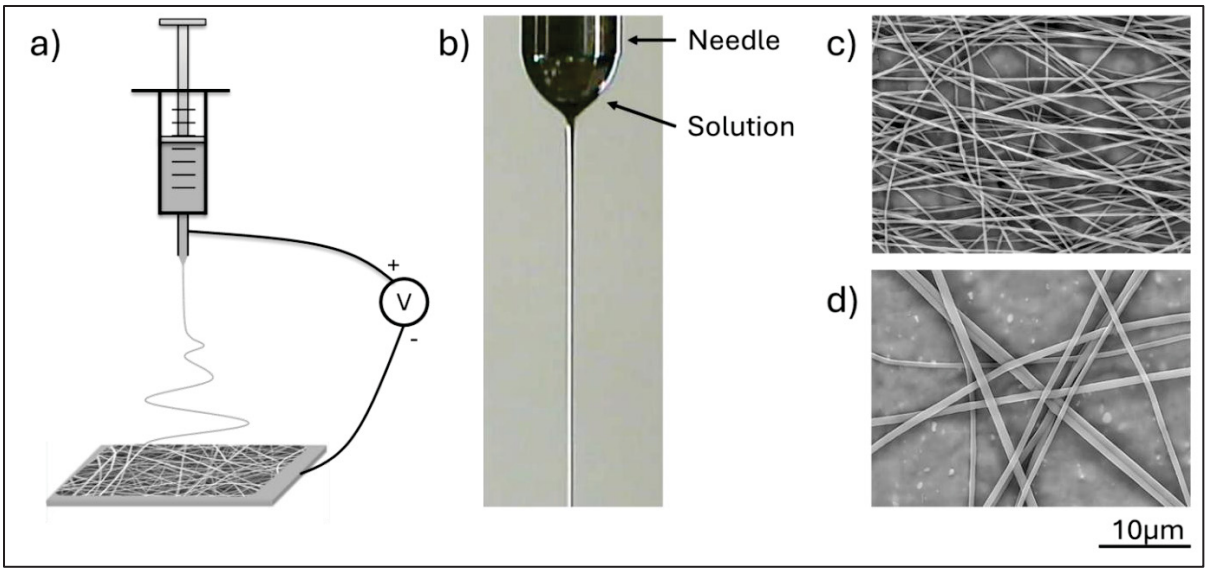

Figure 1.1 a) Schematic of a conventional solution electrospinning setup, comprising a syringe pump, spinneret (needle), high-voltage power supply, and grounded collector; b) Picture of the Taylor cone and initial straight part of the jet formed during electrospinning of a poly(ethylene oxide) (PEO) solution in water; c) Electrospun PEO nanofibers with an average diameter of ~265 nm; d) Electrospun PEO microfibers with an average diameter of ~840 nm; Fiber images illustrate the range of diameters achievable by adjusting solution, processing, and ambient parameters

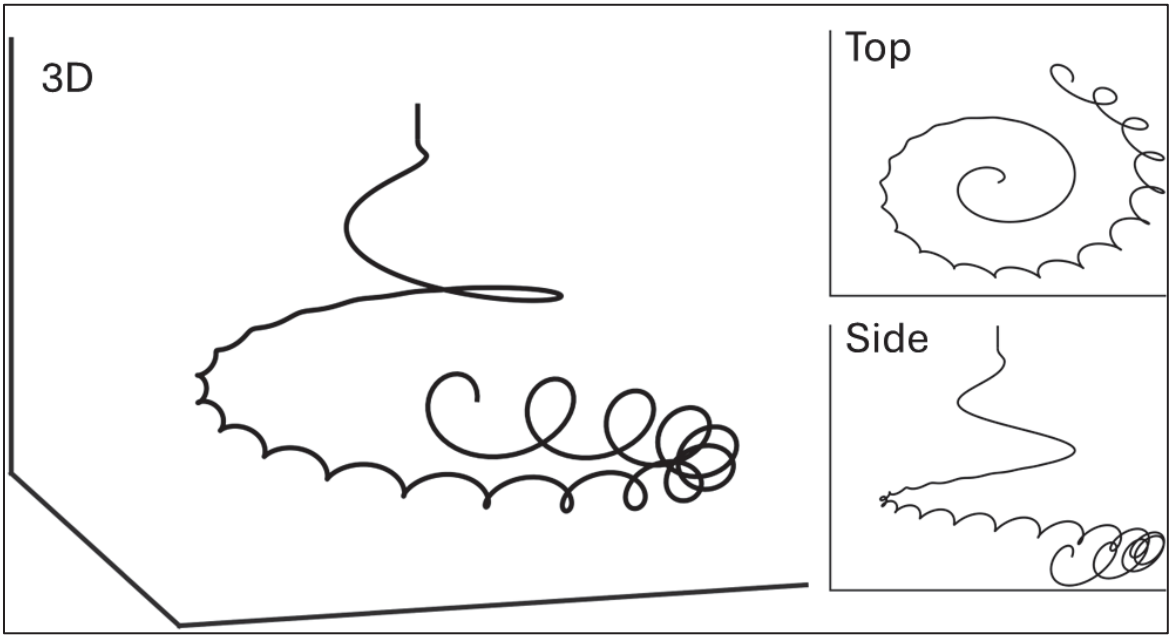

Figure 1.2 Schematic representation of the electrospinning jet path, including the straight segment and the onset of bending instabilities, shown from three perspectives: 3D view, top view, and side view

Table 1.1 Electrospinning parameters by category

Solution Parameters	**Process Parameters**	**Ambient Conditions**
Rheological properties	Applied voltage	Temperature
Surface tension	Solution flow rate	Solvent vapor pressure & Humidity
Electrical properties	Spinneret-to-collector distance	
Solvent volatility		

1.1.2.1 Solution Parameters

The behavior of a polymer solution in electrospinning is set by molecular features of the polymer and its solvent environment, which determine bulk rheology, interfacial properties, electrical response, and evaporation rate. These, in turn, control cone–jet formation, in-flight thinning, and solidification, and thus the final fiber morphology.

1.1.2.1.1 Rheological Behavior of Polymer Solutions

The rheological behavior of polymer solutions originates from the basic molecular characteristics of the polymer. Attributes such as chain stiffness, the presence of bulky side groups, or specific chemical functionalities determine how easily a polymer coil can expand in a solvent and how strongly different chains interact with one another. Flexible chains facilitate intermolecular interactions by occupying a larger volume, while stiffer chains remain more compact and interact only at higher concentrations (Gennes, 1979). The affinity of the polymer with the solvent are equally important: in a “good” solvent, chains swell and interact more readily, whereas in a “poor” solvent they contract (Gennes, 1990). These molecular characteristics do not directly define the rheological properties of the solution, but they establish the molecular conditions under which polymer chains begin to interact and, ultimately, govern the bulk flow behavior of the system (Doi & Edwards, 1986).

In addition to chemical structure, both the size of polymer chains, expressed through their molecular weight, and the amount of chains present in solution, set by concentration, are central determinants of solution rheology. A longer chain forms a larger coil in solution, occupying more hydrodynamic volume than a shorter one (Gennes, 1979). At very low concentrations (dilute regime), these coils are far apart, and viscosity increases only weakly with polymer addition, and the solution behaves almost like a Newtonian fluid (Doi & Edwards, 1986). As concentration increases to the overlap concentration (c^*), coils begin to interpenetrate and viscosity grows more strongly, entering a power-law dependence on concentration (Rubinstein & Colby, 2003). Upon further increase past the entanglement concentration (c_e), overlapping chains form topological constraints that restrict motion, and viscosity and relaxation times increase steeply with concentration, often scaling as power laws (Rubinstein & Colby, 2003). Both c^* and c_e are not fixed values but depend sensitively on molecular weight and chain structure: larger, more flexible coils overlap and entangle at lower concentrations than shorter or stiffer chains (Graessley, 1980). Entanglements mark a qualitative transition: they endow the solution with elasticity, giving rise to non-Newtonian behaviors such as shear-thinning in steady shear and strain hardening in extensional flows (H.A. Barnes, 1993; John M. Dealy, 1990; McCrum, Buckley, & Bucknall, 1988).

Polymer samples never consist of chains of identical length; instead, they contain a distribution of molecular weights. To characterize this distribution, several averages are commonly defined. The number-average molecular weight (Mn) reflects the simple average chain size, giving equal weight to each molecule, while the weight-average molecular weight (Mw) gives greater weight to longer chains since they contribute proportionally more mass. Because longer chains occupy more hydrodynamic volume and entangle more effectively, Mw is more representative of the properties that control viscoelasticity. The ratio Mw/Mn, known as the polydispersity index (PDI), provides a measure of the breadth of the distribution (Dealy, Read, & Larson, 2018).

The presence of both short and long chains strongly influences solution rheology. Short chains relax quickly and mainly contribute to the viscous response, whereas long chains dominate the

slowest relaxation modes and are primarily responsible for the elastic character of the solution. Consequently, broad molecular weight distributions enhance elasticity compared to narrow distributions, since even a small fraction of long chains is sufficient to form entanglements and extend relaxation times. In practice, this means that the viscoelastic properties of a polymer solution are not governed by a single molecular weight, but by the combined effects of the entire distribution, with disproportionate influence from the longest chains (Mieras & Van Rijn, 1969; Struglinski & Graessley, 1985; Vinogradov et al., 1980; Wasserman & Graessley, 1992).

At the level of the electrospinning jet, the rheological properties of polymer solutions directly determine jet stability and fiber morphology. Among the various descriptors, the relaxation time in extension, which can be quantified using a capillary breakup extensional rheometer (CaBER), has proven to be a particularly reliable predictor of electrospinnability (Ewaldz, Randrup, & Brettmann, 2022; Gupta, Jassal, & Agrawal, 2015; Yu, Fridrikh, & Rutledge, 2006). A detailed description of CaBER, and how it enables measurement of relaxation times in extension for low-viscosity polymer solutions, is presented in a later section of this chapter. The relaxation time represents the characteristic timescale over which stretched polymer chains recover toward equilibrium. In practice, this parameter reflects how long the jet can maintain a coherent cylindrical geometry during stretching: a longer relaxation time allows elastic stresses to counteract necking and preserve jet continuity until solidification occurs. Solutions with sub-entanglement concentrations, and thus low extensional elasticity, lack this resistance and tend to break up prematurely due to the lack of intermolecular cohesion. By contrast, once concentrations exceed the entanglement threshold, the buildup of elastic stresses can stabilize the filament and permit continuous fiber drawing. This stabilization is further reinforced by strain hardening, the nonlinear increase in extensional viscosity with strain, which provides an additional mechanism to delay filament rupture under rapid stretching. In practice, a minimum level of elasticity is required to produce uniform fibers, but excessive elasticity, associated with very long relaxation times, reduces jet ability to stretch and yields larger-diameter fibers.

1.1.2.1.2 Surface Tension

Surface tension arises from the imbalance of molecular interactions at the liquid–air interface. Molecules within the bulk of a liquid experience cohesive forces equally in all directions, whereas molecules at the surface are subjected to asymmetric forces, with fewer neighboring molecules at the interface. This imbalance creates an energetic cost associated with increasing the liquid surface area, quantified as the surface free energy per unit area. Equivalently, surface tension manifests as a force per unit length acting along the contact line, directed toward the bulk liquid. In practical terms, surface tension drives liquids to minimize their surface, favoring spherical droplets over extended geometries (Gennes, Brochard-Wyart, & Quéré, 2004).

In electrospinning, surface tension resists the deformation of the pendant droplet at the spinneret tip, opposing the withdrawal of liquid by the applied electric field. When the electrical stress exceeds the capillary pressure, a charged jet erupts, and the fluid at the spinneret assumes the conical geometry known as the Taylor cone. This shape reflects the balance between surface tension, the electrostatic forces, and the rheological properties of the solution. Even after the jet has been initiated, surface tension continues to throttle the emission, effectively acting as a valve that regulates the flow rate for a given field strength. The extent of this throttling also depends on the electrical properties of the solution, particularly its conductivity, which influences the magnitude of the electrostatic stress (Taylor, 1964; Yarin et al., 2001b).

Once the jet is airborne, surface tension acts as the primary destabilizing force. A long liquid filament is intrinsically unstable to the Rayleigh–Plateau mechanism, in which small surface perturbations grow and eventually lead to breakup (Plateau, 1873; Rayleigh, 1878). This process, familiar from the disintegration of a water stream into droplets, similarly affects electrospinning jets. In this context, the instability manifests as the formation of beads along fibers, or, in severe cases, as complete jet breakup that prevents continuous fiber formation (Fong, Chun, & Reneker, 1999; Gennes et al., 2004; Plateau, 1873; Rayleigh, 1878). Producing smooth cylindrical fibers therefore requires adjusting multiple parameters, including solution,

process, and ambient conditions, in relation to one another. As will be illustrated in the case study on bead formation presented later in this document, this balance enables stable jet formation and uniform fibers to be obtained despite surface tension sometimes being high (~40 mN/m or higher in aqueous solutions).

1.1.2.1.3 Electrical Properties

Electrospinning relies on the conversion of electrical energy into mechanical stretching of a liquid filament. This conversion is mediated by the electrical charges sustained within the solution, which enable the jet to be pulled and stretched under an applied field. The ability of a solution to sustain and redistribute charges is therefore central to electrospinning, and is primarily determined by two properties: its conductivity, which governs charge transport, and its dielectric permittivity, which governs charge storage. Together, these parameters determine the charge density that can be established in the jet, and thus the magnitude of the electrical stress available to deform and thin it (Reneker, Yarin, Fong, & Koombhongse, 2000; Yarin, Koombhongse, & Reneker, 2001a).

The first stage where electrical properties play a decisive role is jet initiation. Under an applied electric field, charges are driven through the solution toward the surface, where they accumulate at the liquid–air interface. Here, “charges” correspond to an imbalance of mobile ions: the electric field drives positive ions toward the negative electrode and negative ions toward the positive electrode, so that regions of the fluid acquire a net excess of charge of either polarity. The interaction of the field with these charges produces an electrostatic stress, which must overcome surface tension for a jet to emerge from the Taylor cone (Taylor, 1964; Yarin et al., 2001b). In more conductive solutions, charge transport is more efficient, allowing higher surface charge densities to be established. As a result, jets can be initiated at lower applied voltages, while poorly conducting solutions often require stronger fields to achieve the same condition (Ahmadi Bonakdar & Rodrigue, 2024; Al-Abduljabbar & Farooq, 2022; Ramakrishna et al., 2005; Yarin et al., 2001b).

Once the jet is emitted, electrical properties continue to govern its stretching in the straight segment that connects the cone to the onset of instabilities. The charges carried by the jet are transported with the rapidly accelerating fluid, since the speed at which ions migrate under the electric field is negligible compared to the jet velocity; they therefore remain effectively bound to the liquid filament rather than moving independently through it (Reneker & Yarin, 2008; Reneker et al., 2000). The tensile force exerted by the electric field therefore depends on both the amount of excess charge the jet carries and how strongly that charge couples to the field. Solution conductivity influences the amount of charge, since more conductive solutions allow ions to respond more readily in the meniscus region and supply a higher density of excess charge into the jet. Dielectric permittivity influences the coupling strength, since it determines how effectively the applied field translates into electrostatic stress on those charges (Guarino, Cirillo, Taddei, Alvarez-Perez, & Ambrosio, 2011). As a result, solutions with higher conductivity and higher permittivity undergo greater elongation under the same applied voltage, typically yielding thinner jets and smaller fibers (Guarino et al., 2011; Ramakrishna et al., 2005).

Beyond the straight segment, the jet enters the regime of bending or whipping instability, as illustrated in Figure 1.2, where Coulombic repulsion between surface charges amplifies small perturbations into large lateral motions (Reneker & Yarin, 2008; Reneker et al., 2000). A higher charge density intensifies this whipping, which increases jet stretching and reduces fiber diameter. At the same time, stronger instabilities broaden the deposition area and can introduce non-uniform fiber diameter distribution (Al-Abduljabbar & Farooq, 2022).

Thus, electrical properties influence fiber formation not only during jet initiation and elongation, but also through the development of instabilities. Greater conductivity increases the amount of charge injected into the jet, while higher dielectric permittivity governs how strongly the electric field acts on that charge. Together, they modulate the electrostatic stress that stretches the jet and shapes the resulting fibers.

1.1.2.1.4 Solvent Volatility

The volatility of the solvent dictates how rapidly the polymer solution loses liquid during electrospinning, thereby controlling the timescale for jet solidification. Volatility is affected by the solvent's vapor pressure, which reflects the number of solvent molecules already present in the air surrounding the liquid. More details about the influence of ambient conditions are presented in Section 1.1.2.3 (Ambient Parameters).

In a polymer solution, however, evaporation is not determined by the solvent volatility alone. For solvent molecules to escape into the air, they must first reach the surface from the interior of the liquid. This occurs by diffusion, driven by concentration gradients within the solution. As the solution becomes enriched in polymer, evaporation slows down: not only are fewer solvent molecules available near the surface, but their mobility is increasingly hindered by polymer–solvent interactions and the rising viscosity of the medium, making it more difficult for them to reach the interface (Crank, 1975; Ohring, 2002; Okuzono, Ozawa, & Doi, 2006).

In electrospinning, the jet adopts an elongated cylindrical geometry with diameters in the micron or submicron range. Such slender dimensions give the jet a very high surface-to-volume ratio, which markedly shortens the timescale for drying and solidification. Continuous thinning of the jet during stretching further increases surface exposure and accelerates solvent loss. For stable fiber formation, solvent evaporation must occur at an appropriate rate relative to the jet dynamics. If solvent removal is too rapid, solidification may begin at the surface of the Taylor cone, causing needle clogging or unstable jet initiation. If solidification occurs too early in flight, the jet cannot stretch sufficiently to reach nanoscale diameters. Conversely, if evaporation is too slow, the jet may break before solidification or reach the collector in a liquid state, leading to coalesced fibers or a film (Cai & Gevelber, 2013; Deshawar, Gupta, & Chokshi, 2020; Tripatanasuwan, Zhong, & Reneker, 2007). In essence, fiber formation requires that the evaporation timescale be matched to the jet flight time: long enough to permit nanoscale stretching, but short enough to achieve solidification before deposition.

1.1.2.2 Process Parameters

In addition to solution properties, the operating conditions of the electrospinning setup strongly influence jet stability and fiber morphology. The most critical process parameters are the applied voltage, the solution flow rate, and the distance between the needle and the collector. These parameters are presented individually here, while their codependence with solution and environmental conditions in determining stable electrospinning and controlled fiber deposition will be detailed in the bead formation case study presented later in this chapter.

1.1.2.2.1 Applied Voltage

The applied voltage establishes the electric field that imposes an electrostatic stress on the droplet at the needle tip. When this stress exceeds the resisting surface tension, the liquid deforms into a Taylor cone and a jet is initiated, as illustrated in Figure 1.3. The threshold voltage therefore defines the minimum condition for jet formation. Stable electrospinning can be maintained only within a finite voltage window above this threshold. The influence of voltage on Taylor cone formation is illustrated in Figure 1.4: under optimal conditions, a stable cone–jet configuration is obtained (Figure 1.4a), whereas excessively high voltages destabilize the system, causing the cone to drain faster than it can be replenished (Figure 1.4b) or leading to the emission of multiple jets (Figure 1.4c), which can ultimately clog the needle. Overall, increasing the voltage increases the stress applied to the jet, which promotes greater stretching and the production of smaller fiber diameters, provided stability is maintained (Basu, Agrawal, & Jassal, 2011; J.M. Deitzel, 2000; Jayesh Doshi & Reneker, 1995; Reneker & Yarin, 2008; Reneker et al., 2000; Taylor, 1964; Thompson, Chase, Yarin, & Reneker, 2007; Yarin et al., 2001a, 2001b).

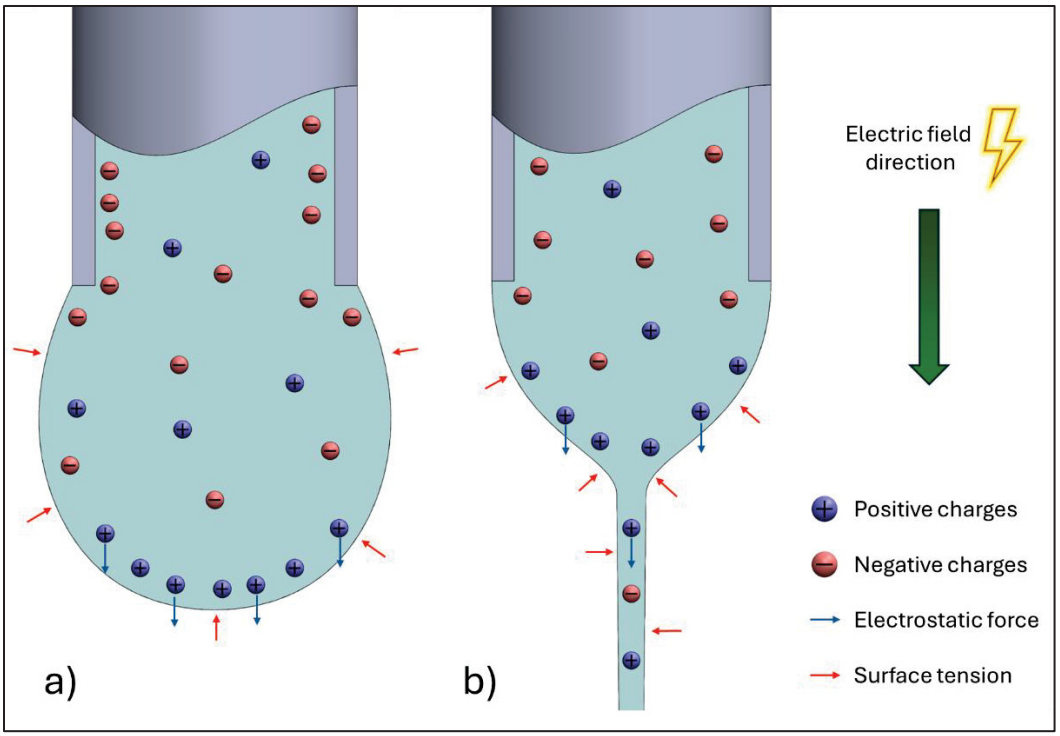

Figure 1.3 Schematic representation of jet initiation during electrospinning; a) pendant drop below the minimum threshold voltage for jet initiation, where electrostatic forces are insufficient to overcome surface tension; b) taylor cone–jet configuration, above threshold, where electrostatic forces overcome surface tension and a stable jet emerges

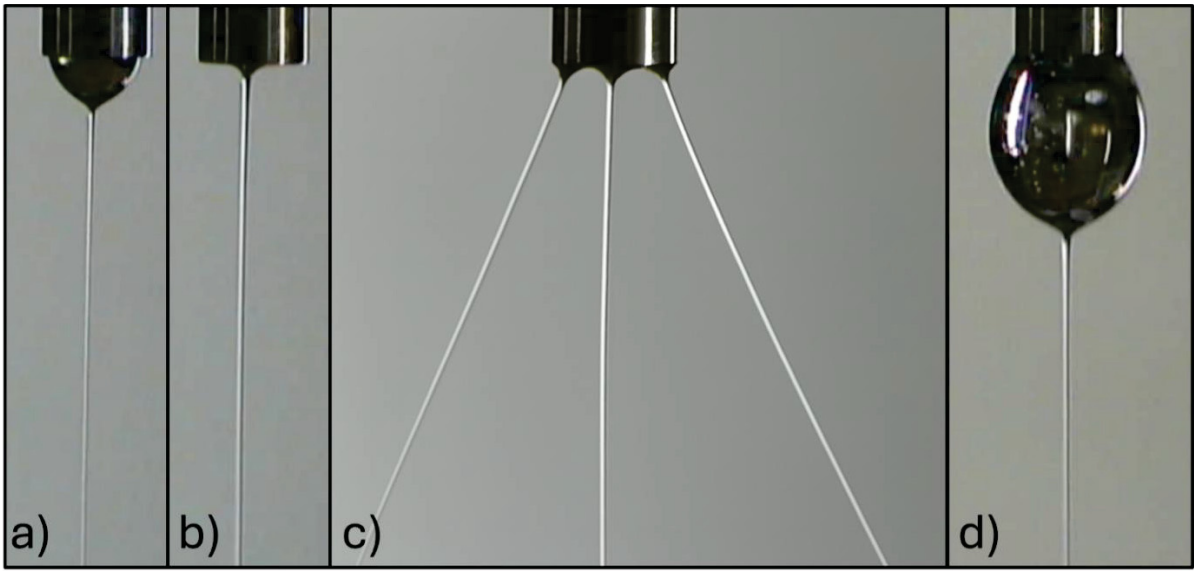

Figure 1.4 Influence of applied voltage and flow rate on Taylor cone formation; a) stable cone-jet configuration under optimal conditions; b) drained cone under excessively high voltage; c) multiple jets emerging from the needle tip under excessively high voltage; d) large pendant drop at the needle tip under excessive flow rate

1.1.2.2.2 Flow Rate

The flow rate is externally set by the pump and must match the rate at which the electric field can draw solution out of the Taylor cone. A minimum flow rate is required to maintain a stable cone and avoid drainage; if the flow is insufficient, the cone may choke, leading to unstable jetting and clogging at the needle tip. At the other extreme, an excessive flow rate lowers the charge density within the jet, reducing the stretching forces and yielding larger fibers or bead formation. The resulting thicker jet also requires more time for solvent removal, so it may not fully dry before reaching the collector, leading to wet or fused deposits. If the applied flow significantly exceeds the capacity of the electric field to draw it into a jet, dripping of solution from the needle may occur, as illustrated in Figure 1.4d (Ahmadi Bonakdar & Rodrigue, 2024; Al-Abduljabbar & Farooq, 2022; Basu et al., 2011; J.M. Deitzel, 2000; Reneker & Yarin, 2008).

1.1.2.2.3 Needle-Collector Distance

The distance between the needle and the collector determines the jet flight time, and therefore the time available for stretching and solvent evaporation. It must be long enough to allow solidification before the jet reaches the collector. At the same time, this distance, in combination with the applied voltage, influences the characteristics of the electric field that governs jet elongation and deposition. Because the field is strongest near the needle tip and decays with distance, changing both the gap and the voltage alters not only the average field strength but also its spatial distribution. If the distance is too short, drying is incomplete and fibers may fuse on the collector; if it is too long, the deposition area broadens and a higher voltage is required to maintain a similar electric field strength near the needle (Basu et al., 2011; Basu, Jassal, & Agrawal, 2013; Joy, Anuraj, Viravalli, Dixit, & Samavedi, 2021). The geometry of the collector further shapes the field lines and can be used to guide deposition patterns such as aligned fibers (Alfaro De Prá, Ribeiro-do-Valle, Maraschin, & Veleirinho, 2017; J.M. Deitzel, 2000; Kuru, 2025; Robinson et al., 2021; Zhou, Hu, Du, & Tan, 2018).

1.1.2.3 Ambient Parameters

During electrospinning, the jet exchanges heat and mass with the surrounding atmosphere. Ambient conditions such as temperature and the vapor composition of the air influence both solvent volatility and the rheological response of the jet. These factors govern the balance between stretching and solidification, and therefore strongly influence fiber formation.

1.1.2.3.1 Temperature

Temperature directly affects both the rheology of the solution and the rate of solvent removal. Increasing temperature lowers solution viscosity and reduces elastic resistance, allowing the jet to stretch more rapidly. At the same time, higher temperature also raises the solvent's saturation vapor pressure, further accelerating evaporation, and can slightly reduce surface tension while increasing ionic mobility.

While reduced viscosity promotes finer fibers by enabling greater elongation, accelerated evaporation induces earlier solidification, restricting further stretching and favoring larger fiber diameters. Lower surface tension improves jet stability, while faster ion motion leads to a higher charge density, intensifying electrostatic stretching. These counteracting influences act on different spatial and temporal scales during jet evolution. In the initial region near the needle, where the electric field is strongest and the jet is still relatively large, reduced rheological resistance predominates, allowing rapid elongation compared to a colder jet. As the filament thins and moves downstream, electrostatic stretching diminishes while solvent evaporation becomes increasingly dominant due to the higher surface-to-volume ratio, leading to pronounced solidification. At elevated temperature, this sequence typically allows the jet to undergo greater elongation before solvent loss becomes the limiting factor, ultimately leading to solidification at smaller diameters.

Overall, moderate heating often produces finer fibers by enhancing stretchability, but excessive heating can lead to premature solidification at the needle tip, causing clogging or unstable jetting (Ahmadi Bonakdar & Rodrigue, 2024; De Vrieze et al., 2009).

1.1.2.3.2 Solvent Vapor Pressure & Humidity

The composition of the surrounding air strongly regulates the solidification dynamics of the electrospinning jet. Solvent evaporation is governed by the difference between its saturation vapor pressure and its partial pressure in the atmosphere. When solvent molecules are already present, whether from intentional vapor addition or accumulation in poorly ventilated environments, the driving force for evaporation decreases. As a result, solidification is delayed, the jet remains liquid for a longer time, and fibers are produced with smaller diameters but a higher likelihood of bead formation (Ahmadi Bonakdar & Rodrigue, 2024; Al-Abduljabbar & Farooq, 2022; De Vrieze et al., 2009; Ramakrishna et al., 2005; Thompson et al., 2007; Yarin et al., 2014a). If drying is incomplete, fused fibers or even films may be formed. Conversely, overly rapid evaporation favors larger fibers and can promote clogging at the needle tip.

When water serves as the solvent, the surrounding relative humidity directly sets this vapor pressure gradient and therefore controls the evaporation rate. In systems where the solvent is not water, humidity can still affect jet solidification. Hydrophilic solutions can absorb moisture from the atmosphere, leading to surface gelation, a premature solidification that stiffens the jet, often yielding thicker fibers, but may cause incomplete drying upon deposition. In contrast, hydrophobic solvents are largely insensitive to atmospheric moisture, and jetting proceeds unaffected. Beyond these mass-transfer effects, water vapor also modifies the dielectric properties of air. As a result, the electric field distribution is altered, changing the magnitude and profile of the electrostatic stresses acting on the jet.

1.1.2.4 Case Study: Bead formation in Electrospinning

Bead formation is one of the most characteristic defects in electrospinning and provides a clear example of how solution, process, and ambient parameters must act together to stabilize the jet (Fong et al., 1999; Zuo et al., 2005). Figure 1.5 shows a typical morphological sequence illustrating how capillary breakup evolves and can be progressively suppressed: a) isolated droplets from complete jet disintegration, b) particles connected by thin filaments, c) continuous fibers decorated with beads, often described as “beads-on-string”, and d) smooth, uniform fibers when capillary breakup is fully suppressed. Beaded fibers thus represent an intermediate state, produced when the jet partially resists instability and solidifies before full breakup can occur.

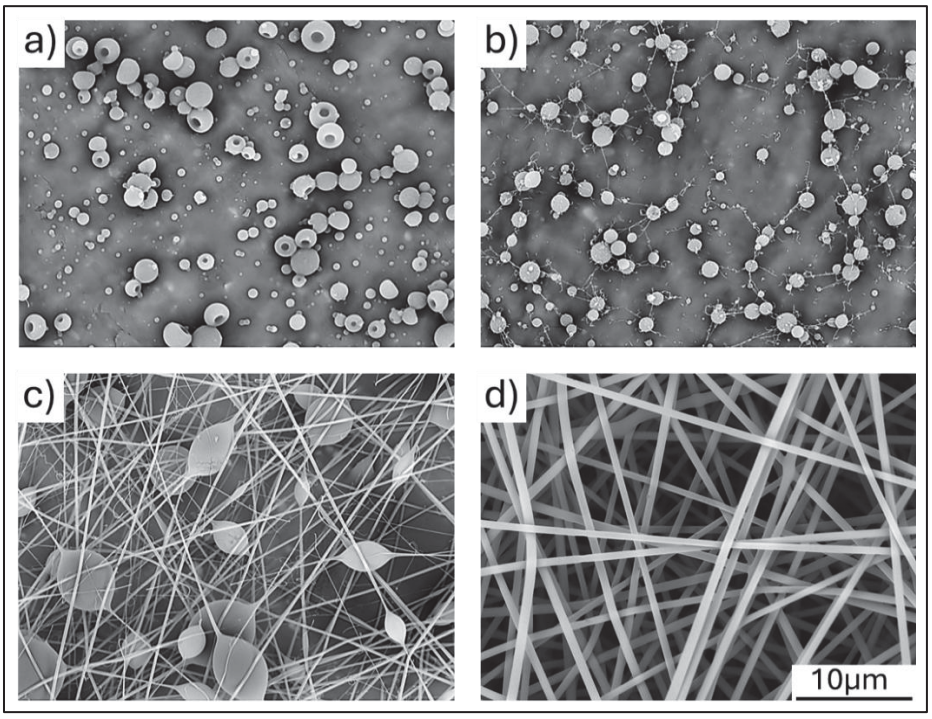

Figure 1.5 Morphological sequence in electrospinning, illustrating suppression of capillary breakup, a) isolated droplets, b) particles connected by thin filaments, c) bead-on-string structure, and d) smooth, continuous fibers; the sequence shown here was obtained from aqueous pullulan solutions

Slender liquid cylinders are intrinsically prone to capillary breakup via the Plateau–Rayleigh instability (Eggers, 1997; Plateau, 1873; Rayleigh, 1878). Small axial variations in radius create capillary-pressure gradients: molecules at the interface experience an inward imbalance of cohesive forces, and regions of tighter curvature present more surface area per unit volume, which results in higher local pressure that drives liquid out of the neck and into adjacent thicker sections. If unopposed, these perturbations grow and the jet disintegrates into droplets. In electrospinning, continuous fibers are obtained only when stabilizing mechanisms and timing are provided: the jet must be stretched rapidly to the target diameter and solidified by solvent removal before these capillary disturbances can amplify.

In electrospinning, the way to suppress the natural tendency toward breakup is to maintain the jet in a state where stabilizing stresses outweigh capillary forces. This is achieved primarily through the strain-hardening response in extension, which is exhibited by many polymer solutions. Strain hardening refers to the increase in resistance to deformation as a material is deformed: much like a spring that stiffens the more it is pulled (Doi & Edwards, 1986; Rubinstein & Colby, 2003). When a local neck forms in the jet, that region has already undergone more deformation than its surroundings, so its effective extensional viscosity is higher. As a result, the neck becomes stiffer and deforms more slowly than the adjacent thicker sections, reversing the Plateau-Rayleigh instability in which thinner regions normally deform more rapidly. In this way, strain-hardening polymer solutions can sustain nearly cylindrical filaments in which small perturbations are unable to grow (Anna & McKinley, 2001; Clasen, Eggers, Fontelos, Li, & McKinley, 2006; Entov, 1986; Entov & Hinch, 1997; Entov & Shmaryan, 1997; Entov & Yarin, 1984; Yarin et al., 2001a).

Because of this stiffening, surface tension is no longer strong enough to amplify local thinning, and further deformation of the neck is effectively suppressed. However, this stabilizing elastic stress is not permanent. Polymer liquids exhibit viscoelastic behavior: over time, the molecular chains relax toward equilibrium, and the stored elastic stress dissipates. If the jet is not continuously stretched, surface-tension–driven perturbations can reemerge. For this reason, electrospinning requires the deformation to be maintained at a rate high enough, relative to the

polymer relaxation timescale, to keep the jet in its strained, stiffened state. When this balance is achieved, strain hardening prevents capillary breakup and enables the formation of continuous, uniform fibers.

Stable electrospinning requires that solution, process, and ambient parameters act together to maintain the jet in a strained, stiffened state until solidification occurs. Solution properties define the basic capacity of the jet to resist capillary breakup by providing elasticity through entangled chains. Molecular structure, molecular weight, and concentration all influence the degree of entanglement, which governs whether the solution exhibits sufficient elastic response and strain hardening under extension. The relaxation time reflects how long this elastic resistance can be maintained: the longer the relaxation time, the longer the jet can remain under stress without relaxing, and the less likely it is that beads will form. In practice, relaxation time therefore serves as a useful indicator of electrospinnability, especially for low-viscosity solutions where strain hardening is difficult to measure directly (Gupta et al., 2015; Yu et al., 2006).

Beyond rheology, solution formulation also sets the electrical properties, conductivity and permittivity, which determine the charge density carried by the jet and thus the magnitude of electrostatic stress available for stretching (Reneker et al., 2000; Theron, Zussman, & Yarin, 2004; Thompson et al., 2007; Yarin et al., 2001a). A higher charge density enhances elongation and helps keep the jet in its strained state. At the same time, surface tension acts in the opposite direction by promoting Rayleigh breakup, so lowering surface tension slows the amplification of perturbations and facilitates stable fiber formation.

Process parameters govern how the available elasticity is engaged. The applied voltage provides the electrostatic stress that extracts liquid from the Taylor cone and drives the jet's continuous elongation. This stress must be high enough to maintain deformation faster than relaxation, but because the field also draws liquid from the cone, excessive voltage mainly increases throughput rather than elongation rate, which destabilizes the process unless the pump flow rate is properly adjusted (Basu et al., 2011; Jayesh Doshi & Reneker, 1995). When

the flow rate is too high, the jet carries a larger volume with lower charge density, reducing stretching per unit volume and leaving insufficient time for solvent evaporation, all of which promote bead formation (Ahmadi Bonakdar & Rodrigue, 2024; Al-Abduljabbar & Farooq, 2022; Tang, Si, Xu, & Liu, 2014). The needle–collector distance, in turn, is coupled with voltage to define the electric field strength and distribution. Short distances provide strong initial stress, but the field decays quickly and may not sustain stretching long enough to stabilize the jet.

Ambient conditions determine whether the jet solidifies in time to preserve its cylindrical form. Solvent evaporation increases polymer concentration and strain hardening, thereby stabilizing the jet, but the rate of evaporation sets how quickly this stabilization occurs and locks in the cylindrical geometry. Faster drying shortens the window during which surface-tension instabilities can grow, which is especially important because electrostatic stresses are strongest near the needle and gradually weaken along the flight path, while instabilities grow faster at smaller jet radius. Conversely, slow drying leaves the filament liquid for longer, giving perturbations time to amplify and produce beads. In addition, ambient temperature, humidity, and solvent vapor content alter the dielectric properties of the surrounding air, which modifies the electric field distribution and thus the stresses available for jet stabilization. More humid air increases the permittivity of the atmosphere, which weakens the electric field for a given applied voltage and further reduces drying, conditions that both favor bead formation (when water is used as a solvent). Higher temperatures, in contrast, slightly strengthen the field while also accelerating evaporation, generally promoting finer fibers though at the risk of premature solidification near the needle (De Vrieze et al., 2009).

Taken together, these effects show that no single parameter controls bead suppression in isolation. Solution rheology must provide sufficient strain hardening and a long relaxation time, process parameters must be adjusted so that the jet is continuously stretched at a rate exceeding its relaxation; and evaporation must occur on the right timescale to lock in the cylindrical morphology before instabilities can grow. When these conditions act in concert, electrospinning produces uniform, continuous fibers, whereas imbalance in any one factor

leads instead to beads-on-string structures, or in more severe cases, complete disintegration of the jet into particles.

From this analysis, a few design rules for suppressing beads emerge:

- Minimize surface tension to slow the amplification of capillary instabilities (for example, through the use of surfactants).
- Ensure sufficient viscoelastic resistance (via higher-molecular-weight polymers, higher concentration, or employing blends of different molecular weights as discussed in Chapter 6) so that strain hardening can suppress local thinning.
- Maintain adequate electrostatic stress to keep the jet continuously stretched (for example, by keeping flow rates low or increasing jet charge density with conductive additives).
- Match evaporation and stretching timescales (by adjusting solvent vapor content or temperature) to ensure the jet solidifies before instabilities can evolve.

Thus, bead suppression is not the result of tuning a single parameter but of orchestrating multiple, interdependent factors. The transition shown in Figure 1.5, from droplets to smooth fibers, is a direct manifestation of how the Plateau–Rayleigh instability is progressively neutralized by strain hardening, sustained stretching, and timely solidification. In order to understand and optimize the electrospinning process, it is essential to quantify the extensional rheology of polymer solutions, a need that motivates the use of the Capillary Breakup Extensional Rheometer (CaBER), a tool designed to probe material behavior under elongational flow.

1.1.3 CaBER

Rheology describes how materials deform and flow under applied stresses. Most conventional rheometric techniques are designed to probe shear flows, which are easier to impose and control. However, many real flows are not purely shear but involve significant elongational deformation. Fiber spinning, film blowing, spraying, coating, inkjet printing, and droplet breakup all involve fluids undergoing strong extensional stresses. Other processes, such as lubrication in engines or polymer melt processing through contractions and dies, are a mix of

shear and extension, where the elongational component plays a central role in determining resistance to flow, stability, and final product morphology. In all these cases, shear characterization alone does not capture the full rheological response that governs processing and performance. This need to probe material behavior under extension provided the motivation for the development of dedicated elongational rheometers (Cogswell, 1968, 1981; H.A. Barnes, 1993; Q. Huang, 2022; McCrum et al., 1988; Joachim Meissner, 1972; J. Meissner, 1984; Sentmanat, 2004).

Measuring elongational properties, however, presents unique challenges. Traditional stretching rheometers were designed primarily for polymer melts and other highly viscous systems. In these cases, the sample must be stiff enough to resist rapid capillary collapse, allowing the imposed strain to be followed and the tensile force to be measured with sufficient accuracy. By contrast, dilute polymer solutions or other low-viscosity liquids disintegrate too quickly, and the associated forces are too small, making conventional stretching methods impractical (Galindo-Rosales, Alves, & Oliveira, 2012). A major step forward came with the work of Bazilevsky, Entov, and Rozhkov in 1990 (Bazilevsky, Entov, & Rozhkov, 1990), who demonstrated that the dynamics of capillary-driven filament thinning could be exploited as a quantitative probe of fluid rheology, opening the way for filament-thinning methods as practical extensional rheometers. Building on this idea, the approach was later pioneered by McKinley and co-workers into the capillary breakup extensional rheometer (CaBER), which provided a simple and reproducible means of characterizing extensional properties of low-viscosity samples (Anna & McKinley, 2001; McKinley, 2005; McKinley & Tripathi, 2000).

The objective of the CaBER technique is to place a liquid into a geometry where it will inevitably collapse under its own capillary pressure, and to monitor the breakup dynamics from which rheological properties can be extracted. In practice, a small droplet is loaded between two parallel plates, which are then rapidly separated in a step stretch, establishing a slender liquid bridge, as illustrated in Figure 1.6. After the plates stop moving, the filament thins and eventually breaks solely under capillary forces. Throughout this process, the mid-plane diameter of the bridge, $D(t)$, is recorded using a high-speed camera or an optical sensor. The

resulting diameter–time curve reflects the competition between surface tension, which drives thinning, and the rheological properties of the liquid, which resist it.

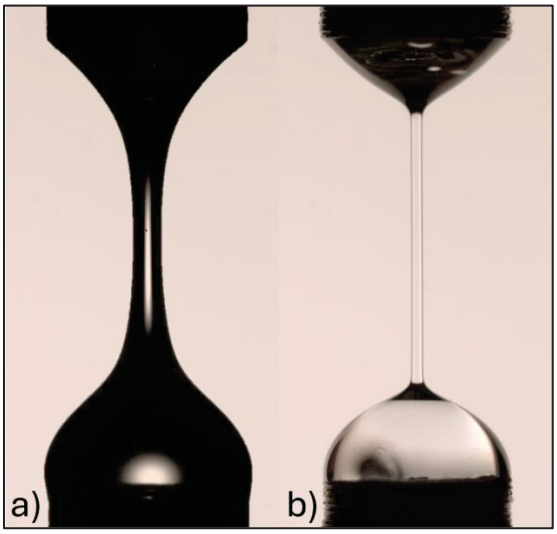

Figure 1.6 Liquid bridges formed in a capillary breakup extensional rheometer (CaBER); a) Newtonian polyethylene glycol (PEG) solution exhibiting the characteristic hourglass profile; b) viscoelastic polyethylene oxide (PEO) solution retaining a nearly cylindrical filament geometry in the elasto-capillary regime; both images were obtained using the custom CaBER developed in this work, which is described in detail in Chapter 4

For a Newtonian liquid, filament thinning is governed by the balance between surface tension, which drives collapse, and purely viscous stress, which resists it. As rupture is approached, the liquid bridge narrows into a characteristic hourglass profile with a well-defined neck at the mid-plane, as presented in Figure 1.6a. The filament shape converges toward a self-similar solution identified by Papageorgiou (McKinley & Tripathi, 2000; Papageorgiou, 1995). Under these conditions, the mid-plane radius decreases linearly with time according to:

$$R_{mid}(t) = 0.0709\frac{\sigma}{\eta_s}(t_c - t) \tag{1.1}$$

where $R_{mid}(t)$ is the filament radius at the pinching point as function of time, σ is the surface tension, η_s is the equivalent shear viscosity and t_c is the critical time to breakup, where $R_{mid}(t_c) = 0$.

It should be noted that the linear Papageorgiou law describes the asymptotic regime typically close to breakup, and that the time required to reach this regime depends on the initial filament geometry and on dimensionless parameters such as the aspect ratio and Bond number (Eggers, 1997; McKinley, 2005; McKinley & Tripathi, 2000; Papageorgiou, 1995). In practice, only sufficiently thin and long filaments converge cleanly to the self-similar form, making the observed dynamics sensitive to experimental conditions. Furthermore, close to breakup, when the filament radius becomes small, additional effects such as inertia may influence the thinning behavior. These considerations set practical limits on the range of conditions over which Newtonian viscosities can be reliably extracted from CaBER experiments.

After an initial phase where viscous and capillary forces govern the dynamics (visco-capillary regime), elastic stresses progressively build up as the filament is stretched. When these stored elastic stresses exceed the viscous resistance, the system enters an elasto-capillary regime that profoundly slows the thinning process (Anna & McKinley, 2001; Bazilevsky, Entov, Lerner, & Rozhkov, 1996; Entov & Hinch, 1997; Entov & Yarin, 1984; McKinley, 2005). During this regime, the filament adopts a nearly cylindrical geometry, as illustrated in Figure 1.6b, that recalls the form observed in electrospinning jets. Instead of a linear decay, the filament diameter decreases exponentially over time, with a rate determined by the characteristic relaxation time λ of the fluid:

$$\mathrm{D}(t) = \alpha \cdot \exp\left(-\frac{t}{3\lambda}\right) \tag{1.2}$$

where $\mathrm{D}(t)$ is the filament diameter at time t. The parameter α is a fitting constant that represents the hypothetical filament diameter $D(0)$, obtained by extrapolating the exponential thinning relation to $t = 0$. This relation is derived for a single-mode Maxwell (or equivalently Oldroyd-B) fluid and is exact only when the material can be described by a single dominant relaxation time. In practice, for fluids exhibiting multiple relaxation modes, the elasto-capillary regime emerges at timescales on the order of or greater than the apparent relaxation time of the fluid (Entov & Hinch, 1997). Measuring the relaxation time λ through CaBER thus provides a quantitative indicator of the fluid's extensional elasticity. While λ is not a direct measure of

elasticity, it reflects the characteristic timescale of the elastic response during filament thinning and is therefore commonly used as a practical indicator of viscoelastic effects in CaBER measurements of polymer solutions. The relaxation time determined from CaBER is specific to extensional flow and does not correspond to the relaxation time inferred from shear stress-relaxation measurements.

It should be emphasized that the exponential form is only observed once elastic stresses dominate over viscous resistance. In practice, this requires that the filament undergo large deformations to store sufficient elastic stress to overcome viscous dissipation (Entov & Hinch, 1997). Observation times must also exceed the polymer relaxation time (or, for fluids with multiple modes, the longest relevant relaxation time in the spectrum). If the viscous component of the liquid is too strong, the filament deforms too slowly and elastic stresses relax before the exponential regime can be established. Conversely, if the deformation rate is too high, inertial effects may interfere (Rodd, Scott, Cooper-White, & McKinley, 2005). It is also important to note that the relaxation time extracted from CaBER is not always identical to the longest molecular relaxation time of a polymer solution. Instead, it emerges from the evolving stress balance within the filament: as thinning proceeds, chains with progressively shorter relaxation times are recruited, and the elasto-capillary regime only establishes once sufficient elastic stress has accumulated to counteract capillary pressure (Calabrese, Shen, & Haward, 2025). The measured timescale thus represents an effective quantity arising from this dynamic recruitment of modes, rather than a single intrinsic property of the fluid, and can therefore be sensitive to filament geometry and the initial conditions of the experiment (Miller, Clasen, & Rothstein, 2009). These considerations define the practical limits of CaBER in characterizing viscoelastic liquids.

1.2 State of the art

The previous section reviewed the fundamental principles governing electrospinning, emphasizing how solution, process, and ambient parameters determine fiber formation. It also introduced the Capillary Breakup Extensional Rheometer (CaBER) as a tool to characterize

the extensional rheological properties of low-viscosity polymer solutions. Building on this foundation, this state of the art section examines recent studies to reveal the limitations of current approaches and challenges that remain unresolved. This discussion is organized around four themes that directly motivate the contributions of this thesis: 1) the design and optimization of CaBER instruments, 2) the influence of controlled environments and solvent evaporation during CaBER experiments, 3) the role of molecular weight distribution and long-chain content on extensional rheology and electrospinnability, and 4) strategies for scaling up electrospinning through multi-needle arrays. Together, these subsections outline the current frontiers of research and define the gaps that the subsequent chapters of this thesis aim to address.

1.2.1 CaBER Machine

Capillary Breakup Extensional Rheometry (CaBER) has become a widely adopted technique for probing the extensional rheological response of polymer solutions through the controlled formation and capillary-driven failure of a liquid bridge. Commercially, the most widely known device was the HAAKE CaBER (Thermo Fisher Scientific), which for many years provided a benchmark for laboratory studies but is no longer available (Thermo Fisher Scientific Inc., 2007). More recently, specialized systems such as the TriMaster (Trijet Ltd., 2025) have been developed, primarily for ink-jet and coating applications, though they remain niche instruments rather than broadly distributed rheometers. Consequently, most current research relies on custom-built devices or on discontinued HAAKE instruments, resulting in considerable diversity in design and operation. In parallel, the scarcity of commercial options has also motivated the development of low-cost or portable variants, including a portable field rheometer (Seymour) (Collett et al., 2015; Hallmark et al., 2016), other lab-scale or portable device (Marshall, 2017; Rozali, Paterson, Hindmarsh, & Huffman, 2019; Shabaniverki, Alvarez-Valdivia, & Juárez, 2019), and even smartphone applications for filament tracking (Marshall, Liedtke, Todt, & Walker, 2017; Swift, 2018). These efforts reflect the creativity of the community and the growing demand for accessible extensional rheometry, but such devices

can lack the precision, calibration, and environmental control required for advanced research on complex polymer solutions.

From these diverse implementations, several key lessons have emerged regarding the requirements for reliable CaBER measurements. Some instruments, such as the commercial HAAKE CaBER, use a laser micrometer to measure filament thinning. This approach is simple and cost-effective, but it provides only a one-dimensional signal. However, subsequent studies have demonstrated that high-speed imaging is essential, as it captures filament asymmetry, transient instabilities, and enables a more rigorous definition of the thinning location, capabilities that are crucial for precise rheological characterization (Ng & Poole, 2021). Equally important is the control of the step-stretch protocol, since the solution properties extracted from CaBER are sensitive to experimental parameters including plate diameter, initial gap, stretch ratio, and actuation speed (Miller et al., 2009). Typical implementations use plates of 2 to 6 mm in diameter, initial gaps of 1 to 3 mm, and final separations three to four times larger than the initial gap. For more liquid systems, rapid actuation is required to form a measurable filament before breakup occurs, yet precision in displacement and timing must still be maintained. In practice, this corresponds to completing a step stretch of approximatively 10 mm within 50 ms (Riazi, Abbasi, Klein, Naue, & Wilhelm, 2020). Together, these insights define the practical requirements for a CaBER apparatus and serve as a specification framework for designing instruments capable of producing reproducible and interpretable measurements. These requirements are recalled at the beginning of Chapter 4, where they serve as the design specifications for the CaBER rheometer developed in this work.

It is also important to position CaBER relative to other extensional rheometry techniques that rely on monitoring the thinning of a capillary bridge to extract extensional properties. One such method is the Dripping-onto-Substrate (DoS) technique, in which a pendant drop is gently brought into contact with a flat substrate. Wetting of the surface forces the droplet to break into two, thereby forming a liquid bridge whose thinning can be analyzed (Jelena Dinic, Biagioli, & Sharma, 2017; J. Dinic, Jimenez, & Sharma, 2017; J. Dinic, Zhang, Jimenez, & Sharma, 2015; Zinelis, Abadie, McKinley, & Matar, 2024). DoS is particularly effective for very low-

viscosity fluids and short relaxation times, conditions under which a conventional CaBER cannot reliably establish a stable filament. However, the method is limited in its ability to impose sufficient stretching on the sample, reducing its capacity to characterize more viscous or strongly elastic liquids. Similarly, the Slow Retraction Method (SRM) involves placing a drop of liquid between two plates and then retracting one plate slowly, so that a liquid bridge is drawn out under quasi-static conditions (Campo-Deaño & Clasen, 2010). This technique offers more stable filament formation, as it avoids the rapid liquid transfer that occurs in DOS when the droplet wets the substrate. However, it suffers from a similar drawback in that it provides little control over the imposed deformation.

Another rheometry technique is the Rayleigh–Ohnesorge Jetting Extensional Rheometer (ROJER), that generates filaments by imposing controlled perturbations on a continuous liquid jet, which destabilizes into a sequence of beads connected by thinning ligaments (Ardekani, Sharma, & McKinley, 2010; Keshavarz et al., 2015; Mathues, Formenti, McIlroy, Harlen, & Clasen, 2018). This method enables measurements at very short relaxation times and for dilute, weakly elastic fluids, where CaBER filaments break too quickly. However, ROJER requires continuous sample injection so larger fluid volumes, and the flow field is more complex, making it less practical for systematic studies compared to CaBER. Furthermore, ROJER is a more complex instrument to develop, build and operate than CaBER, which limits its accessibility.

Each of these methods occupies a specific niche within extensional rheology, and CaBER is particularly well adapted to small sample volumes and semidilute polymer solutions, where filaments can be formed and extensional elasticity probed under conditions relevant to electrospinning. Despite these advantages, CaBER results remain highly sensitive to instrument design and operating protocols, which underlines the importance of carefully documented and reproducible setups. Chapter 4 therefore presents the construction of a custom CaBER with controlled actuation and calibrated high-speed imaging, developed to enable reliable characterization of low-viscosity polymer solutions.

1.2.2 CaBER in Controlled Environment

Most CaBER studies have been performed under ambient laboratory conditions, where solvent evaporation, humidity, and temperature are rarely controlled. This is problematic because the large surface-to-volume ratio of CaBER filaments makes them highly sensitive to mass and heat transfer effects. Although surprisingly little literature addresses this point directly, the limited studies that do exist clearly demonstrate its importance.

Immersion experiments by Sousa and co-workers demonstrated that surrounding the filament with an immiscible oil layer could reduce solvent loss by evaporation (Sousa, Vega, Sousa, Montanero, & Alves, 2017). Colby has further argued that for volatile solvents, the apparent exponential thinning observed in CaBER can be dominated by solvent diffusion through a concentrated surface layer, meaning that the extracted relaxation time may reflect evaporation dynamics rather than intrinsic viscoelasticity (Colby, 2023). Robertson and Calabrese introduced an evaporation-controlled dripping-onto-substrate (DoS) setup and showed that solvent vapor saturation strongly alters thinning behavior in volatile systems: in open air, rapid evaporation can produce surface films and apparent gelation, whereas under saturated conditions the thinning curves more faithfully represented the polymer solution response (Robertson & Calabrese, 2022).

The parallels with electrospinning are immediate. In both processes, a polymer solution filament undergoes extensional deformation while exposed to ambient air. Just as humidity and solvent vapor content strongly affect electrospinning jet stability, solidification, and fiber morphology, they also alter CaBER measurements by conflating rheological elasticity with evaporation-induced viscosity increases. Unlike electrospinning, however, controlled-environment CaBER studies remain rare. This gap not only limits quantitative connections between extensional rheology and fiber formation but also constrains the ability to obtain intrinsic rheological properties of volatile solutions.

Chapter 5 addresses this issue by coupling controlled-environment CaBER experiments with an evaporation model, enabling quantification of evaporation-driven strain-hardening while decoupling these effects from the intrinsic material response.

1.2.3 Extension Rheology: Impact of Long Chains

In capillary thinning, viscous stresses oppose breakup only proportionally to viscosity, but the presence of long polymer chains and their entanglements generates elastic stresses that can prolong filament lifetime by orders of magnitude beyond what viscosity alone would predict. Even at low concentrations, a small fraction of high-molecular-weight chains within a distribution can dominate the late-stage dynamics, delaying breakup and producing measurable strain hardening in CaBER experiments (Amarouchene, Bonn, Meunier, & Kellay, 2001; Lindner & Wagner, 2009). Early studies demonstrated that broadening the molecular weight distribution (MWD) or blending polymers of different chain lengths significantly increases apparent relaxation times and extensional elasticity (Entov & Hinch, 1997; Plog, Kulicke, & Clasen, 2005). To further probe these effects, so-called Boger fluids have been employed to isolate elastic contributions in extensional flows (Colman P. Carroll, 2006; Gupta et al., 2015; Yu et al., 2006). More recent analyses have emphasized that chain recruitment during filament thinning occurs progressively across the MWD, such that CaBER does not measure a single relaxation time but a hierarchy of molecular responses (Calabrese et al., 2025).

In Chapter 6, these factors are examined within a unified experimental framework that connects molecular characteristics to both extensional flow behavior and fiber formation. The role of high-molecular-weight chain content and distribution is evaluated in terms of their influence on filament thinning dynamics, extensional relaxation times, and electrospinnability. Beyond clarifying these fundamental relationships, the work also demonstrates practical strategies, such as elastic doping, that enable fiber formation from otherwise unspinnable low-molecular-weight polymers, while achieving a fivefold increase in polymer throughput.

1.2.4 Electrospinning Scale-Up

While electrospinning has become an established technique for producing polymeric nanofibers at the research scale, its translation to industrial production remains limited. A single needle typically yields on the order of 0.01–2 g/h of deposited polymer (Omer, Forgach,

Zelko, & Sebe, 2021), a rate well suited for laboratory studies but clearly insufficient for large-scale applications. This low production yield leads to high costs and constrains the industrial adoption of electrospinning despite its scientific and technological importance.

One approach to scale-up is needleless electrospinning, where jets are initiated directly from a free liquid surface (Y. Li et al., 2021; Yan, Niu, & Lin, 2019). This method can produce nanofibers at significantly higher rates, and commercial implementations such as the Nanospider system (Elmarco, Czech Republic) have demonstrated its potential for pilot-scale operation. Nevertheless, needleless systems face drawbacks compared with needle-based electrospinning, including broader fiber diameter distributions and premature solvent evaporation from the free liquid surface. In addition, they do not permit the production of complex fiber architectures such as core–shell fibers (Yan et al., 2019).

As a result, considerable attention has also been given to multi-needle electrospinning, which in principle allows a straightforward and scalable extension of single-needle setups (I. G. Kim, Lee, Unnithan, Park, & Kim, 2015). This strategy preserves the versatility of laboratory-scale electrospinning while promising higher yields. In practice, however, multi-needle arrays suffer from poor production quality due to Coulombic repulsion between the charged jets and needles that leads to an uneven electric field distribution along the multiple needle array. As the electric field is the driving force pulling and stretching polymeric jets, this non-uniformity precludes the reliable production of high-quality fibers in multi-needle systems (Theron, Yarin, Zussman, & Kroll, 2005).

Numerous researchers have tried to address these electric field issues using varying needle arrangements (Zhu et al., 2018) and needle spacing (Liu & Guo, 2013), adding a dielectric material around the needles (Zhu et al., 2019), changing needle-to-collector distances (Zheng et al., 2020), complementing coaxial needles with compressed air flow (Zheng et al., 2019; Zheng et al., 2020), and even applying a different voltage to each needle (Liu & Guo, 2013). Other approaches include the introduction of auxiliary electrodes placed perpendicularly to the needles (Xie & Zeng, 2012), cylindrical electrodes surrounding the needles (G. Kim, Cho, &

Kim, 2006), and even ring-shaped electrodes (Varesano, Carletto, & Mazzuchetti, 2009; Ying Yang et al., 2010) in attempts to improve the quality of deposited fibers. Despite considerable effort, none of these embellishments has been able to yield the robust uniformization of the electric field required for reproducible large-scale operation.

Chapter 7 addresses this challenge by introducing parallel auxiliary electrode plates that confine the needle array. Experimental observations and finite element models confirm that these electrodes homogenize the electric field along the array, greatly improving jet stability and fiber uniformity. This approach enables scaled-up, high-yield electrospinning while maintaining the product quality expected from single-needle operation.

CHAPTER 2

OBJECTIVES

The main objective of this work is to evaluate the physics of electrospinning scale-up by tailoring the rheological properties of polymer solutions and optimizing the electric field distribution in multi-needle systems. The specific objectives are divided into two complementary parts:

A. To evaluate the importance of rheology for electrospinning, through the following steps:

A1. To design and construct a custom Capillary Breakup Extensional Rheometer (CaBER) suitable for low-viscosity, viscoelastic polymer solutions used in electrospinning.

A2. To improve the reliability of CaBER measurements for volatile polymer solutions by minimizing experimental artifacts, with a particular focus on solvent evaporation, in order to isolate the intrinsic rheological response.

A3. To assess the influence of polymer formulation (molecular weight distribution and long-chain content) on extensional rheology and electrospinnability, and to demonstrate elastic doping as a practical scale-up tool.

B. To scale-up electrospinning using multi-needle system, through the following steps:

B1. To mitigate electric field non-uniformities in multi-needle systems in order to reduce jet interference and stabilize fiber production.

CHAPTER 3

METHODOLOGY

This chapter presents the general methodology followed throughout the thesis. It first outlines the overall research strategy, highlighting how the specific objectives are organized into complementary paths leading to the main objective of scaling up electrospinning. The materials used throughout this study are then described together with their preparation protocols, followed by the processes and characterization techniques employed across the research chapters.

3.1 Research Strategy

The main objective of this thesis is to evaluate the physics of electrospinning scale-up by tailoring the rheological properties of polymer solutions and optimizing the electric field distribution in multi-needle systems. To achieve this, two complementary research paths were pursued, as summarized in the methodological flowchart presented in Figure 3.1.

The first path (A) focuses on controlling the rheological properties of polymer solutions, characterized using Capillary Breakup Extensional Rheometry (CaBER). Three sub-objectives were defined:

(A1) the development of a custom CaBER device, designed with precise actuation and high-speed optical imaging to reliably capture the filament thinning dynamics of low-viscosity, viscoelastic polymer solutions typical of electrospinning

(A2) the improvement of CaBER reliability through controlled-environment experiments and evaporation–diffusion modeling to quantify and correct for solvent evaporation effects on filament thinning, and

(A3) the evaluation of polymer formulations, including molecular weight distribution and elastic doping, to demonstrate how solution rheology can be tuned to enhance fiber formation and production throughput.

The second path (B) addresses the electric field interference problem in multi-needle electrospinning. While multi-needle setups provide a straightforward route to increasing production yield, their implementation is hindered by non-uniform electric field distributions that destabilize jets and compromise fiber quality. To overcome this limitation, the research objective (B1) is pursued through the design and validation of auxiliary electrode configurations that homogenize the electric field along a linear needle array. Their effectiveness was assessed through finite element simulations and experimental electrospinning trials.

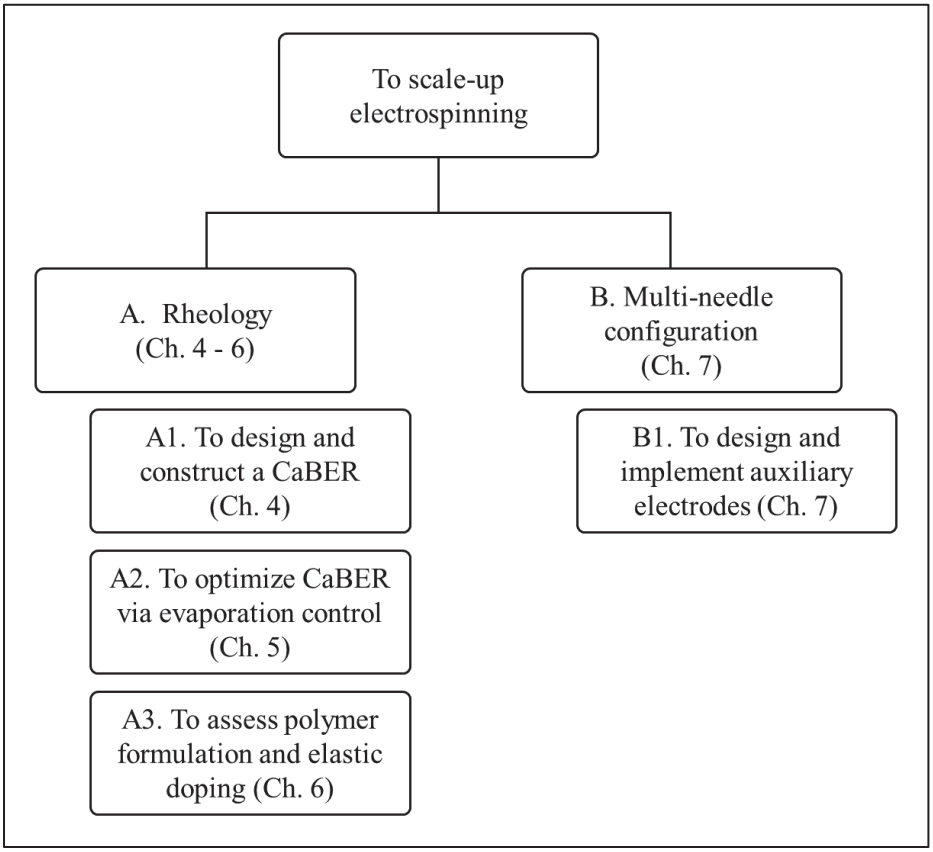

Figure 3.1 Methodological flowchart for the scale-up of electrospinning, mapping the objectives to their corresponding thesis chapters

3.2 Materials

All polymers and solvents used in this thesis are summarized in Table 3.1.

Poly(ethylene glycol) (PEG) and poly(ethylene oxide) (PEO) samples were purchased from Sigma-Aldrich (St. Louis, MO, USA). The PEG used in all formulations had a weight-average molecular weight (M_w) of 35,000 g/mol. The PEO samples covered a range of number-average molecular weights (M_n) of 100,000; 300,000; 600,000; 900,000; and 4,000,000 g/mol. Blends of PEO and PEG (Boger fluids) were also prepared for selected experiments, with compositions described in Chapter 5.

Silicone oils were kindly provided free of charge by Dow Chemical (Midland, MI, USA) under the trade name XIAMETER™ PMX-200. Three grades were used without further modification: 200 cSt, 350 cSt, and 1000 cSt.

Pullulan powder (manufactured by Hayashibara Co., Ltd., Okayama, Japan; distributed by Nagase) was dissolved in distilled water at concentrations between 10 and 25 wt%. Solutions were stirred on a hot plate at 60 °C for 4 h, followed by a 30 min cool down at room temperature.

Polyvinylidene difluoride (PVDF) powder (Kynar 741, Arkema, King of Prussia, PA, USA) was dissolved in a binary solvent mixture of 70% N,N-dimethylformamide (DMF) and 30% acetone (Fisher Scientific, Fair Lawn, NJ, USA) to obtain an 18 wt% solution. The solution was stirred at 70 °C for 4 h on a hot plate and cooled for 30 min under continued stirring before use.

Detailed formulations and processing conditions are described in the corresponding chapters.

Table 3.1 Overview of materials, solvents, and preparation protocols

Material	Supplier	Grade	Solvent System	Preparation Protocol	Chapter Used
PEG	Sigma-Aldrich (USD)	M_w $[g/mol]$ $35k$	Water	Stirred at 60°C, 4h; cooled 1h	Ch. 4 & 6
PEO	Sigma-Aldrich (USD)	M_n $[g/mol]$ $100k, 300k, 600k, 900k, 4M$	Water	Stirred at 60°C, 4h; cooled 1h	Ch. 4 & 6
Silicone Oils (XIAMETER PMX-200)	Dow Chemical (USD)	200, 500, 1000 cSt	-	Used as recived	Ch. 4,
Pullulan	Nagase (Japan)	-	Water	Stirred at 60°C, 4h; cooled 30min	Ch. 5,
PVDF (Kynar 741)	Arkema (USD)	-	70% DMF / 30% Acetone	Stirred at 70°C, 4h; cooled 30min	Ch. 7,

3.3 Process and Characterization

This section presents the processing and characterization techniques employed throughout this thesis. Emphasis is placed on methods that are used across multiple research chapters, including electrospinning with the L-100 system, morphological analysis of fibers by scanning electron microscopy (SEM), shear rheology with the Anton Paar MCR 302 rheometer, and surface tension measurements using a VCA Optima goniometer in pendant drop mode. While

detailed experimental parameters are provided within each research chapter, the following subsections summarize the equipment and general protocols common to the work.

3.3.1 L-100 Electrospinning

Electrospinning experiments were performed using a FLUIDNATEK L-100 system (Bionicia, Paterna, Valencia, Spain). Polymer solutions were dispensed through integrated syringe pumps connected to 21-gauge stainless-steel needles. High voltages were applied between the needle and the collector, and fibers were deposited on aluminum foil substrates. The integrated environmental control unit of the L-100 was used to regulate the temperature and humidity inside the electrospinning chamber (108 x 84 x 85 cm^3), with temperature maintained at 21 °C for all experiments. Steady-state conditions were typically reached within 1h, and all experiments were conducted only after equilibrium was achieved. In addition to single-needle operation, the multi-needle configuration of the L-100 was employed for scale-up studies, with details provided in Chapter 7.

3.3.2 Scanning Electron Microscopy

Fiber morphology was characterized using scanning electron microscopy (SEM). Two instruments were employed across different experiments: a TM3000 tabletop SEM (Hitachi High-Technologies, Tokyo, Japan) or a Hitachi S3600 SEM (Hitachi, Ltd., Tokyo, Japan). Prior to imaging, samples were sputter-coated with a thin layer of gold using an Emitech K550X coater (Quorum Technologies, Laughton, UK) operated at 30 mA for 2 minutes. Fiber diameters were measured from SEM micrographs using ImageJ software (version 1.53a, NIH, Bethesda, MD, USA). For each sample, between 50 and 100 measurements were taken across multiple images, and the mean diameter with standard deviation was reported.

3.3.3 302 Rheometer

Steady-shear viscosity measurements were performed using an Anton Paar MCR 302 rotational rheometer equipped with a concentric cylinder geometry (bob diameter 16.7 mm, cup diameter 18 mm). All measurements were conducted at 21 °C, and viscosity was recorded as a function of shear rate.

3.3.4 Pendant Drop

Surface tension measurements were performed using a VCA Optima goniometer (AST Products, Inc.) operated at 21 °C. Drops were formed by suspending the polymer solutions from a 27-gauge stainless steel needle, which also served as a scale reference for image calibration. For each solution, ten images were acquired. Image analysis was conducted using Fiji (ImageJ version 1.53a, NIH, Bethesda, MD, USA) with the pendant drop plugin, fitting the drop profile to the Young-Laplace equation. An example of a drop is presented in Figure 3.2 The reported surface tension corresponds to the mean of the ten measurements.

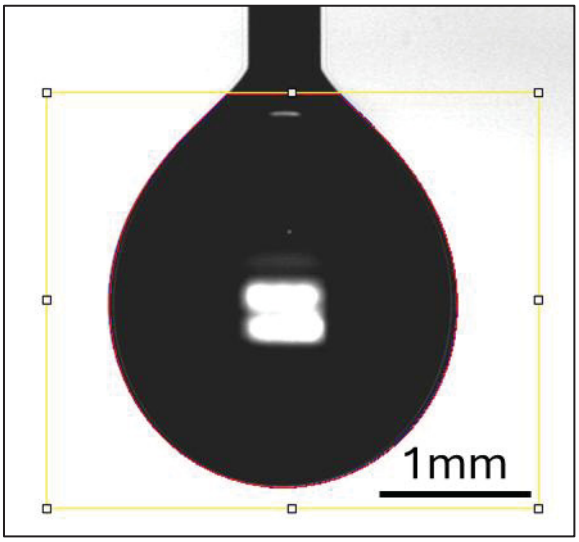

Figure 3.2 Surface tension measurement by the pendant drop method; the yellow box indicates the region of interest used for analysis, the blue line traces the detected edge of the drop, and the red line shows the fitted drop contour according to the Young-Laplace equation

CHAPTER 4

Custom Capillary Breakup Extensional Rheometer

This chapter addresses the first component (A1) of the first research objective of this thesis: to design and construct a custom Capillary Breakup Extensional Rheometer (CaBER) suitable for low-viscosity, viscoelastic polymer solutions used in electrospinning. This chapter details the design and implementation of a custom-built Capillary Breakup Extensional Rheometer (CaBER), developed to characterize the extensional rheological properties of low-viscosity liquids. Section 4.1 describes the CaBER device and its subsystems, including the mechanical structure, electronic control components, optical acquisition system, and image analysis procedures. Section 4.2 presents model experiments used to validate the system's performance, including tests on Newtonian silicone oils and viscoelastic polymer solutions.

The design of the custom CaBER was guided by requirements and specifications identified from previous implementations (Section 1.2.1). These criteria can be grouped according to the main subsystems of the device; in this list, *must* denotes essential requirements for reliable operation, while *should* indicates recommended specifications that improve performance and repeatability:

Mechanical stretching unit

- The apparatus must accommodate plate diameters in the range of 2–6 mm.
- The apparatus must allow initial gaps of 1–3 mm and stretch ratios of 3–4.
- The design should minimize misalignment and mechanical vibrations to improve repeatability across experiments.

Electrical control system (actuation)

- The actuator must achieve a complete step stretch of at least 10 mm in less than 50 ms to enable measurements on low-viscosity liquids.
- The actuator must provide precise control of displacement and timing to ensure repeatability of the stretch protocol.

- The control system must incorporate basic safety functions (e.g., emergency stop, motion limits) to protect both users and equipment.
- The control system should allow flexible programming of stretch protocols for different experimental conditions.

Optical imaging system

- The device must include high-speed imaging that provides sufficient temporal and spatial resolution for characterization of filament thinning dynamics.
- The optical setup should capture filament asymmetry, transient instabilities, and the thinning location.
- The imaging system should allow adjustable magnification to optimize resolution across filament sizes.

Image analysis method

- The system must allow consistent extraction of filament diameter from high-speed recordings.
- The analysis workflow should enable automated tracking to improve repeatability and reduce operator bias.

These requirements and specifications framed the design strategy and guided the development of the subsystems described in Section 4.1.

4.1 Description of the Capillary Breakup Extensional Rheometer

The custom-built Capillary Breakup Extensional Rheometer (CaBER) enables the formation of a liquid filament (capillary bridge) and its visual monitoring to quantitatively analyze extensional rheology. A schematic representation of the device is presented in Figure 4.1, and a 3D model is shown in Figure 4.2.

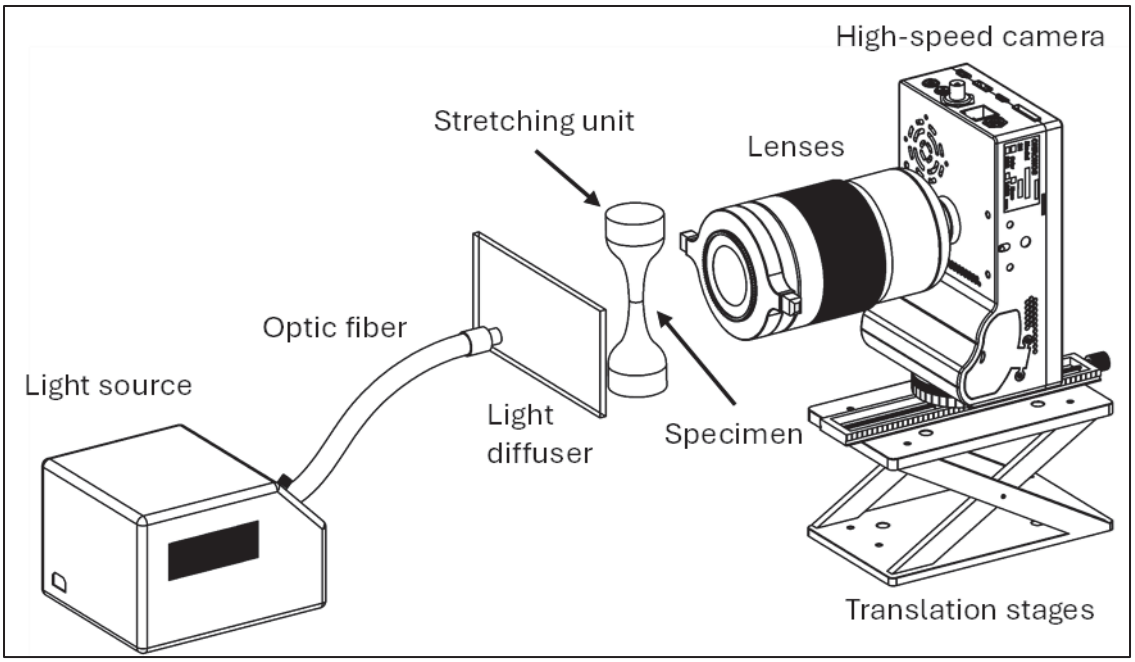

Figure 4.1 Schematic of the custom-built CaBER

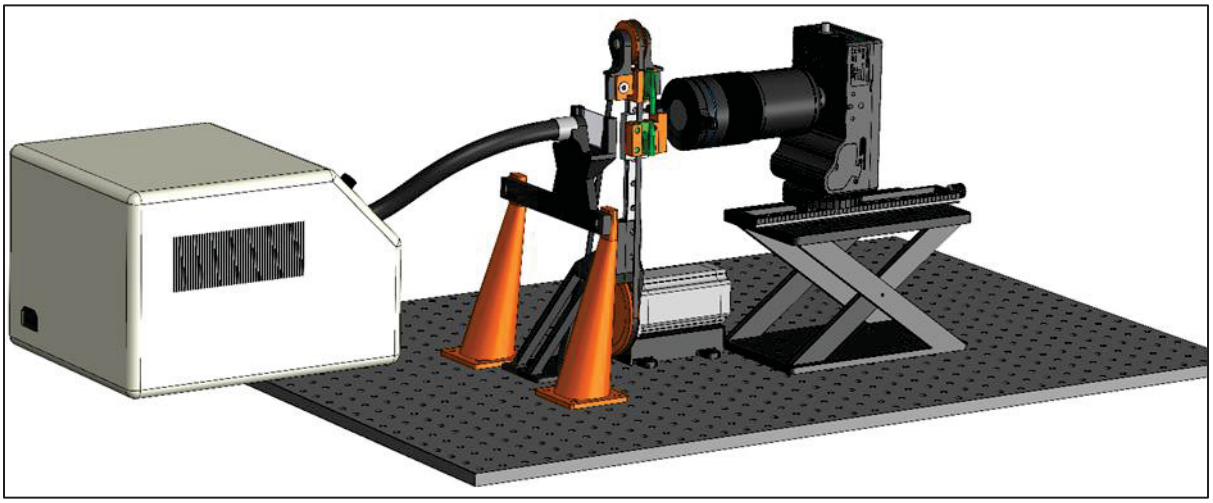

Figure 4.2 3D model of the custom-build CaBER device

During each test, a small volume of polymer solution is loaded between two parallel circular plates. The bottom plate is rapidly displaced downward to stretch the liquid sample into a filament, while the top plate remains fixed. The evolution of the filament's mid-diameter is tracked over time using high-speed imaging. This thinning dynamic is then used to determine the rheological characteristics of the liquid.

The CaBER device integrates four main subsystems: mechanical stretching, electrical control, optical imaging, and image analysis, each of which is detailed in the following sections. A detailed bill of material, including specific details about each component of the designed CaBER is presented in APPENDIX I.

4.1.1 Mechanical Stretching Unit

The mechanical stretching unit converts the rotational motion of a stepper motor into the linear vertical displacement of the bottom plate. The top plate remains fixed and serves as a positional reference during each test. The system is designed to ensure plate parallelism, rigid alignment, and rapid motion throughout operation. A 3D rendering of the stretching unit is shown in Figure 4.3, including an angled view a) and a cross-sectional view b).

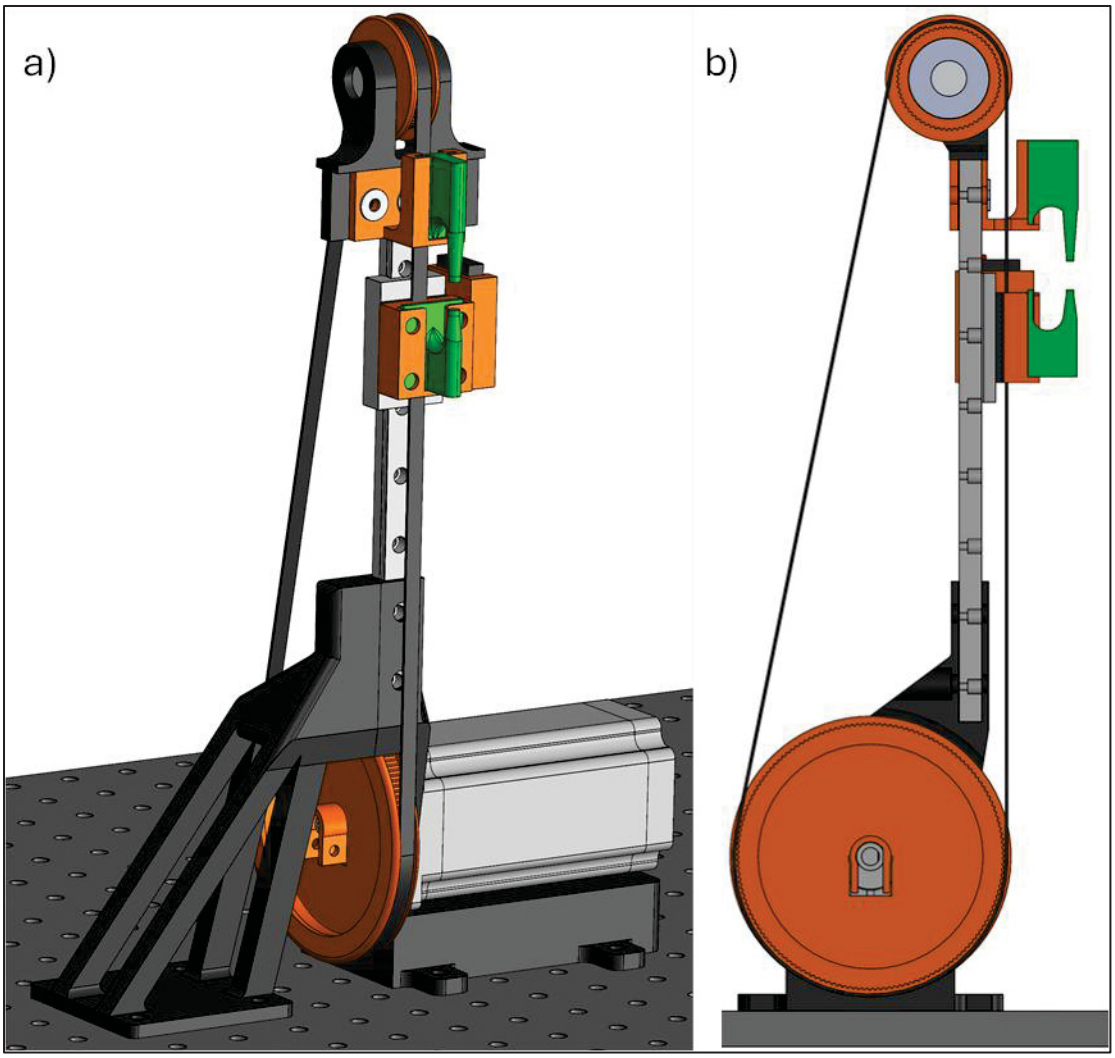

Figure 4.3 Mechanical stretching system of the CaBER: a) angled 3D view, b) cross-sectional view

At the core of the system is a vertical linear translation rail, mounted on an optical breadboard through a custom support. A carriage (slider) moves along the rail and is connected to a timing belt loop, which transmits torque from a stepper motor located at the bottom of the structure. The transmission uses two gears: the bottom gear is directly coupled to the motor shaft, while the top gear is mounted on a ball bearing and rotates freely. The belt is attached to the carriage, converting motor rotation into linear vertical motion.

The bottom plate is mounted on the moving carriage, while the top plate is fixed to the upper rail assembly. During each test, the sample is manually loaded between the plates, and the stepper motor rapidly lowers the bottom plate to form a liquid filament. The top plate remains stationary, ensuring that the initial position is constant across experiments. A limit switch is installed on the carriage to detect its top position and reset the system before each trial.

The plates are easily interchangeable, allowing the user to vary parameters such as plate diameter and initial inter-plate distance. This modularity also facilitates cleaning between experiments.

The tension in the belt can be adjusted through the upper rail assembly, which includes an adjustable mounting bracket connected to the rail. This feature ensures smooth motion and prevents slippage during rapid acceleration.

The custom parts of the mechanical stretching unit were designed in SolidWorks and 3D-printed in polylactic acid (PLA) using fused deposition modeling (FDM), with printed components shown in green, orange, and black in Figure 4.3. All other elements, including the stepper motor, linear rail, ball bearings, timing belt, and limit switch, were purchased as standard commercial components due to their functional or electrical roles.

4.1.2 Electrical Control System

The electrical control system delivers controlled, rapid, and precise rotation of the stepper motor, which is mechanically converted into the vertical displacement of the bottom plate. A schematic of the system architecture is shown in Figure 4.4.

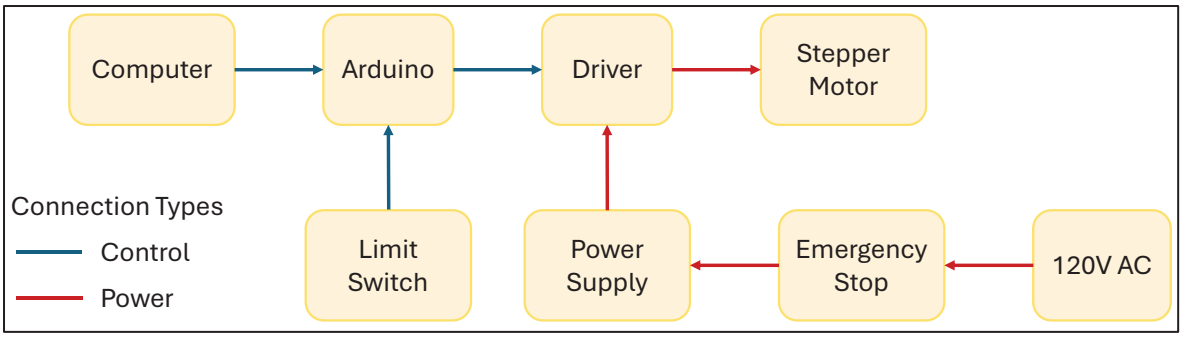

Figure 4.4 Electrical wiring diagram of the CaBER system, showing control (blue) and power (red) connections

The CaBER electrical system is divided into two functional loops: power delivery and motion control. The power loop begins at a standard 120 V AC outlet, which is routed through a mushroom-type emergency stop switch for safety. Power is then supplied to a regulated 24 V, 6.5 A switching power supply (150 W max), which feeds a digital stepper motor driver (rated up to 5.6 A). The driver controls a NEMA 23 stepper motor (maximum torque 3.0 Nm), responsible for actuating the mechanical stretching unit.

The control loop is based on an Arduino Mega 2560 microcontroller, which generates step pulses for the driver. A mechanical limit switch, mounted on the carriage, provides positional feedback and ensures a consistent top reset position before each test. The Arduino receives commands via USB from a host computer. Motion is controlled by modulating the delay between motor steps, which defines the rotational speed. The Arduino program (provided in APPENDIX II) allows the user to specify the total displacement length (in motor steps), as well as the velocity, acceleration, and deceleration profiles.

To optimize the CaBER motion profile, preliminary tests were conducted without liquid, using high-speed imaging to track the distance between the plates over time during actuation. Figure 4.5 compares two sets of displacement profiles, each corresponding to a 1 mm to 8 mm plate separation, tested under different motion strategies. In Figure 4.5a, no acceleration or deceleration was applied; a constant time delay between motor steps was used to command a nominally constant velocity. However, due to the system's dynamic limitations, the actual plate

response deviates from the ideal motion. The black curve shows a fast motion that results in significant overshoot and pronounced oscillations around the final position. At a slower commanded speed (red curve), wave-like oscillations occur throughout the motion, likely due to mechanical resonance, and similar overshoot and oscillation patterns are observed at the end of travel. These behaviors indicate poor dynamic stability and can significantly impair the CaBER's ability to test liquids, by increasing the plate stabilization time and introducing disturbances into the liquid, which can negatively affect filament formation, particularly for low-viscosity samples.

To address these limitations, acceleration and deceleration ramps were implemented in the motion program. Figure 4.5b presents the evolution of the inter-plate gap for two stretching velocities, both exhibiting smooth trajectories with controlled acceleration and deceleration phases. The fastest motion profile (black curve) achieves the full displacement in 35 ms, while the slowest (red curve) completes the stretch in 75 ms. This slower profile was selected as the standard for subsequent experiments, as it provides sufficiently rapid motion for filament formation while minimizing abrupt movements that could disturb low-viscosity liquids, even when plate motion is mechanically smooth. This approach improves the robustness and repeatability of filament formation across a broad range of solution types.

To vary the total plate displacement while maintaining smooth motion, the program takes advantage of the velocity profile's segmented design: an initial acceleration ramp, a constant-speed region, and a final deceleration ramp. The displacement is adjusted by changing the number of motor steps in the central linear segment, without altering the ramp profiles. This structure ensures that different stretching distances can be applied while preserving the smooth acceleration and deceleration phases essential for dynamic stability.

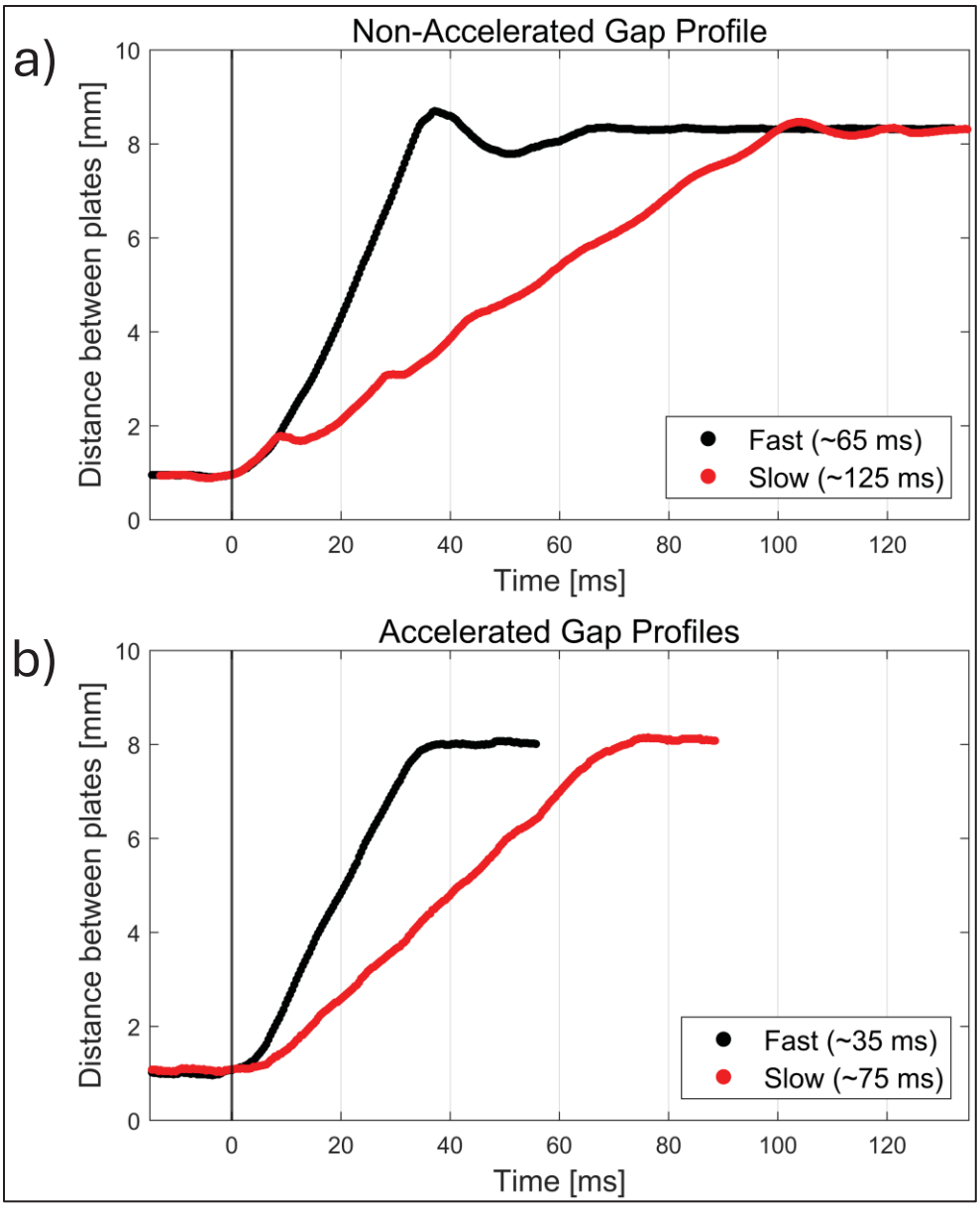

Figure 4.5 Distance between CaBER plates during actuation from 1 mm to 8 mm gap; a) motion without programmed acceleration; the black curve shows a fast profile with overshoot and oscillations, stabilizing after ~65 ms; the red curve, with slower steps, exhibits wave-like oscillations throughout the motion and stabilizes after ~125 ms; b) motion with programmed acceleration and deceleration; both profiles achieve smooth displacement with no overshoot or oscillations; the black curve stabilizes in ~35 ms, while the red curve, used in subsequent experiments, reaches a stable position within ~75 ms

4.1.3 Optical Imaging Setup

The optical system was designed to capture high-resolution, time-resolved images of the thinning filament formed during CaBER experiments. High-speed imaging was performed using a Chronos 2.1-HD camera, equipped with a Laowa 100 mm f/2.8 ultra-macro lens. A Raynox macro converter was optionally added to increase magnification when required.

To ensure proper illumination, uniform backlighting was provided by a MI-152 fiber optic illuminator coupled to a ½" optical fiber, held in place by a custom 3D-printed support. The light was diffused through a translucent screen positioned behind the filament.

The camera was mounted on a micro-positioning system composed of a Huanyu Z-axis manual lift platform, a NiSi NM180S macro focusing rail, and a Sunwayfoto GC-01 geared tripod head, stacked in series and mechanically coupled via custom-designed adaptors. This setup provided precise multi-axis adjustment for accurate and repeatable focusing.

Focus was first adjusted by observing the apex of a sessile drop using a wide lens aperture, which created a shallow depth of field. This condition, combined with numerical magnification on the camera preview, allowed for precise identification of the focal plane. Once the focus was optimized, the aperture was reduced to increase depth of field, and the illumination intensity was adjusted to ensure consistent image quality during acquisition. This method ensured that the system remained sharply focused even under the most demanding optical conditions. This approach ensured robust focusing accuracy, since the focal plane was adjusted under the most demanding optical conditions, ensuring sharp imaging during experiments. Typical exposure time was 200 μs, with frame rates ranging from 100 to 2500 fps depending on the experiment.

To calibrate spatial resolution, an image of a microscope calibration slide was captured after focus adjustment, as shown in Figure 4.6a. The slide includes markings every 0.1 mm, with larger labels every 1 mm, allowing accurate conversion between pixels and physical

dimensions. At maximum magnification, the optical system of the CaBER reaches a spatial resolution of approximately 300 pixels/mm, corresponding to a maximum measurable precision of ~3.3 μm. Additionally, a 0.2 mm optical fiber was photographed (Figure 4.6b) to fine-tune image thresholding parameters for cylindrical transparent objects. Details of the thresholding and image analysis procedures are presented in Section 4.1.4.

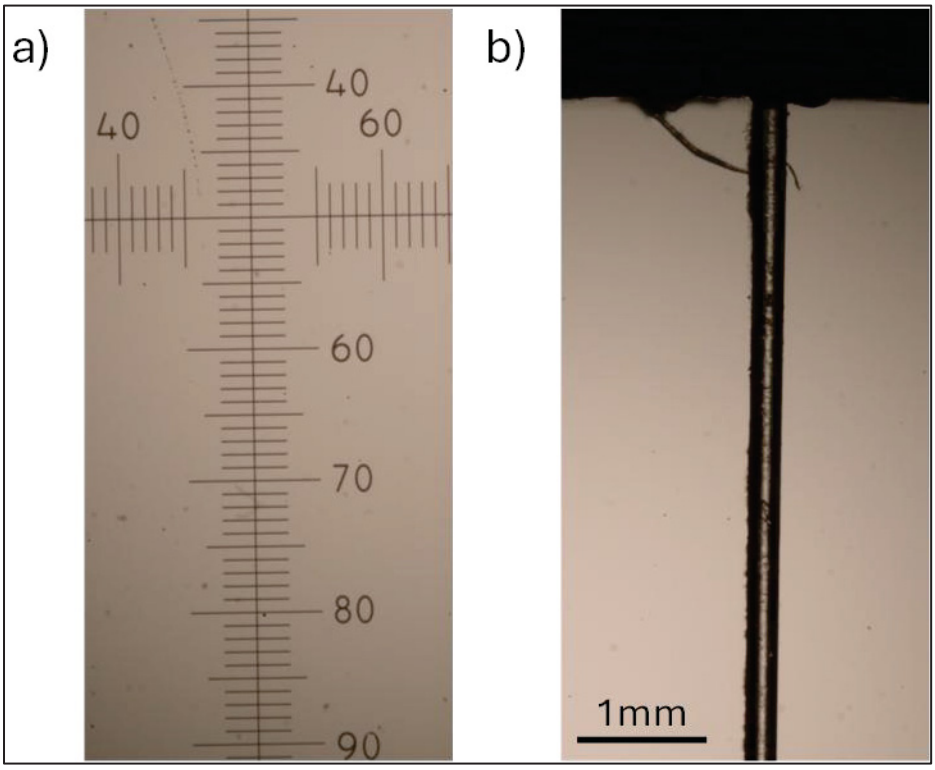

Figure 4.6 Optical calibration procedure: a) image of the microscope calibration slide, featuring markings every 0.1mm and larger labels every 1mm, used for special calibration; b) optical fiber used for intensity threshold adjustment

4.1.4 Image Analysis Method

Image analysis is used to extract quantitative measurements of filament diameter over time, D(t), from high-speed photographs captured during CaBER experiments. These diameter-time curves are used to fit rheological models and extract key fluid properties, such as relaxation time and viscosity.

A custom MATLAB program (available in APPENDIX III) processes each image in the sequence sequentially. For every frame, the filament diameter is extracted, and the resulting $D(t)$ data are compiled for direct use in model fitting. The time corresponding to each frame is calculated based on the frame rate set during image acquisition, as defined by the camera settings. To reduce measurement uncertainty, the analysis is automatically terminated once the filament diameter drops below 10 pixels, corresponding to approximately 34 μm at maximum magnification.

The diameter extraction procedure consists of four main steps, illustrated in Figure 4.7 and detailed below:

a) Grayscale Conversion: The raw color image is converted to grayscale to reduce data dimensionality and simplify subsequent thresholding and edge detection.

b) Binarization: A calibrated intensity threshold, previously selected to give accurate diameter measurements of a transparent 0.2 mm optical fiber under same optical conditions, is applied to generate a black-and-white image.

c) Edge Detection and ROI Selection: The program identifies the filament edges one side at a time by scanning each row of pixels in the binarized image. For the left edge, it examines each row starting from the leftmost pixel and moves inward until it encounters the first bright pixel, which is recorded as the filament boundary at that height. The same procedure is then applied from the right side, scanning each row from the rightmost pixel towards the left to locate the corresponding edge. The detected edge positions are then plotted as a function of vertical height. To ensure reliable measurements, a region of interest (ROI) is manually defined around the central portion of the filament, typically corresponding to the liquid bridge, where the filament is well-formed and free from visual artifacts.

d) Diameter Profile and Extraction: The local filament diameter is calculated as the distance between the detected left and right edges at each vertical position within the ROI. These values

form a diameter profile along the filament height, from which a single representative diameter is extracted for each image. Depending on the fluid behavior, the program is configured to select one of two criteria for extracting a representative diameter. For Newtonian fluids that exhibit a necked, hourglass-shaped profile, the minimum diameter within the ROI is typically used. For elastic fluids that form nearly cylindrical filaments, the most frequent diameter value (statistical mode) is more appropriate. The mode offers greater robustness against local artifacts, as it reflects the most commonly occurring measured diameter across the ROI. In the example shown in Figure 4.7d, the diameter profile exhibits a plateau at the thinnest section of the filament. The mode value, 51 pixels, accurately captures this plateau and serves as a reliable diameter measurement for this specific image.

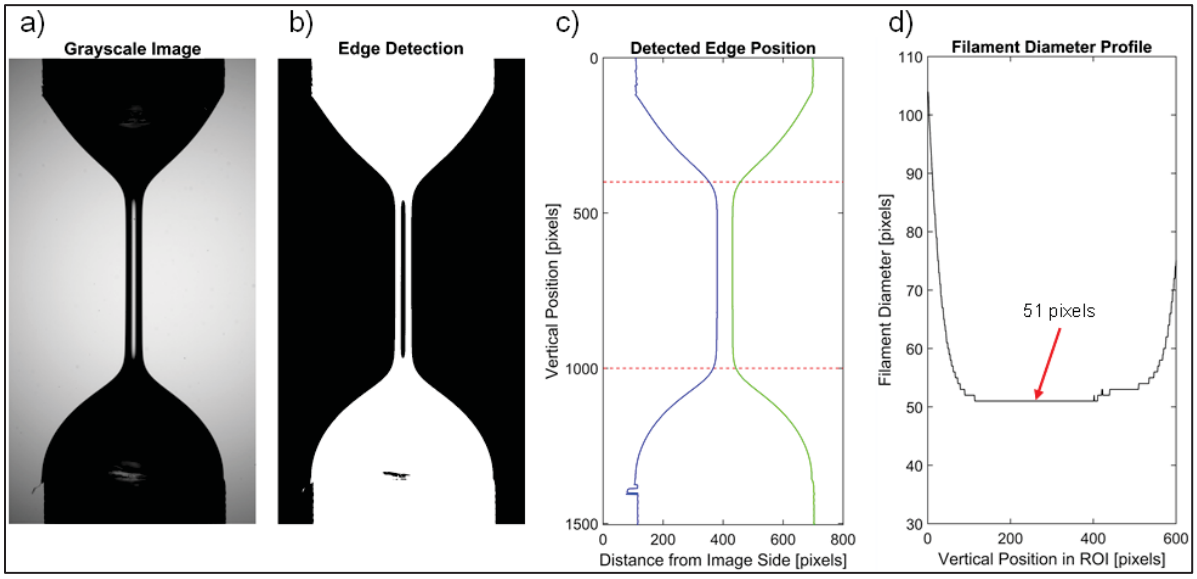

Figure 4.7 Image analysis method for extracting filament diameter from high-speed CaBER image;. a) image converted to grayscale; b) binarized image obtained by applying a manually calibrated intensity threshold, determined using a 0.2 mm optical fiber for calibration; c) detected left (blue) and right (green) edge positions as a function of vertical height; the region of interest (ROI), indicated by dashed red lines, defines the zone used for diameter extraction; d) filament diameter profile within the ROI; in this example, the representative filament diameter is taken as 51 pixels, as indicated by the red arrow in d); the solution analyzed is referred to as Boger fluid #2 in later sections of this work: it is composed of 25 wt% polyethylene glycol (PEG, $M_w \approx 35{,}000$ g/mol) and 0.1 wt% polyethylene oxide (PEO, $M_n \approx 900{,}000$ g/mol) in water

4.2 Model Experiments

This section presents model experiments designed to both validate the CaBER device and illustrate its application for viscoelastic fluids. First, the system's accuracy was evaluated by measuring the viscosity of Newtonian silicone oils with known properties, providing a direct benchmark against reference values. Then, its ability to capture elastic behavior was demonstrated using aqueous polyethylene oxide (PEO) solutions at varying concentrations, from which relaxation times were extracted.

Representative high-speed images of filament evolution for both fluid types are shown in Figure 4.8. Panel a) shows a Newtonian silicone oil (500 mPa·s), which forms an hourglass-shaped filament with the smallest diameter at mid-height, and was used to verify viscosity measurements against a known reference. Panel b) shows a 2 wt% PEO solution in water, producing the nearly cylindrical filament shape typical of elastic liquids, from which the relaxation time can be determined.

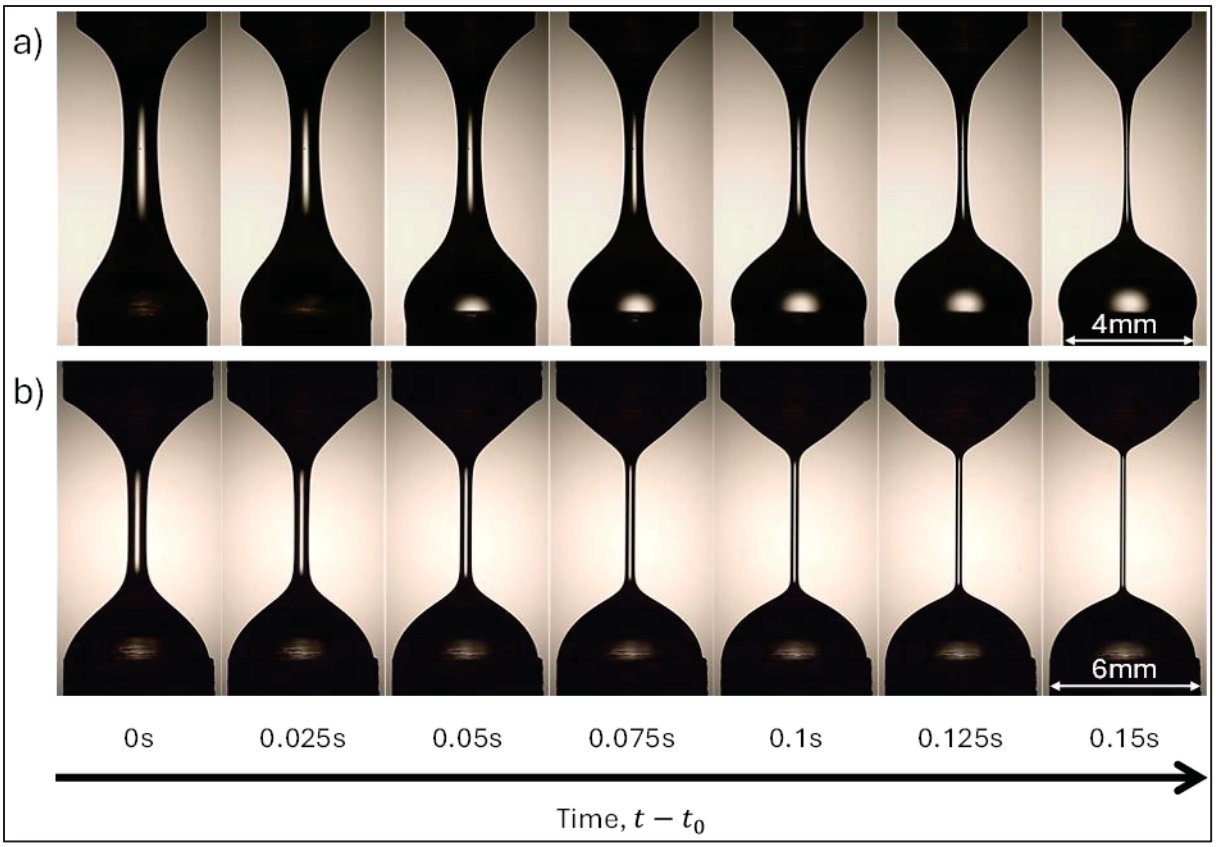

Figure 4.8 Representative high-speed images of filament evolution during CaBER experiments; a) newtonian silicone oil (500 mPa·s) forming an hourglass-shaped filament, used to verify viscosity measurement against a known reference; test performed with 4 mm plates, initial gap 2 mm, final gap 8 mm, imaged at 2000 fps; b) 2 wt% PEO solution in water forming a nearly cylindrical filament, typical of elastic liquids from which relaxation time can be determined; test performed with 6 mm plates, initial gap 2 mm, final gap 10 mm, imaged at 2500 fps; in both cases, t_0 corresponds to the end of the plate motion, so that time represents the free filament evolution

Examples of filament diameter evolution D(t), extracted from image analysis of high-speed photographs taken with the CaBER, are presented in Figure 4.9. In Figure 4.9a, three silicone oils exhibit progressively slower thinning rates with increasing viscosity. The dashed lines represent fits to Papageorgiou's analytical solution for the viscous-dominated regime (Equation (1.1)), which predicts that the minimum filament diameter decreases linearly with time in the final approach to pinch-off. In all cases, the data progressively approach this linear decay as transient effects subside. For the highest-viscosity oil, these initial transients are more pronounced, but the later-stage thinning aligns well with the model. The resulting viscosities

are compiled in Table 4.1, alongside their nominal grade values and shear viscosities measured by rotational rheometry. The CaBER-derived values agree well with the references, confirming the system's ability to reliably characterize Newtonian viscosity.

Figure 4.9b presents the D(t) curves for PEO solutions at 1%, 2%, and 3% wt in water. Unlike Newtonian oils, these viscoelastic fluids exhibit exponential thinning behavior, with all three datasets fitted by the exponential model described in Eq. 2 (dashed lines in Figure 4.9b). Transient effects are also visible at early times, particularly for the highest-concentration solution (red line), where the formation of the elasto-capillary regime is delayed by the higher solution viscosity. The relaxation time λ for each formulation was obtained from these fits in the elasto-capillary regime. The extracted relaxation times increase with polymer concentration, consistent with the higher degree of chain entanglement and elastic resistance to capillary thinning at elevated solid content. This trend demonstrates that CaBER can quantitatively resolve differences in extensional elasticity among low-viscosity viscoelastic solutions.

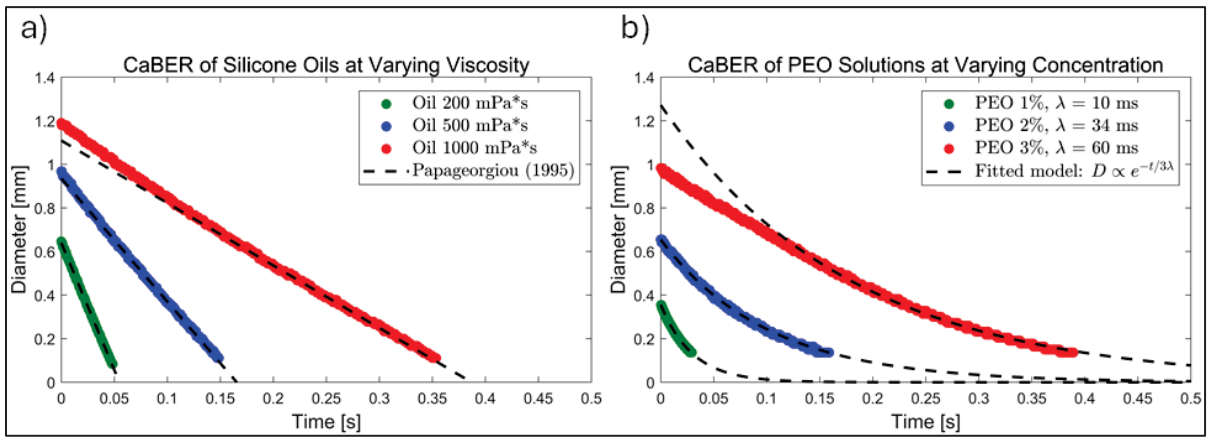

Figure 4.9 Examples of filament diameter evolution *D(t)*, extracted from image analysis of high-speed photographs taken with the CaBER; a) newtonian silicone oils of 200, 500, and 1000 mPa*s; dashed lines indicate fits to Papageorgiou's analytical model (Equation (1.1)) for the viscous-dominated regime, used to extract Newtonian viscosity; b) viscoelastic PEO solutions at 1, 2, and 3 wt% in water; eashed lines indicate exponential fits (Equation (1.2)) used to extract the relaxation time λ for each formulation

Table 4.1 Viscosity of Newtonian silicone oils determined by CaBER compared with their nominal grade values and shear viscosities measured using a rotational rheometer

Oil grade [mPa*s]	**Shear viscosity [mPa*s]**	**CaBER shear equivalent [mPa*s]**
200	213	244
500	537	514
1000	1078	1034

Altogether, these model experiments demonstrate that the custom-built CaBER rheometer can reliably measure extensional viscosity in Newtonian fluids and relaxation time in viscoelastic solutions, confirming its suitability for the rheological characterization of low-viscosity liquids undergoing extensional deformation.

CHAPTER 5

SOLVENT EVAPORATION INDUCES STIFFENING IN CABER AND ELECTROSPINNING OF VOLATILE POLYMER SOLUTIONS

Étienne J. Beaudoin[a], Ricardo J. Zednik[a] and Nicole R. Demarquette[a],

[a]Department of Mechanical Engineering, École de Technologie Supérieure,
1100 Notre-Dame West, Montreal, Quebec, Canada H3C 1K3

Paper submitted for publication, August 2025

5.1 Introduction

This chapter is based on the work submitted for publication in August 2025 in *Rheologica Acta* and addresses the second component (A2) of the first research objective of this thesis: to improve the reliability of CaBER measurements for volatile polymer solutions by minimizing experimental artifacts, with a particular focus on solvent evaporation. In this context, electrospinning involves rapid jet stretching and solidification through solvent loss, while Capillary Breakup Extensional Rheometry (CaBER) provides an analogous platform to probe the extensional flow behavior of polymer solutions. However, solvent evaporation during CaBER thinning experiments can artificially increase the measured relaxation times of polymer solutions, conflating intrinsic viscoelasticity with evaporation-induced strain hardening.

In this chapter, the influence of solvent evaporation on extensional rheology probed by CaBER is examined through a combined experimental and modeling study. Controlled-environment electrospinning and CaBER experiments with aqueous pullulan solutions are compared to quantify the effect of ambient vapor pressure on fiber morphology and filament thinning dynamics. Electrospinning results show that lower vapor pressure accelerates solvent evaporation, leading to earlier jet solidification and the formation of thicker fibers. In parallel, CaBER measurements reveal longer relaxation times at low vapor pressure, consistent with evaporation-induced strain hardening. To interpret these results, a coupled evaporation–

diffusion model is presented to simulate the development of polymer concentration gradients across the filament radius during thinning, arising from solvent loss at the surface. This model enables the calculation of apparent filament viscosity during thinning, demonstrating that low vapor pressure steeply increases viscosity near the surface and leads to significant deviations from the intrinsic extensional response.

Together, these findings demonstrate that solvent evaporation drives strain-hardening behavior in CaBER in much the same way it does in electrospinning. They highlight the need for careful environmental control and evaporation-aware modeling to ensure accurate rheological characterization of volatile polymer solutions

5.2 Experimental Results

Electrospinning experiments were conducted at controlled relative humidities of 25%, 50%, 75%, and 90%, while maintaining identical processing parameters. Figure 5.1 presents SEM micrograph of the electrospun samples obtained at each humidity level, alongside with the corresponding fiber diameters and standard deviations, where applicable.

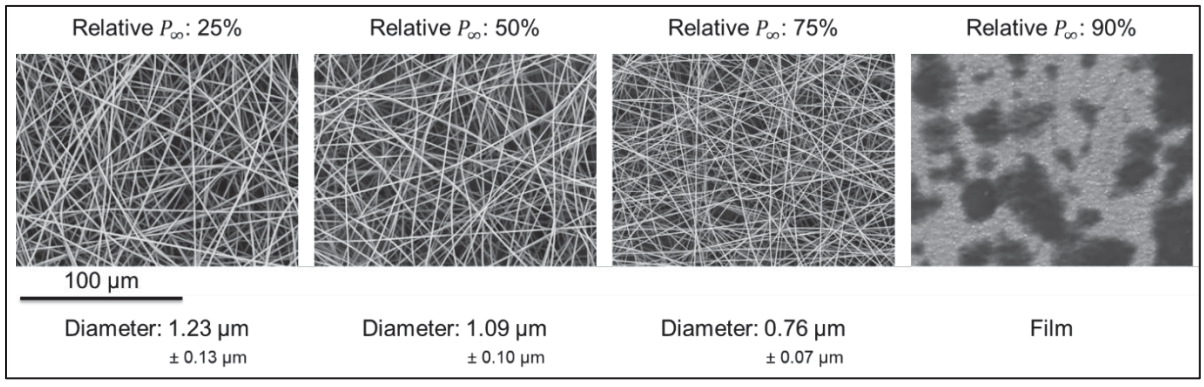

Figure 5.1 Scanning electron micrographs and diameter analysis of electrospun fibers obtained at different ambient relative solvent vapor pressure P_∞ (25%, 50%, 75%, and 90%); electrospinning was performed using a 22 wt% aqueous pullulan solution at 21°C, with a flowrate of 1mL/h and an applied voltage of 18kV; fibers were collected at 25 cm below the needle tip

As the solvent vapor pressure in the surrounding air increases, the evaporation rate decreases, allowing the jet to remain fluid for a longer duration. This delay in solidification gives the jet more time to stretch, which results in thinner fibers. However, a limiting condition is reached when solidification does not occur before the jet reaches the collector. In such cases, the still-liquid jet merges upon deposition, leading to the formation of a continuous film rather than discrete fibers, as observed at 90% relative humidity in this specific case. These results are consistent with previous studies investigating the effect of ambient humidity on electrospinning of aqueous polymer solutions (Mailley, Hébraud, & Schlatter, 2021; Pelipenko, Kristl, Jankovic, Baumgartner, & Kocbek, 2013; Tripatanasuwan et al., 2007).

Capillary Breakup Extensional Rheometry (CaBER) measurements were conducted under controlled ambient relative solvent vapor pressures, corresponding to 25%, 50%, 75%, and 90% of the solvent's saturation pressure at 21 °C. To control the CaBER environment, the entire system was enclosed in a plexiglass chamber (54 x 53 x 78 cm^3). The system calibration was validated using Newtonian silicone oils, presented in APPENDIX IV, Figure-A IV-1 and APPENDIX IV, Table-A IV-1. Relative humidity was adjusted by modulating the output of a humidifier placed inside that chamber. Humidity levels and temperature were monitored using a digital thermos-hygrometer positioned near the filament thinning region. Steady-state conditions were typically reached within 5 min, and all measurements were performed only after equilibrium was achieved. Figure 5.2a presents a representative CaBER experiment for pullulan solution at low vapor pressure (25%), which serves as the model case for the evaporation-concentration simulation discussed later. The evolution of the filament midpoint radius over time displays two distinct regimes: (1) an initial linear decay phase, corresponding to the visco-capillary thinning regime, followed by (2) a nonlinear exponential thinning regime where elastic effects dominate. The blue line corresponds to a linear fit of regime (1), while the red line shows the exponential fit used in regime (2) to extract the extensional relaxation time.

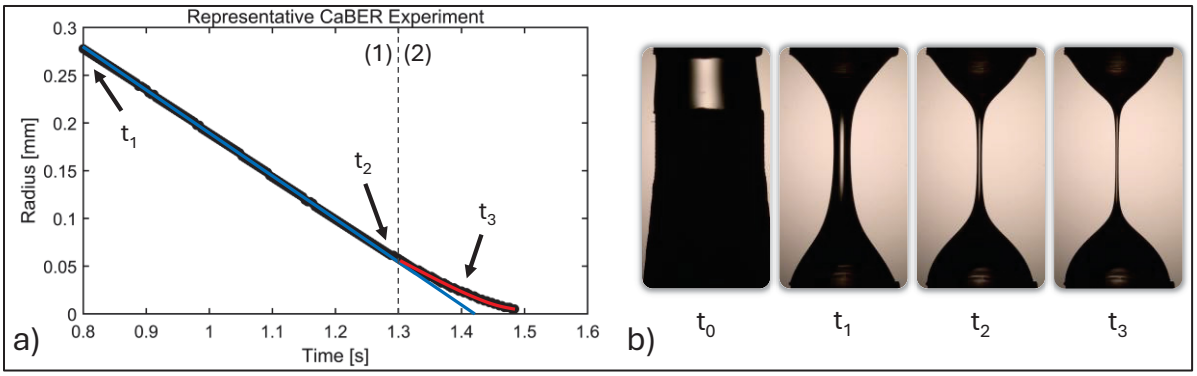

Figure 5.2 a) representative CaBER measurement of a 22 wt% aqueous pullulan solution at 25% relative solvent vapor pressure; the filament radius as a function of time exhibits an initial linear thinning regime (fit shown in blue), followed by an exponential regime (fit shown in red) used to extract the relaxation time; key time points (t_1 to t_3) are marked on the curve with arrows; a semi-log scale version of this plot is available in APPENDIX IV, Figure-A IV-3; b) corresponding high-speed images of the filament at selected time points (t_0 to t_3), including the initial configuration (t_0); this dataset serves as the reference case for the theoretical modeling of solvent evaporation presented in the discussion section

Figure 5.2b presents high-speed images of the filament at selected time points, labeled t_0 through t_3, with corresponding positions marked on the x-axis of Figure 5.2a. These snapshots provide visual reference for the filament evolution and serve as the basis for computing local polymer concentration and viscosity changes in the modeling section.

To assess the impact of evaporation conditions on the thinning dynamics, the relaxation time was measured using the same CaBER procedure under different relative solvent vapor pressures. Figure 5.3 summarizes the relaxation times extracted from these fits. To obtain those results, plates with a diameter of 4 mm and initial gap of 2mm were used. A total of five displacement amplitudes were applied: 4.5, 5.0, 5.5, 6.0, and 6.5 mm, corresponding to final plate separations of 6.5 to 8.5 mm. These amplitudes were selected to span a representative range over which stable breakup dynamics could be recorded: excessively large steps can cause premature rupture before entering the elasto-capillary regime, whereas very small steps may lead to end effects or incomplete filament formation. This selection strategy was designed to probe multiple operating conditions across the stable regime and to avoid biasing the measured relaxation time toward a specific machine parameter. Each condition was repeated twice, for a total of ten measurements per humidity condition. An example of the step-stretch gap evolution

over time is presented in APPENDIX IV, Figure-A IV-2. The reported relaxation time represents the average of these measurements, with the standard deviation provided as error.

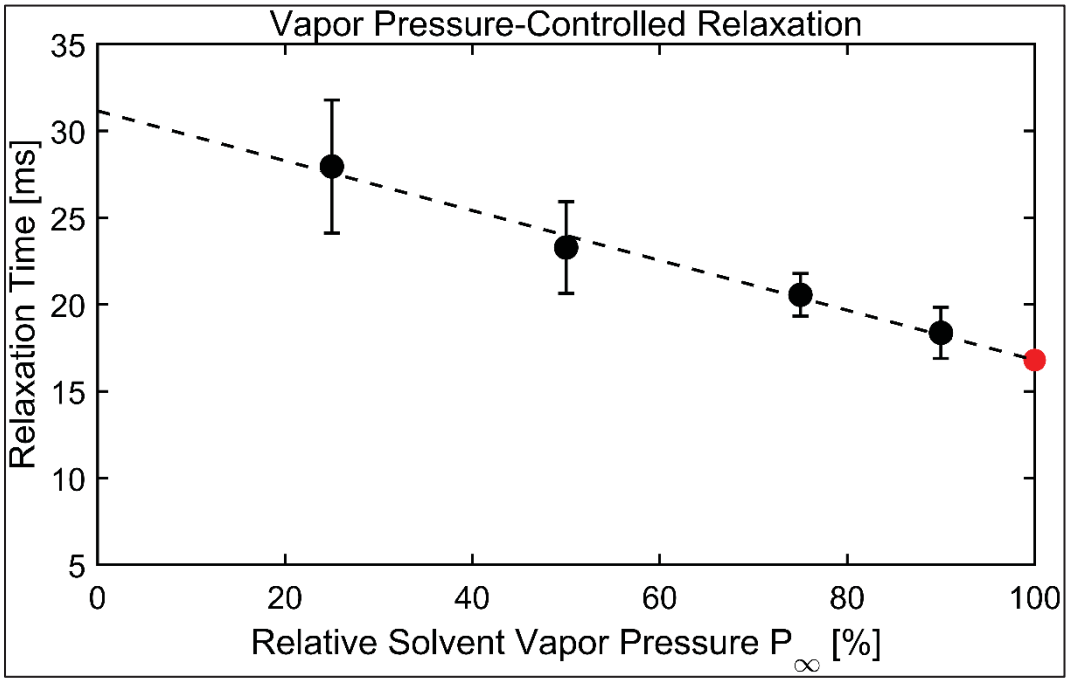

Figure 5.3 Extensional relaxation time measured by CaBER as a function of ambient relative solvent vapor pressure P_{∞}; error bars represent standard deviations; the dashed line indicates the linear extrapolation toward saturation conditions (P_{∞} corresponding to 100% relative vapor pressure), shown in red, where solvent evaporation is assumed to be negligible; the complete dataset used to compute the reported averages and standard deviations is provided in APPENDIX IV, Table-A IV-2

A clear decreasing trend in apparent relaxation time is observed with increasing solvent vapor pressure. This demonstrates that the relaxation time measured by CaBER is sensitive to the vapor environment, with higher solvent content in the air leading to shorter apparent relaxation times. Linear extrapolation suggests that the relaxation time at full saturation (100% relative vapor pressure, indicated in red in Figure 5.3) would be approximately 40% lower than that at ambient conditions (25% relative vapor pressure).

This behavior can be interpreted as a consequence of reduced solvent evaporation at higher vapor pressures. As the surrounding atmosphere becomes richer in solvent vapor, the evaporation rate decreases and the polymer concentration within the filament remains more

stable during thinning. Under such near-saturated conditions, the measured relaxation time approaches the intrinsic rheological response of the solution, largely unaltered by solvent loss. These results thus suggest that solvent evaporation induces a progressive stiffening of the filament, thereby influences the apparent CaBER measurement.

This behavior arises from the strong sensitivity of solution rheological properties to polymer concentration, which increases as solvent is lost during filament thinning. To quantify this effect, solutions with varying concentration were prepared and characterized for their viscosity. Figure 5.4 presents the measured zero-shear viscosity of pullulan solutions as a function of polymer concentration.

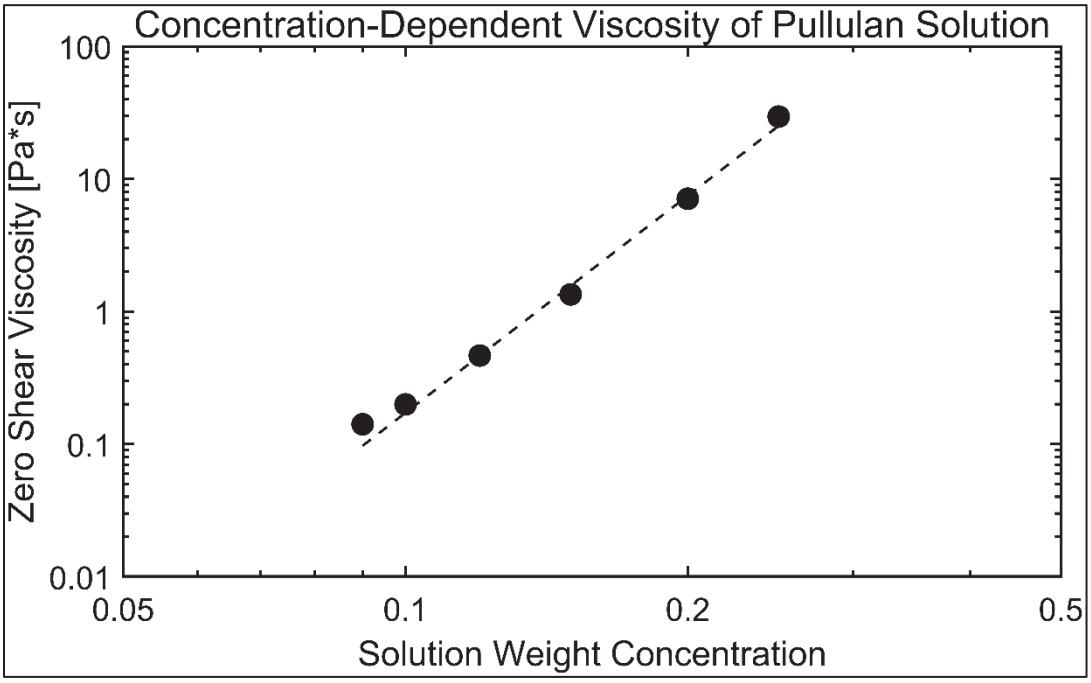

Figure 5.4 Zero-shear viscosity of pullulan solutions as a function of polymer concentration; viscosity values were taken at a shear rate of 1 s^{-1}, within the low-shear-rate Newtonian plateau where all solutions exhibited stable behavior indicative of their zero-shear viscosity; the complete steady-shear viscosity profiles are presented in APPENDIX IV, Figure-A IV-4

The data reveal an exponential increase in viscosity with increasing concentration, which is well approximated by the empirical expression:

$$\eta_0(C) = 47298 \times C^{5.439} \tag{5.1}$$

where η_0 is the zero-shear viscosity in Pa·s, C is the polymer concentration (mass fraction), the prefactor carries the units of viscosity, and the exponent is dimensionless. This relation provides a practical interpolation of the experimentally measured viscosities using an empirical fit over the studied concentration range, and was not intended to imply a theoretical dependence. While CaBER probes extensional rheological property of the solution rather than shear, an estimate of the Newtonian-like extensional viscosity, mainly observed during the early stages of the filament thinning, can be obtained by applying the Trouton ratio, given by:

$$\eta_e = 3\eta_s \tag{5.2}$$

where η_e is the extensional viscosity and η_s is the zero-shear viscosity taken in the linear low-shear-rate plateau (at 1 s^{-1}). This approximation does not capture the intrinsic strain hardening that arises from polymer chain entanglements, which dominates in the elasto-capillary regime during which the relaxation time is extracted. However, equation (5.1) and (5.2) provide a practical estimate of the concentration dependent apparent extensional viscosity of the pullulan solution use in this study. In the subsequent discussion section, this relationship is applied to a representative CaBER experiment, used as model case, to compute the cross-sectional average (i.e., bulk) apparent viscosity of the thinning filament, based on the evolving radial and time-dependent concentration profiles induced by solvent evaporation at the filament surface.

5.3 Discussion

To quantify the influence of solvent evaporation on filament thinning during CaBER experiments, a numerical model was developed and implemented using the experimentally measured filament radius $R(t)$ as input. The model simulates radial solvent diffusion within

the polymer solution filament, driven by concentration gradients resulting from solvent loss at the surface. By computing the evolving polymer concentration profiles across the filament radius over time, the model calculates the filament's bulk apparent extensional viscosity. This allows assessment of how solvent loss contributes to evaporation-induced stiffening under different solvent vapor pressure conditions. The governing equations are first presented, followed by the numerical parameters applied to the pullulan–water system. The resulting simulations provide insight into how solvent evaporation alters the rheological response of the filament during CaBER measurements.

The model is formulated in cylindrical coordinates assuming an axisymmetric geometry of infinite length, as illustrated in Figure 5.5. Let r denote the radial position and R the filament radius at time t.

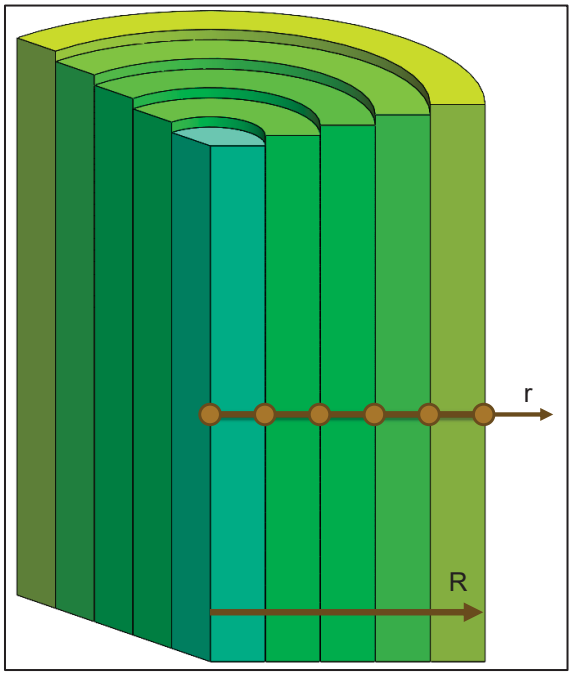

Figure 5.5 Schematic representation of the filament geometry and radial discretization for theoretical modeling; the filament radius R(t) and radial coordinate r are displayed; the cross-section is divided into concentric radial slices to numerically compute the evolving polymer concentration profile $\phi(r, t)$; brown dots represent the radial nodes at which concentration is evaluated; solvent evaporation occurs at the outer surface (i.e., $r = R(t)$); for clarity, the number of slices shown in the schematic is reduced; the simulation used 200 radial nodes and a time step of 10 μs to resolve the concentration evolution

Solvent evaporation occurs at the filament surface, leading to the following boundary condition, adapted from the formulation proposed by (Okuzono et al., 2006):

$$D\frac{\partial \phi}{\partial r} = J\phi(1-\phi) \;\; at\; r = R \tag{5.3}$$

where D is the solvent diffusion coefficient inside the jet and $\phi(r,t)$ is the polymer weight concentration.

Based on the derivations of (Wu, Salkovskiy, & Dzenisc, 2011), the evaporation coefficient J can be expressed using the mass transfer model:

$$J = \frac{k_g M_1}{R_g T \rho}(P_s - P_\infty) \tag{5.4}$$

where k_g is the gas-side mass transfer coefficient of water vapor into air, M_1 is molar mass of the solvent, R_g the universal gas constant, T the absolute temperature, ρ the solvent density, P_s the saturation vapor pressure of solvent at surface and P_∞ the partial vapor pressure in the surrounding air, calculated as $P_\infty = P_s \cdot RH$ here RH is the relative humidity (fractional form).

During the CaBER experiment, solvent evaporation is *dominated by diffusion* through the surrounding air since the gas phase is essentially quiescent and therefore convection plays a negligible role in vapor transport. As the filament radius decreases, diffusion path in air becomes shorter and vapor removal is enhanced, leading to faster evaporation for smaller radii. The mass transfer is therefore considered *purely diffusive*, but its intensity depends on the filament geometry. To account for this radius-dependent diffusion, the Sherwood number correlation is introduced to estimate the gas-side mass-transfer coefficient k_g:

$$\mathrm{Sh} = \frac{k_g(2R)}{D_g} = 2 + 0.6\,\mathrm{Re}^{1/2}\mathrm{Sc}^{1/3} \tag{5.5}$$

where $L = 2R$ is the characteristic length for a cylinder, D_g is the gas-phase diffusivity of water vapor in air, and Re and Sc are the Reynolds and Schmidt numbers, respectively. Under ambient conditions in air (Re ≈ 0.07, Sc ≈ 0.6), this gives Sh ≈ 2.1, consistent with the diffusion-dominated regime where Sh tends toward 2. The corresponding mass-transfer coefficient is therefore $k_g \approx 2.1D_g/(2R)$, with $D_g = 2.4 \times 10^{-5}\ \mathrm{m}^2/\mathrm{s}$.

At the filament centerline, symmetry requires a no-flux boundary condition:

$$\frac{\partial \phi}{\partial r} = 0 \ \ at\ r = 0 \tag{5.6}$$

The redistribution of solvent inside the filament is governed by Fick's second law of diffusion in cylindrical coordinates (Crank, 1975):

$$\frac{\partial \phi}{\partial t} = \frac{1}{r}\frac{\partial}{\partial r}\left(rD\frac{\partial \phi}{\partial r}\right) \tag{5.7}$$

The parameters, constants, and symbols used in this study are listed in Table 5.1.

Table 5.1 Input parameters and constants used for the solvent evaporation model

Symbol	Description	Value	Unit	Note / Reference
t	Time		s	
ϕ_0	Initial polymer concentration	0.22	(wt/wt)	Experimental condition
r	Radial coordinate		m	
R	Filament radius		m	Measured from images
k_g	Gas-side mass transfer coefficient of water vapor into air		m/s	(Wu et al., 2011) Estimated from the Sherwood number correlation
M_1	Solvent molar mass (water)	0.018	kg/mol	
R_g	Universal gas constant	8.314	$\frac{J}{(mol \cdot K)}$	
T	Absolute temperature	294.15	$Kelvin$	

Symbol	Description	Value	Unit	Note / Reference
ρ	Solvent density	998	kg/m^3	
P_s	Saturation vapor pressure (water)	2490	Pa	$P_s(T)$ (Incropera, DeWitt, Bergman, & Lavine, 2006)
P_∞	Ambient vapor pressure		Pa	$P_\infty = P_s \cdot RH$
D_g	Gas-phase diffusivity of water vapor in air	2.4×10^{-5}	m^2/s	(Incropera et al., 2006)
J	Evaporation coefficient		m/s	$J(P_\infty, k_g)$
D	Diffusion coefficient of water in pullulan solution	5×10^{-6}	m^2/s	Range for hydrophilic polymers solution (Incropera et al., 2006; Moon et al., 2024)
Δt	Time step	$min(10^{-5}, 0.125\ dr^2/D)$	s	Numerical parameter
N_r	Number of radial nodes	200	$-(qt)$	Numerical parameter

The evaporation coefficient J was calculated using Equation (5.4) by varying the ambient partial vapor pressure P_∞ to reflect the different relative vapor pressure conditions investigated experimentally.

A constant diffusion coefficient of water in the polymer solution was assumed, with a value of $D = 5 \times 10^{-10}\ m^2/s$. This value falls within the typical range of 10^{-9} to $10^{-10}\ m^2/s$ reported for solvent diffusion in hydrophilic polymer systems at comparable polymer concentrations (Moon et al., 2024).

To simulate the evolution of polymer concentration during filament thinning, the filament radius R(t) extracted from the reference CaBER experiment presented in Figure 5.2 was used to define the time-dependent geometry of the filament. Based on this evolving geometry, the polymer concentration profile $\phi(r, t)$ was computed using the discretization scheme described earlier.

Figure 5.6 displays a subset of the simulated concentration profiles, plotted along the normalized radial coordinate $\tilde{r} = r/R(t)$, from the filament center ($\tilde{r} = 0$) to the free surface ($\tilde{r} = 1$), under a relative solvent vapor pressure of 25%. Four time points were selected to illustrate the evolution: the initial configuration (R = 2.00 mm), two intermediate stages ($R = 0.1005\,mm$ and $R = 0.0375\,mm$), and the final measurable radius ($R = 0.0051\,mm$). This final point corresponds to the smallest reliably measured diameter, given the spatial resolution of the imaging setup. Simulated profiles are shown with distinct line colors, and corresponding filament images are inset using matching-colored borders for clarity.

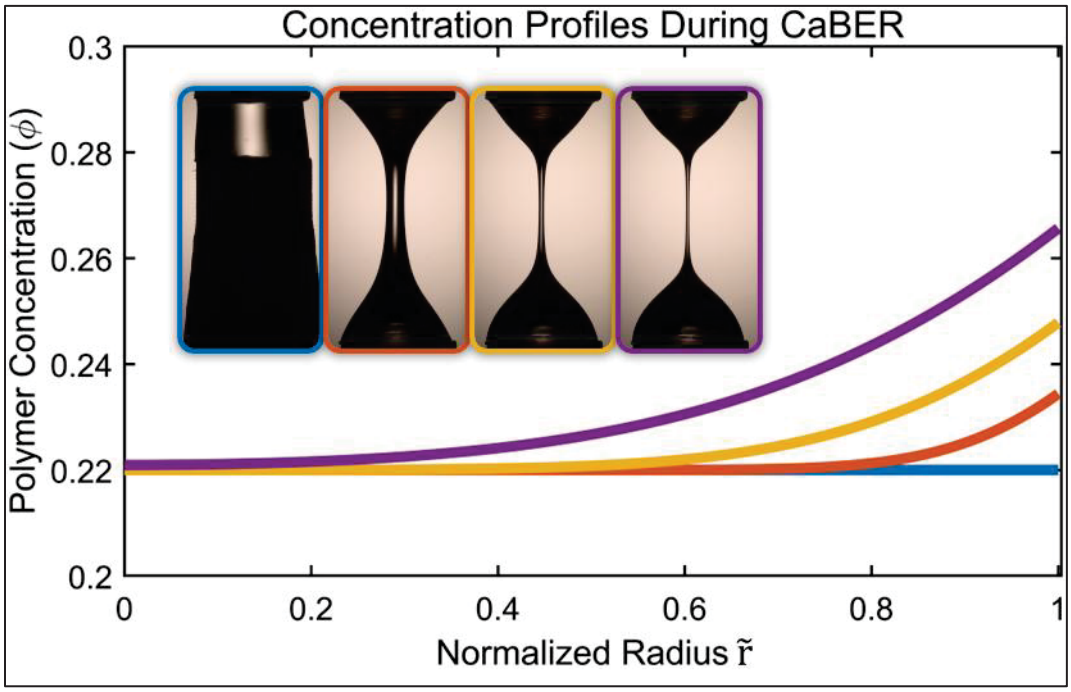

Figure 5.6 Simulated radial polymer concentration profiles during filament thinning in a representative CaBER experiment at 25% relative solvent vapor pressure; concentration profiles are plotted along the normalized radial coordinate $\tilde{r} = r/R(t)$, ranging from the filament center ($\tilde{r} = 0$) to the free surface ($\tilde{r} = 1$); four time points are shown: the initial configuration ($R = 2.00\,mm$), two intermediate stages ($R = 0.1005\,mm$ and $R = 0.0375\,mm$), and the final measurable radius ($R = 0.0051\,mm$); inset images display high-speed CaBER snapshots at the corresponding times, framed with color-matching borders for visual reference; the results illustrate the progressive inward growth of elevated polymer concentration due to surface evaporation and radial diffusion

At early stages of thinning, solvent evaporation leads to an increase in polymer concentration primarily near the free surface, while the filament core remains close to its initial composition. As the filament radius decreases over time, the surface-area-to-volume ratio increases, which intensifies solvent loss and exacerbates evaporation effects. In parallel, smaller filaments experience relatively stronger radial diffusion. Indeed, the reduced cross-sectional dimensions shorten the path length required for solvent molecules to reach the surface, thereby increasing the relative influence of diffusion on solvent redistribution. This geometric constraint accelerates solvent depletion within deeper layers of the filament, causing regions of elevated polymer concentration to progressively extend inward. By the final time point, the concentration begins to rise near the filament midpoint, highlighting the impact of solvent evaporation during CaBER characterization.

The concentration profiles shown in Figure 5.6 demonstrate how solvent evaporation induces a radial gradient in polymer content during filament thinning. To quantify the rheological consequences of this evolving composition, the solution viscosity was calculated at each radial position from the local polymer concentration using the exponential relationship established experimentally (Figure 5.4 and Equation (5.1)). These local viscosities were then averaged across the filament cross-section, weighted by the radial distribution, to obtain an apparent (bulk) viscosity at each time step. Extensional viscosity was subsequently estimated by applying the Trouton ratio (Equation (5.2)) to these averaged shear viscosity values. While this relation is most accurate in the initial thinning regime, it is employed here throughout the process to illustrate the qualitative impact of solvent loss on extensional rheology.

Figure 5.7 presents the evolution of the apparent extensional viscosity over time, calculated from the modeled concentration profiles, under different ambient relative solvent vapor pressures: 25%, 50%, 75%, and 90%. Since the filament radius R(t) decreases monotonically during thinning, time also reflects filament radius thinning. At low vapor pressure (e.g., 25%), a marked increase in apparent viscosity is observed as thinning progresses, consistent with evaporation-driven stiffening. The steepest rise occurs at late stages, when the filament radius is small, leading to a high surface-to-volume ratio and enhanced relative impact of diffusion

over short radial distances. In contrast, at high vapor pressure (e.g., 90%), the apparent viscosity remains nearly unchanged, indicating minimal solvent loss and little deviation from the initial polymer concentration.

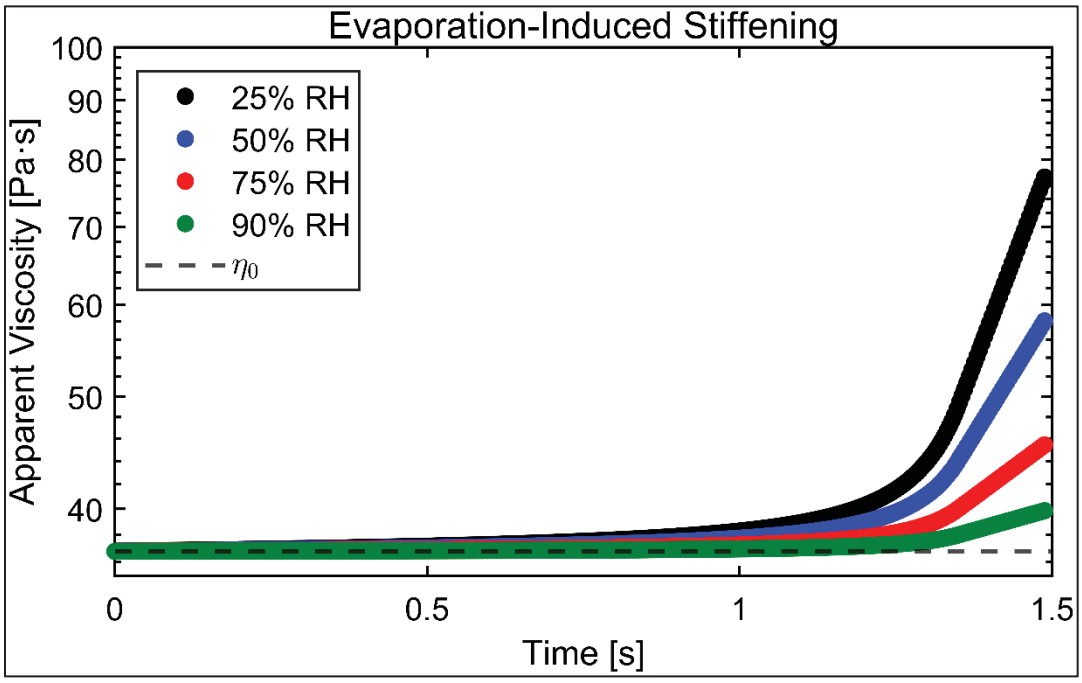

Figure 5.7 Evolution of the apparent extensional viscosity during filament thinning, computed from the modeled radial concentration profiles under ambient solvent vapor pressures of 25%, 50%, 75%, and 90%; the bulk viscosity was calculated as a cross-sectional weighted average; time reflects the experimentally measured filament radius evolution $R(t)$ (Figure 5.2); dashed lines indicate the initial viscosity of the solution before thinning

These modeled rheological behaviors are consistent with experimental CaBER measurements, where relaxation time increased significantly under low vapor pressure conditions, indicating enhanced elastic resistance due to evaporation-induced solidification. This behavior also aligns with the electrospinning results presented in Figure 5.1: thicker fibers were obtained at low ambient vapor pressure (25%), corresponding to more rapid solvent loss and earlier jet solidification. As vapor pressure increased, fiber diameters decreased, reflecting delayed solidification and reduced elastic resistance. At 90%, insufficient evaporation led to the collapse of the jet into a film, in agreement with the nearly constant viscosity and short relaxation times observed. The convergence of trends in electrospinning, CaBER

measurements, and theoretical modeling underscores the critical role of solvent evaporation in governing both the extensional rheology captured by capillary breakup experiments under unsaturated ambient conditions and the final morphology of electrospun fibers.

5.4 Conclusion

This study investigated the influence of solvent evaporation on extensional flow behavior and fiber formation by integrating electrospinning, Capillary Breakup Extensional Rheometry (CaBER), and numerical modeling under controlled solvent vapor pressure environments ranging from 25% to 90%.

Experimentally, an aqueous 22 wt% pullulan solution was employed as a representative system for experimental investigations. Under low vapor pressure (25%), electrospinning produced significantly larger diameter fibers. Upon increase of vapor pressure, the diameter decreases, but fiber formation was entirely suppressed at high vapor pressure (90%). Correspondingly, CaBER measurements showed markedly longer relaxation times at low vapor pressure, indicating increased resistance to filament thinning. These findings consistently point to a shared sensitivity of both processes to solvent evaporation.

To better understand this behavior, a model was developed to simulate solvent evaporation at the filament's surface and radial diffusion within it. Experimental filament radius data from CaBER was used to define the time-dependent geometry. Based on the modeled concentration profiles across the filament, the local viscosity at each radial position was computed using an experimentally established concentration-dependent relationship. These values were then averaged using a weighted scheme across the cross-section to obtain the apparent (bulk) extensional viscosity at each time step. The results showed a progressive increase in apparent viscosity during filament thinning, particularly under low vapor pressure conditions (25%) where solvent loss is significant. In contrast, at high vapor pressure (90%), the polymer concentration, and thus the viscosity, remained nearly unchanged, indicating negligible impact from evaporation.

The agreement between experimental and modeled trends demonstrates that CaBER measurements are highly sensitive to solvent evaporation. In particular, part of the observed strain hardening, reflected by the relaxation time, can be attributed not solely to inherent material properties, but to solvent loss during filament thinning. This evaporation leads to increases in polymer concentration, which amplify the apparent viscosity of the filament over time. At high ambient vapor pressure, this effect is largely suppressed, resulting in minimal change in both solution concentration and its apparent viscosity.

These results carry important implications for researchers using capillary breakup measuring tools or similar open-air techniques: ambient vapor pressure must be controlled and reported, as even moderate evaporation can alter rheological interpretations. For polymer systems processed by electrospinning, these findings reaffirm the critical role of evaporation in defining jet solidification and final fiber morphology.

Altogether, this work establishes CaBER as a processing-relevant rheological tool, but also highlights the need for experimental caution. Without appropriate environmental control or evaporation-aware modeling, the measured extensional properties may reflect not only intrinsic material behavior but also evaporation-induced artifacts. Accurately capturing and interpreting the flow behavior of volatile polymer solutions therefore requires both experimental control and theoretical insight.

CHAPTER 6

TUNING POLYMER SOLUTION ELASTICITY FOR ELECTROSPINNING: EFFECTS OF MOLECULAR WEIGHT DISTRIBUTION AND ELASTIC DOPING

Étienne J. Beaudoin[a], Ricardo J. Zednik[a] and Nicole R. Demarquette[a],

[a]Department of Mechanical Engineering, École de Technologie Supérieure,
1100 Notre-Dame West, Montreal, Quebec, Canada H3C 1K3

Paper submitted for publication, August 2025

6.1 Introduction

This chapter is based on the work submitted for publication in August 2025 in *Rheologica Acta* and addresses the third component (A3) of the first research objective of this thesis: to assess the influence of polymer formulation on extensional rheology and electrospinnability, and to demonstrate elastic doping as a practical tool for scale-up. Electrospinning requires sufficient extensional elasticity to stabilize the liquid jet against capillary breakup, a property conferred primarily by entangled high–molecular-weight chains.

In this chapter, the roles of molecular weight distribution (MWD), matrix viscosity, and long-chain content are systematically investigated using blends of poly(ethylene glycol) (PEG) and poly(ethylene oxide) (PEO). Comparisons between low–molecular-weight PEG and entangled high–molecular-weight PEO highlight the critical importance of chain entanglements for fiber formation. Controlled broadening of MWD at constant average molecular weight is shown to increase relaxation times measured by CaBER and produce fibers with larger diameters, highlighting the disproportionate contribution of long polymer chains. Experiments with Boger-type fluids demonstrate that shear viscosity alone does not correlate with electrospinning performance, while CaBER relaxation times remain predictive. Increasing the background matrix viscosity further enhances extensional elasticity by slowing chain relaxation and filament thinning. Finally, elastic doping, done by adding a trace amount of

long-chain PEO to an unspinnable short chains PEG matrix, enabled fiber formation and produced a fivefold increase in polymer throughput.

Together, these results establish extensional relaxation time as a robust predictor of electrospinnability and show that tuning molecular weight distribution and long-chain content offers a versatile strategy for designing high-yield nanofiber formulations.

6.2 Results and Discussion

6.2.1 Highlighting the Need for Polymer Long Chains

To establish a baseline for interpreting fiber formation and extensional elasticity, three single-polymer solutions were examined: one PEG solution, and two PEO solutions of different molecular weights. Their compositions, along with their steady shear viscosity and CaBER relaxation times, are presented in Table 6.1. The relaxation times were obtained using plates with a diameter of 4 mm and an initial gap of 2 mm. Five displacement amplitudes were applied (4.5, 5.0, 5.5, 6.0, and 6.5 mm), corresponding to final plate separations between 6.5 and 8.5 mm. Reported values represent the average of these measurements.

The PEG solution exhibited Newtonian behavior in both shear and extensional flows, showing no dependence of viscosity on shear rate and no measurable extensional relaxation in the CaBER test. In contrast, both PEO solutions showed clear shear thinning behavior, and measurable caber relaxation times increasing with molecular weight (see APPENDIX V, Figure-A V-1 and Figure-A V-2).

Electrospinning results, presented in Figure 6.1, reflect these trends. The PEG solution produced only particles, while both PEO solutions yielded uniform nanofibers. Notably, the higher-molecular-weight PEO formed thicker fibers than its lower-molecular-weight counterpart, consistent with its longer relaxation time. These outcomes reinforce the conclusion that shear viscosity alone does not predict electrospinnability, and that the fluid’s

elastic response under extension, modulated by chain length, is the dominant factor governing fiber formation.

Table 6.1 Compositions and rheological properties of baseline pure PEG and PEO solutions

Polymer	**Molecular Weight** $[g/mol]$	**Concentration**	**Zero Shear viscosity [mPa*s]**	**CaBER Relaxation time [ms]**
PEG	35,000	40%	3,035	-
PEO	300,000	6%	2,226	14 ± 1.6
PEO	900,000	6%	23,719	124 ± 4.0

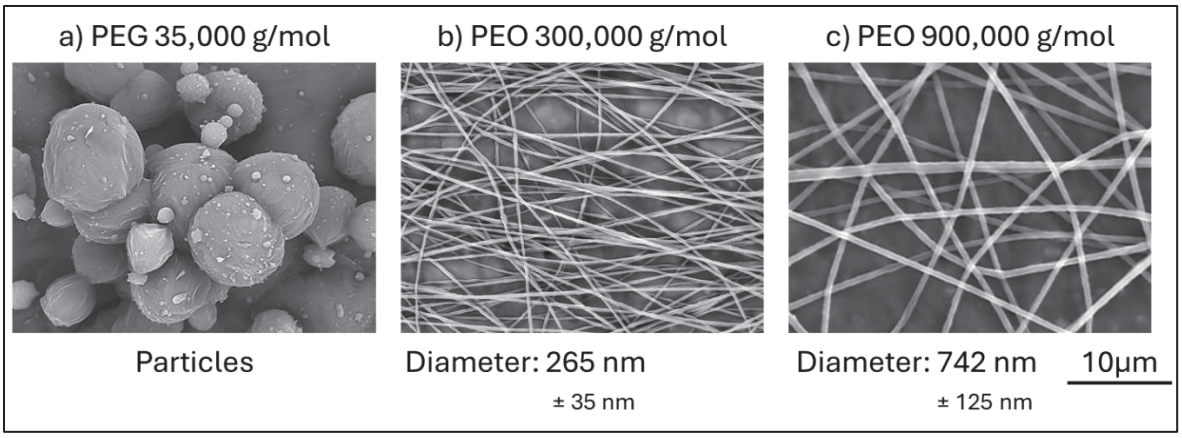

Figure 6.1 Electrospinning outcomes of PEG 35,000 g/mol, 40 wt% a) PEO 300,000 g/mol, 6 wt% b) and PEO 900,000 g/mol, 6 wt% c) solutions; despite its high solid content, the PEG solution fails to produce fibers, while the PEO solutions yield uniform nanofibers, highlighting the importance of extensional elasticity rather than shear viscosity alone in enabling fiber formation; the higher molecular weight PEO in c) produces fibers with bigger diameters than the lower molecular weight counterpart in b), consistent with its longer relaxation time; solutions were processed at a flow rate of 1 mL/h, with the applied voltage adjusted to stabilize the Taylor cone; the needle-to-collector distance was 20 cm for the PEG solution and increased to 60 cm for the PEO formulations to allow sufficient drying before fiber deposition

6.2.2 Impact of Molecular Weight Distribution on Solution's Elasticity and Fiber Formation

Building on the previous comparison of short and long chain formulations, where the presence of longer polymer chains was shown to significantly increase extensional elasticity and enable fiber formation, the present investigation examined whether these effects could be modulated by altering the molecular weight distribution (MWD) while maintaining a constant average molecular weight. Broadening the MWD effectively increases the fraction of long chains in the system, enhancing the elastic contributions without requiring a higher nominal molecular weight polymer. To explore this effect, four mixtures were prepared by blending PEG and PEO samples of distinct molecular weights, while keeping the total polymer concentration constant across all formulations, as detailed in Table 6.2. Each mixture was formulated to maintain a comparable average molecular weight while systematically broadening the molecular weight distribution.

Table 6.2 Compositions of PEO and PEG mixtures with controlled molecular weight distribution (MWD); each mixture was formulated to maintain a comparable average molecular weight (300,000 g/mol) while systematically increasing MWD by blending polymers of distinct molecular weights, at a total polymer concentration of 6 wt%; the table lists the weight concentration (%) of each component in the mixtures

Mixture	**35,000 g/mol [wt%]**	**100,000 g/mol [wt%]**	**300,000 g/mol [wt%]**	**600,000 g/mol [wt%]**	**4M g/mol [wt%]**	**Zero Shear η [mPa*s]**	**Caber λ [ms]**
Mix 1	-	-	6	-	-	2114	14 ± 1.6
Mix 2	-	1.8	3	1.2	-	1406	104 ± 6.3
Mix 3	1.86	1.26	1.98	0.78	0.12	616	126 ± 4.2
Mix 4	5.6	-	-	-	0.4	95	172 ± 6.1

The steady shear rheology of the four mixtures is presented in Figure 6.2, and the zero-shear viscosity is also indicated in Table 6.2. Two clear trends can be observed. First, the zero-shear viscosity, highlighted by dashed lines, decreases progressively as the MWD increases. Second,

the onset of shear thinning shifts toward lower shear rates in mixtures with broader molecular weight distributions. This behavior reflects the broader spectrum of relaxation times associated with an increased diversity of chain lengths, which results in an earlier departure from Newtonian behavior as the deformation rate increases. These observations are consistent with previous studies of polymer solutions and melts reporting similar sensitivity of shear rheology to the distribution of molecular weights (Herbert Leaderman; Robert G. Smith; L. C. Williams, 1959; John M. Dealy, 1990; Minoshima, White, & Spruiell, 1980; Rudd, 1960; Ye & Sridhar, 2005).

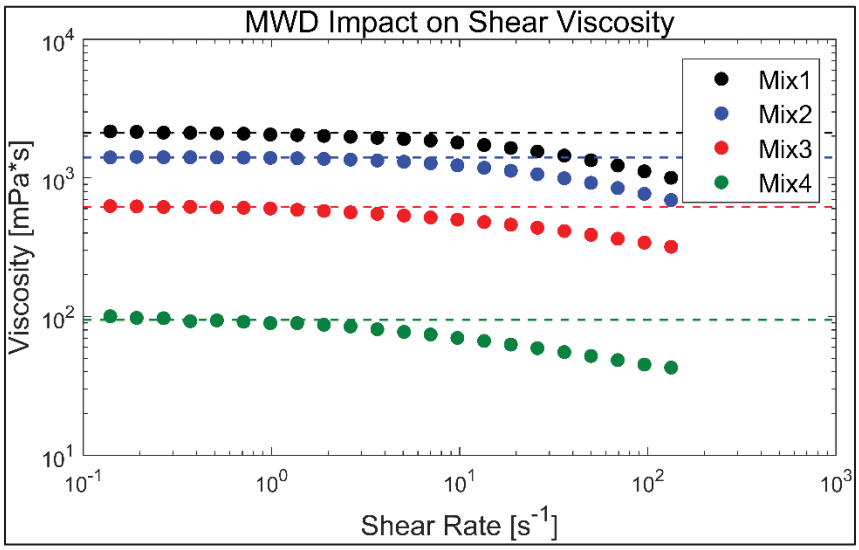

Figure 6.2 Shear viscosity of Mix1 to Mix4 as a function of shear rate; dashed lines indicate the estimated zero-shear viscosity for each sample, calculated as the average of viscosity values measured between 0.1 and 1 s^{-1}; the zero-shear viscosity decreases progressively from Mix1 to Mix4 as the MWD increases; furthermore, the onset of shear thinning shifts to lower shear rates, consistent with a broadened relaxation time spectrum contributed by high-molecular-weight chains

The four solutions were also characterized by CaBER (see APPENDIX V, Figure-A V-3), and the extracted relaxation times are presented in Table 6.2. A clear trend is observed: as the molecular weight distribution broadens, the relaxation time increases significantly, despite the nearly constant average molecular weight. These results indicate that even a small fraction of high molecular weight chains can dominate the extensional elasticity of the fluid. This behavior reflects the strong molecular-weight dependence of relaxation dynamics, with the longest

chains storing elastic stresses and resisting filament thinning over extended timescales during extensional flow (Calabrese et al., 2025; C. Clasen et al., 2006; Plog et al., 2005).

Electrospinning outcomes for Mix1 to Mix4 are presented in Figure 6.3. The average fiber diameter and standard deviation are reported for each formulation. Consistent with the CaBER results, increasing MWD leads to progressively larger fiber diameters, reflecting the higher extensional elasticity of these mixtures. This trend underscores the strong correlation between extensional relaxation time and fiber morphology and further supports the conclusion that elastic contributions, rather than shear viscosity alone, are the principal factor governing electrospinnability in these systems. More broadly, this finding highlight that tailoring the molecular weight distribution provides a practical strategy to control fiber dimensions and optimize processability without necessarily increasing the nominal molecular weight or concentration.

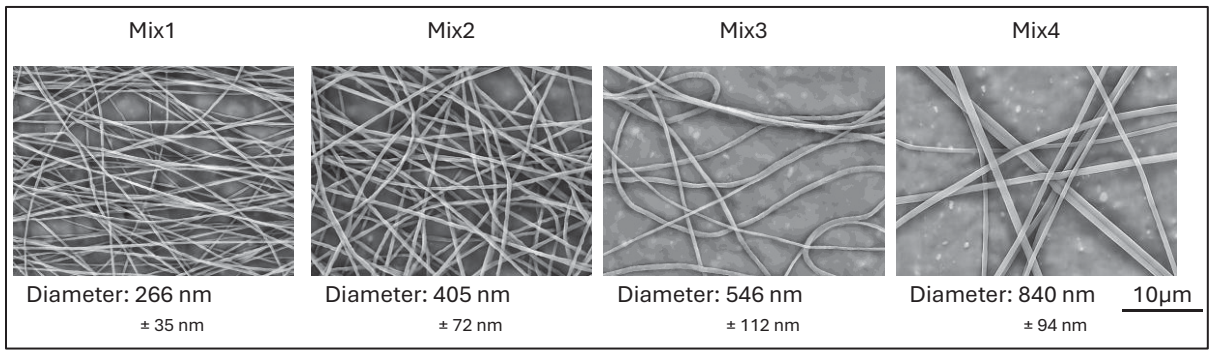

Figure 6.3 Electrospun fiber morphology of Mix 1 to Mix 4; average fiber diameter and standard deviation are indicated; as molecular weight distribution (MWD) increases across the series, fiber diameter also increases; electrospinning was performed at 1 mL/h with a 20 cm working distance and voltage adjusted to stabilize the Taylor cone

Overall, these findings confirm that even at constant average molecular weight, broadening the molecular weight distribution has a pronounced effect on the rheological and processing behavior of the solutions. Across the four blends, increasing MWD led to progressively lower zero-shear viscosity and an earlier onset of shear thinning, indicative of more pronounced non-Newtonian behavior. This was further reflected in CaBER experiments, where broader distributions yielded longer relaxation times, consistent with the disproportionate influence of longer chains on extensional elasticity. Finally, electrospinning outcomes showed that

mixtures with broader MWD produced thicker fibers, highlighting the practical implications of these rheological changes. Together, these results demonstrate that processing-relevant rheological behavior cannot be inferred solely from average molecular weight or shear viscosity, but instead requires consideration of the complete molecular weight distribution and its impact on the relaxation spectrum, which in turn strongly influences extensional flow behavior.

6.2.3 Boger Fluid's

Building on the observation that the proportion of long chains strongly influences extensional rheology and electrospinnability, the next set of experiments focused on mixtures designed to decouple viscosity and elasticity more systematically. In the previous section, Mix 4 already represented a form of bimodal distribution, combining a large fraction of low-molecular-weight chains with a smaller proportion of longer chains. Such formulations are commonly referred to as Boger fluids, which are often used to independently tune viscosity and elasticity. In these systems, the short chains contribute primarily to viscous friction without forming significant entanglements, while the small amount of long chains establishes an elastic network to which extensional deformation is particularly sensitive. Because the fraction of long chains is low in these Boger fluids, their contribution to shear viscosity is largely negligible and is overwhelmed by the high fraction of the short-chain component. Here, PEG ($\sim 35{,}000\ g/mol$) was employed as the short-chain additive due to its lack of measurable entanglement (as demonstrated previously), and high-molecular-weight PEO ($\sim 900{,}000\ g/mol$) was used to provide the entangled fraction. Although entanglements are expected for the high-molecular-weight PEO solutions used here, defining entanglement thresholds solely from shear-based criteria can be misleading for extensional flows, where even partially overlapped chains may sustain elastic stress (Clasen et al., 2006). The following sections first examine Boger fluids prepared with constant PEG concentration, resulting in similar shear viscosity, while varying the PEO content to systematically adjust the level of elasticity measured in extensional flow. The next series keeps the PEO content constant while varying the PEG concentration, which unexpectedly revealed that extensional relaxation times still changed substantially. This

observation suggests that the background viscosity contributed by short chains influences how the long-chain network relaxes under extensional flow. However, PEG in water does not act as a perfectly ideal continuum solvent for PEO, so the relaxation time does not scale strictly proportional to the background viscosity. Nevertheless, the observed trend remains consistent with increased friction contributed by the short chains. To investigate this phenomenon more directly, a final set of mixtures was prepared by jointly adjusting PEG and PEO concentrations to achieve comparable extensional relaxation times. This design enabled a direct assessment of the extent to which the resulting elongational elasticity, shaped by the combination of long-chain entanglement and background viscosity, governs fiber formation during electrospinning.

6.2.3.1 Constant Short Chains Content

To further investigate the relative contribution of long-chain entanglement on the rheological behavior and electrospinnability of polymer solutions, a series of Boger fluids was prepared by maintaining a constant concentration of low-molecular-weight PEG while systematically varying the amount of high-molecular-weight PEO. The compositions of these mixtures, along with their steady shear viscosity and CaBER relaxation times, are reported in Table 6.3.

Table 6.3 Compositions and rheological properties of Boger-fluids with constant PEG content and varying PEO content

Bo#	**wt% of PEG 35,000 g/mol**	**wt% of PEO 900,000 g/mol**	**Zero Shear η [mPa*s]**	**Caber λ [ms]**
1	25	0.05	427	38 ± 1.9
2	25	0.1	401	47 ± 4.0
3	25	0.16	470	59 ± 4.4

Despite increasing the proportion of long chains, the steady shear viscosity remained nearly constant across all three formulations. This confirms that the low-molecular-weight PEG dominates the viscous response under shear, and that the small quantities of entangled PEO

contribute minimally to the resistance in steady flow. All samples displayed nearly Newtonian behavior over the measured shear rate range (APPENDIX V, Figure-A V-4).

In contrast, the extensional relaxation time measured by CaBER increased markedly with rising PEO content, indicating a growing resistance to filament thinning due to elastic effects (APPENDIX V, Figure-A V-5). This pronounced sensitivity to even small fractions of long chains highlights the effectiveness of extensional rheology in detecting polymer elasticity that remains hidden in shear measurements.

Electrospinning results for these three Boger fluids, shown in Figure 6.4, further reinforce this distinction. Boger fluid #1, with the lowest relaxation time, produced fibers with numerous beads and droplets. Boger fluid #2 yielded thicker, more continuous fibers with fewer defects. Boger fluid #3, which had the highest relaxation time, formed smooth, uniform nanofibers. Despite their similar shear viscosities, the dramatic difference in electrospinning performance correlates closely with the relaxation time, underscoring the importance of extensional elasticity for jet stability and fiber formation.

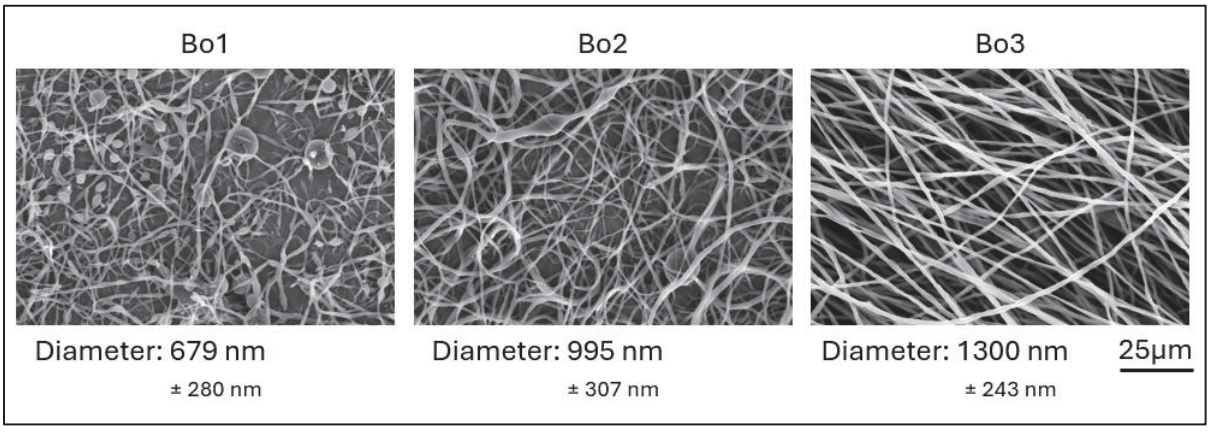

Figure 6.4 Electrospinning outcomes of Boger-fluids #1 to #3, showing that fiber morphology correlates with extensional relaxation time measured in CaBER; boger-fluid #1 produces only beads, while #2 yields partial fibers and #3 produces uniform fibers, despite similar shear viscosity across all samples; electrospinning conditions were identical for all samples

6.2.3.2 Constant Long Chains Content

To evaluate the influence of matrix viscosity on the rheological behavior and electrospinnability of polymer solutions, a second series of Boger fluids was formulated by maintaining a constant concentration of high molecular weight PEO while systematically varying the amount of low molecular weight PEG. The compositions of these mixtures, along with their steady shear viscosity and CaBER relaxation times, are presented in Table 6.4.

Table 6.4 Compositions and rheological properties of Boger-fluids with constant PEO content and varying PEG content

Bo#	wt% of PEG 35,000 g/mol	Wt% of PEO 900,000 g/mol	Zero Shear η [mPa*s]	Caber λ [ms]
4	20	0.1	177	32 ± 3.0
5	25	0.1	401	47 ± 4.0
6	30	0.1	834	53 ± 7.3

As PEG content increased, the zero-shear viscosity rose accordingly, while all samples maintained nearly Newtonian behavior over the measured shear rate range (APPENDIX V, Figure-A V-6). These results align with the previous series, confirming that PEG dominates the steady shear response due to its much larger concentration, which overwhelms the contribution of the small fraction of long PEO chains.

Interestingly, extensional rheology measured by CaBER revealed a perhaps non-intuitive trend: increasing PEG concentration resulted in progressively longer relaxation times, despite a constant amount of entangled PEO in all formulations (APPENDIX V, Figure-A V-7). Since PEG tested independently exhibits no measurable elasticity, this effect cannot be attributed to the short chains themselves. Rather, it suggests that increasing the background viscosity enhances the drag on the long-chain network, thereby slowing its relaxation. This observation underscores the fact that matrix viscosity can modulate the apparent elastic response of the fluid, reflected by its relaxation time, by influencing the dynamics of entangled polymers during filament thinning.

The electrospinning performance of Boger fluids #4 to #6, shown in Figure 6.5, closely reflects the relaxation time trend. Boger fluid #4 produced thin fibers with numerous beads and droplets, whereas Boger fluid #5 formed thicker, more continuous fibers with fewer defects. Boger fluid #6 yielded fibers with the largest diameters and the lowest observed defect density among the series. These results demonstrate that even when the long chain content is fixed, enhancing matrix viscosity can improve fiber formation by increasing the apparent elastic response during uniaxial extension.

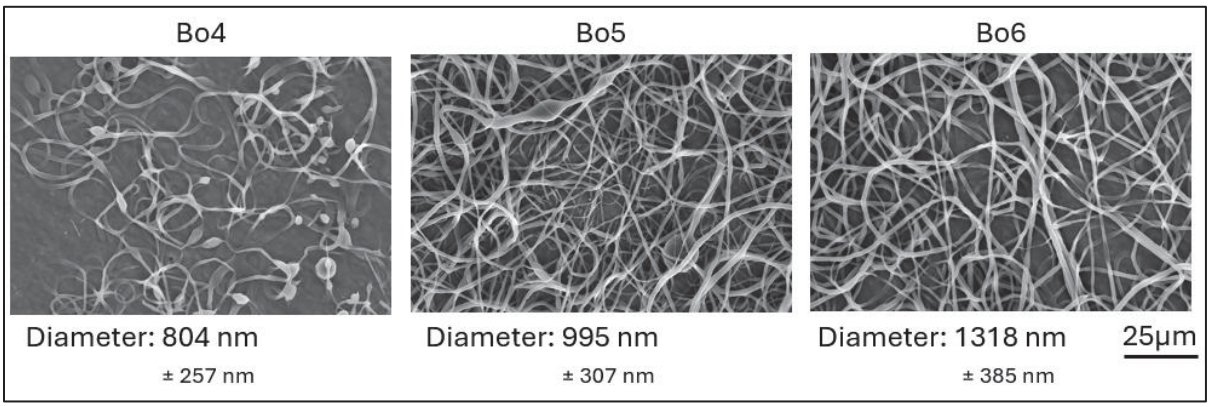

Figure 6.5 Electrospinning outcomes of Boger-fluids #4 to #6, demonstrating that increasing PEG concentration results in progressively larger fibers, consistent with the trend in extensional relaxation times; in all samples, PEO content was held constant, confirming that the increase in fiber diameter arises from the influence of background viscosity; electrospinning conditions were identical for all samples

6.2.3.3 Constant Relaxation Time

To demonstrate more explicitly that extensional relaxation time is the most reliable predictor of electrospinnability, a final series of Boger fluids was formulated by jointly adjusting the concentrations of high molecular weight PEO and low molecular weight PEG to achieve comparable relaxation times while varying the shear viscosity. The compositions of these mixtures, along with their steady shear viscosity and CaBER relaxation times, are presented in Table 6.5. In this set, increasing PEG content allowed a corresponding reduction in PEO content while maintaining comparable extensional relaxation times.

Table 6.5 Compositions and rheological properties of Boger-fluids designed to achieve comparable extensional relaxation times with increasing background viscosity

Bo#	wt% of PEG 35,000 g/mol	Wt% of PEO 900,000 g/mol	Zero Shear η [mPa*s]	Caber λ [ms]
7	25	0.1	401	47 ± 4.0
8	30	0.08	705	49 ± 6.6
9	33	0.06	1210	45 ± 11.0

As PEG concentration increased and PEO content decreased, the zero-shear viscosity of the mixtures increased accordingly, confirming once again that PEG dominates the steady shear response. All samples remained essentially Newtonian over the measured range (APPENDIX V, Figure-A V-8)

Despite these differences in composition and shear viscosity, CaBER measurements confirmed that the extensional relaxation times of all three samples were closely matched (APPENDIX V, Figure-A V-9). The filament thinning dynamics converged onto similar exponential decay regimes, indicating that increased matrix viscosity can compensate for reduced entangled chain content by slowing the relaxation of the long chain network. This demonstrates that similar relaxation times, and thus comparable extensional responses, can be achieved through different combinations of PEG and PEO.

Electrospinning results, presented in Figure 6.6, reflect this convergence. All three formulations produced fibers of similar morphology, diameter, and defect density. These results reinforce the conclusion that extensional relaxation time, rather than shear viscosity or total polymer content, is the most reliable predictor of electrospinnability. Moreover, they illustrate how tuning the matrix viscosity provides a practical strategy for controlling fiber formation while reducing the amount of long chains required.

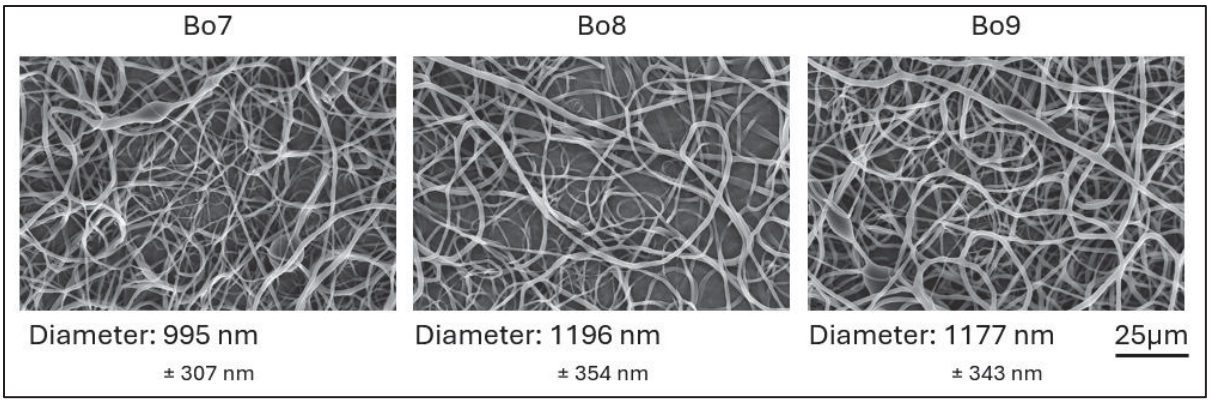

Figure 6.6 Electrospinning outcomes of Boger-fluids #7 to #9, showing that once again, fiber morphology correlates with the extensional relaxation time measured by CaBER rather than the initial viscous response; all three formulations produce similar fibers despite varying PEO concentrations, underscoring that extensional elasticity, rather than shear viscosity, is the primary predictor of electrospinnability; electrospinning conditions were identical for all samples

6.2.4 Elastic Doping for High-Yield Fiber Production

To demonstrate the practical importance of solution optimization in electrospinning, two polymer formulations with contrasting compositions were compared. The first was a conventional solution of high–molecular-weight PEO ($\sim 900{,}000\ g/mol$) at 6 wt%, while the second was a Boger-type fluid comprising a concentrated blend of PEG ($\sim 35{,}000\ g/mol$) and a small amount of the same high–molecular-weight PEO. This blend had a total solid content of approximately 30 wt%. The compositions of these two mixtures, along with their steady shear viscosity and CaBER-measured extensional relaxation times, are presented in Table 6.6. Full rheological characterization, including shear and CaBER data, is provided in the Supplementary Information (APPENDIX V, Figure-A V-10 and Figure-A V-11).

Table 6.6 Composition and rheological properties of PEO and elastically doped PEG formulations

Type	wt% of PEG 35,000 g/mol	Wt% of PEO 900,000 g/mol	Zero Shear η [mPa*s]	Caber λ [ms]
Simple PEO	0	6	23,719	124 ± 4.0
PEG-PEO Blend	30	0.05	885	37 ± 4.2

Both solutions were electrospun at a constant volumetric flow rate of 1 mL/h. However, the dilute PEO solution required significantly more time for solvent evaporation, necessitating an increase in the needle-to-collector distance to 60 cm, compared to the standard 20 cm used for other formulations in this study. As shown in Figure 6.7, despite these differences in formulation, both solutions successfully produced nanofibers with comparable diameter and morphology.

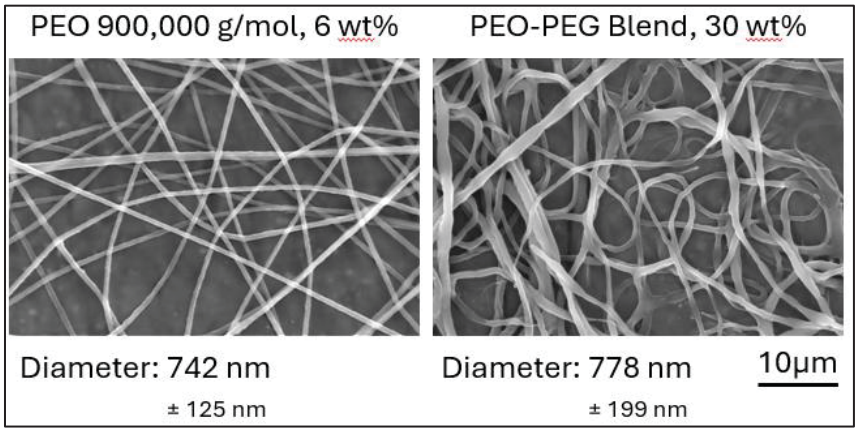

Figure 6.7 Electrospinning outcomes of 6 wt% PEO and 30 wt% PEG + 0.05 wt% PEO (elastically doped) solutions; despite differences in formulation, extensional rheology, and required working distance (60 cm for PEO, 20 cm for the PEG-based blend), both solutions produced nanofibers with comparable diameter and morphology; electrospinning was performed at a constant flow rate of 1 mL/h, with voltage adjusted to stabilize the Taylor cone; the higher solid content of the PEG-based formulation enabled an approximately fivefold increase in polymer throughput relative to the PEO-only solution

In contrast to other formulation comparisons presented in this work, the two solutions discussed here differ substantially in polymer concentration. The high solvent content of the PEO-only solution led to slower jet solidification, requiring a greater working distance and a

slower deformation rate to enable fiber formation. This solution exhibited a higher extensional relaxation time measured by CaBER, indicating a slower thinning rate during electrospinning process, which facilitated sufficient solvent evaporation accounting for the longer drying kinetics. Two key conclusions emerge from this comparison:

1. Although both solutions yielded similar fiber morphologies, the PEG–PEO blend enabled a fivefold increase in polymer mass throughput, owing to its higher solid fraction at the same flow rate. This highlights the potential of formulation tuning to scale-up the electrospinning process.
2. Fibers were successfully produced from a predominantly PEG-based solution, a polymer that does not form fibers when electrospun alone, even at high concentrations. Fiber formation was enabled by incorporating only a trace amount of high–molecular-weight PEO, just one part in 600 relative to the PEG content, demonstrating the effectiveness of elastic doping in rendering otherwise unspinnable systems electrospinnable.

These findings underscore that extensional rheology, though essential for predicting electrospinnability, does not act in isolation and must be evaluated in the context of other process parameters, notably solvent evaporation dynamics. They also highlight the importance of selecting an appropriate molecular weight and molecular weight distribution, as these parameters fundamentally govern the extensional rheology of the solution and, consequently, the formation and scalability of electrospun fibers. Elastic doping, when judiciously applied, offers a powerful strategy for enhancing both the processability and scalability of electrospinning systems.

6.3 Conclusion

This work investigated the impact of long-chain content and molecular weight distribution (MWD) on the extensional rheology and electrospinning behavior of polymer solutions, using

a series of formulations prepared with polyethylene glycol (PEG) and polyethylene oxide (PEO). The findings provide several important insights:

First, the comparison between short-chain PEG and long-chain PEO demonstrated that even highly viscous PEG solutions fail to form continuous fibers, whereas lower-viscosity PEO solutions produce uniform nanofibers. This highlights that long-chain are essential to generate the elastic stresses required to stabilize the jet against capillary breakup during electrospinning.

Second, experiments varying MWD while maintaining constant weight-average molecular weight revealed that broader distributions substantially increased the extensional relaxation time measurable by CaBER and yielded fibers with larger diameters, despite a lower zero-shear viscosity. In parallel, the onset of shear thinning shifted to lower shear rates, reflecting the broader relaxation time spectrum contributed by the long chains. Together, these observations underscore that even a small fraction of high molecular weight chains exerts a disproportionate influence on the fluid's elastic response, with extensional flows particularly sensitive to their presence.

Third, experiments with Boger fluids, which are designed to decouple viscosity and elasticity, confirmed that the quantity of long chains in a polymer solution primarily governs extensional rheology and, consequently, fiber morphology. When the concentration of high molecular weight PEO was increased at constant PEG content, the relaxation time and resulting fiber diameter increased substantially, even though shear viscosity remained nearly unchanged. Conversely, at constant PEO content, increasing the PEG concentration raised the shear viscosity and also led to longer CaBER's relaxation times and larger fibers. Finally, a third set of formulations demonstrated that comparable relaxation times, and thus similar fiber morphologies, could be achieved by jointly tuning the amount of long and short chains, underscoring that background viscosity modulates the relaxation dynamics of entangled long chains. These results highlight the need to consider both long chain content and matrix viscosity in parallel when designing electrospinnable formulations with targeted extensional properties.

Finally, elastic doping with a trace amount of high molecular weight PEO enabled fiber formation from an otherwise unspinnable low molecular weight PEG solution. This approach yielded fibers with morphology comparable to those from a dilute PEO formulation, while enabling a fivefold increase in polymer throughput.

Altogether, these results confirm that the extensional relaxation time measured by CaBER is a robust and process-relevant predictor of fiber formation, more so than shear viscosity alone. The ability to tailor solution properties by independently controlling the amount of long chains and the matrix viscosity offers a versatile strategy for optimizing electrospinning performance, scaling production, and designing fibers from low molecular weight polymers traditionally considered unspinnable.

CHAPTER 7

SCALED-UP MULTI-NEEDLE ELECTROSPINNING PROCESS USING PARALLEL PLATE AUXILIARY ELECTRODES

Étienne J. Beaudoin[a], Maurício M. Kubaski[a], Mazen Samara[a], Ricardo J. Zednik[a] and Nicole R. Demarquette[a],

[a]Department of Mechanical Engineering, École de Technologie Supérieure, 1100 Notre-Dame West, Montreal, Quebec, Canada H3C 1K3

Paper published in *Nanomaterials*, April 2022
DOI: https://doi.org/10.3390/nano12081356

7.1 Introduction

This chapter is based on the work published in Nanomaterials (Beaudoin, Kubaski, Samara, Zednik, & Demarquette, 2022) and addresses the first step (B1) of the second research objective of this thesis: to mitigate electric field non-uniformities in multi-needle systems in order to reduce jet interference and stabilize fiber production. Electrospinning has long been recognized as a powerful method to produce high-quality polymeric nanofibers, but the extremely low productivity of single-needle systems, typically 0.01–2 g/h, limits its translation from laboratory studies to industrial applications. Although needleless electrospinning has been proposed as a higher-throughput alternative, it suffers from drawbacks such as broad fiber diameter distributions, premature solvent evaporation from the free surface solution, and incapacity to produce complex architectures such as core–shell fibers. Multi-needle electrospinning therefore remains an attractive strategy, since it can in principle combine the versatility of single-needle setups with substantially higher yields. However, non-uniform electric field distributions along the array lead to jet deflection, heterogeneous fiber diameters, and variable membrane thickness, posing a major barrier to practical implementation.

In this chapter, a linear twenty-needle array is studied, and the introduction of parallel-plate auxiliary electrodes is proposed as a solution to homogenize the electric field. Through combined experiments and finite element simulations, this approach is shown to stabilize jet

trajectories, reduce fiber diameter variability, and enable the scalable fabrication of high-quality nonwoven nanofiber membranes.

7.2 Methodology

A linear array of twenty needles, positioned 13 mm apart, was used to process the PVDF solution. The solution flowrate through each needle was 0.5 mL/h. The applied voltage to the needles was +15 kV and the needles were placed at 20 cm from the collector to which -15kV was applied. A simple flat collector and a conveyor belt collector, with travel speed of 0.5 mm/s, were used. A micrometer was used to measure the thickness of the membranes, the average of 5 measurements is reported, and the standard deviation is represented as the error bars.

The electric field distribution just below the needles was modeled using COMSOL Multiphysics 5.6. To do so, both Gauss' and Faraday's Laws (Equations (7.1) and (7.2)) were solved using the electrostatic stationary physics interface. In these equations, $\mathbb{D}$ is the electric displacement field, ρ_{v} is the volumetric charge density, E is the electric field, and V is the electric potential. The minimum and maximum free tetrahedral element size was 0.003 and 1 mm, respectively. In the simulation, stainless steel chromium steel, from the COMSOL library, was used as the material for the needles, air for the space domain, and pure aluminum for the collector.

$$\nabla \cdot \mathbf{D} = \rho_{\mathrm{v}} \tag{7.1}$$

$$\mathbf{E} = -\nabla V \tag{7.2}$$

7.3 Experimental Results

A representative in situ image showing the multi-needle electrospinning apparatus is shown in Figure 7.1. All 20 needles making up the linear array were used simultaneously in parallel during fiber production.

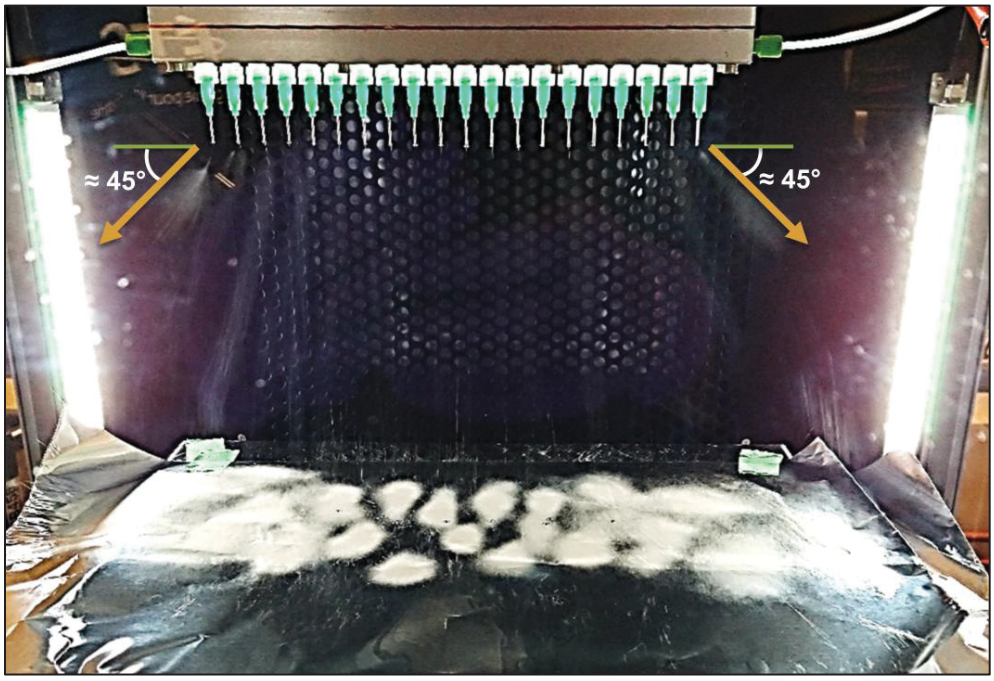

Figure 7.1 Multi-needle electrospinning, initial setup (without auxiliary electrodes)

As indicated by the orange arrows in Figure 7.1, the spun jets from the side needles were deflected by around 45° from the vertical. The consequence of this deflection can be seen in the deposition pattern of the spun fibers, as presented in Figure 7.2.

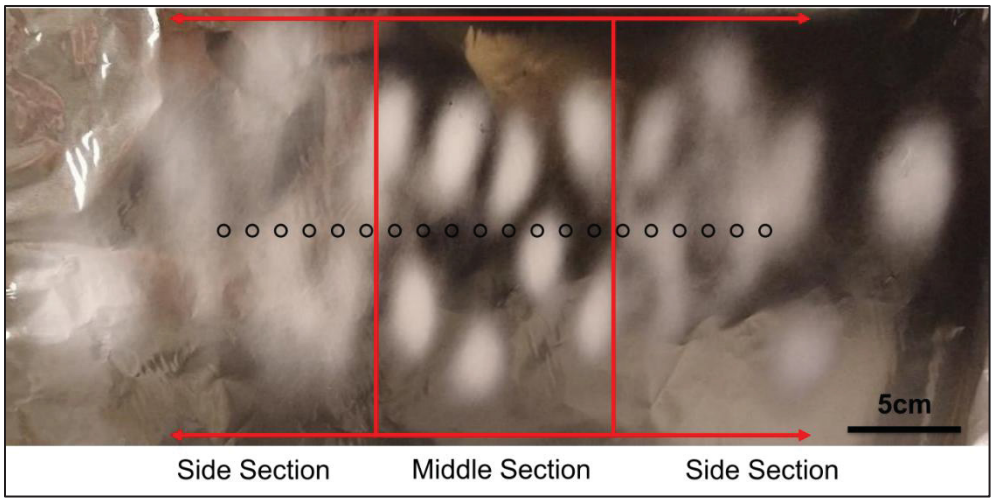

Figure 7.2 Deposition pattern of the initial setup (without auxiliary electrodes); the black circles represent needle position

The deposition pattern shows a well-defined middle section, where the deposition spots are uniform in size and density, and two distinct side sections, where the deposition spots are spread over a wider area, which decreases the deposition density of the fibers.

The resulting fibers were analyzed by SEM and representative images of the fibers are shown in Figure 7.3. It can be observed that the fibers in the middle section have a significantly larger diameter than those in the side sections, an average of 445 nm and 288 nm, respectively.

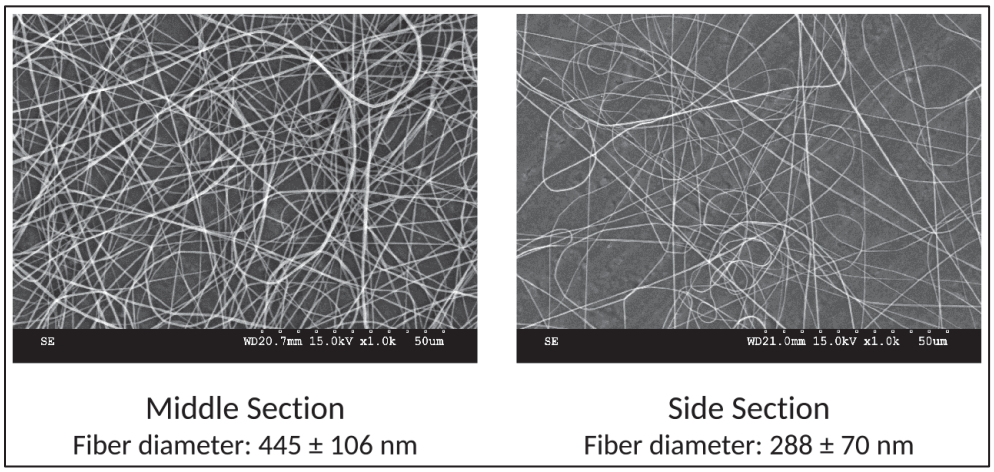

Figure 7.3 Example of the fibers from the middle and the side sections with initial setup (without auxiliary electrodes)

Using a conveyor belt as a collector, large membranes were produced, and the thickness was measured along the width, as presented in Figure 7.4.

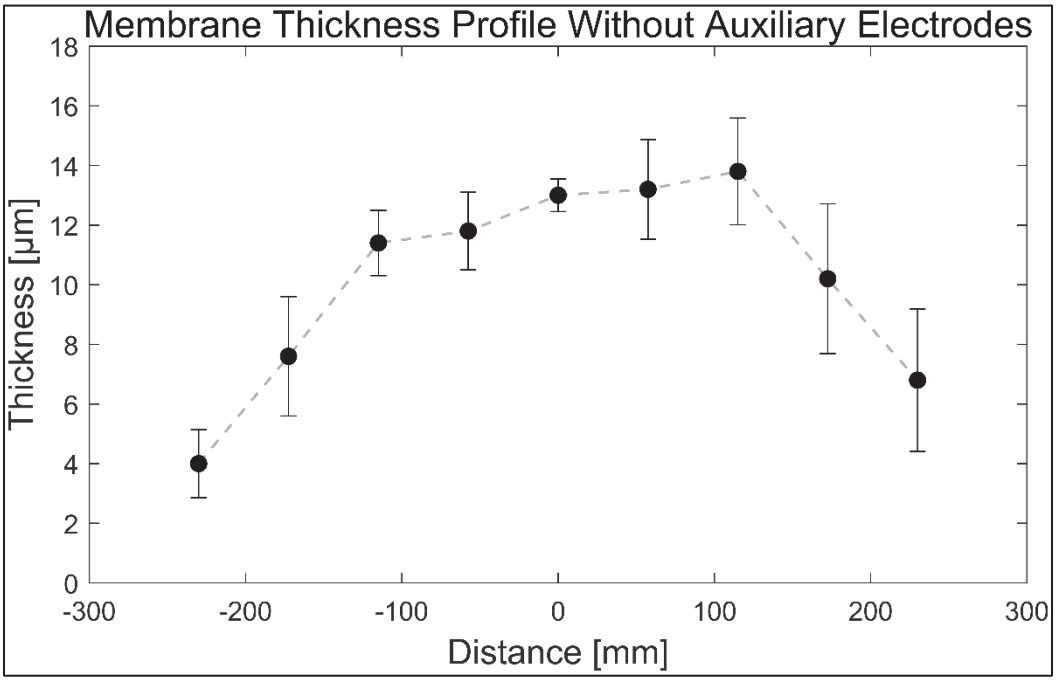

Figure 7.4 Thickness along the width of the membrane produced with initial setup (without auxiliary electrodes); the dashed line is only a guide for the eyes

These deposition non-uniformities are due to electric field interaction between the needles. A theoretical explanation for this phenomenon is presented in the discussion section.

This issue was resolved using parallel plate auxiliary electrodes: a folded aluminum foil sheet was positioned on each side of the needle array, both connected to the same voltage source as the needles (15 kV with −15 kV at the collector). This improved setup is presented in Figure 7.5, where the parallel plate auxiliary electrodes are shown within the red circles.

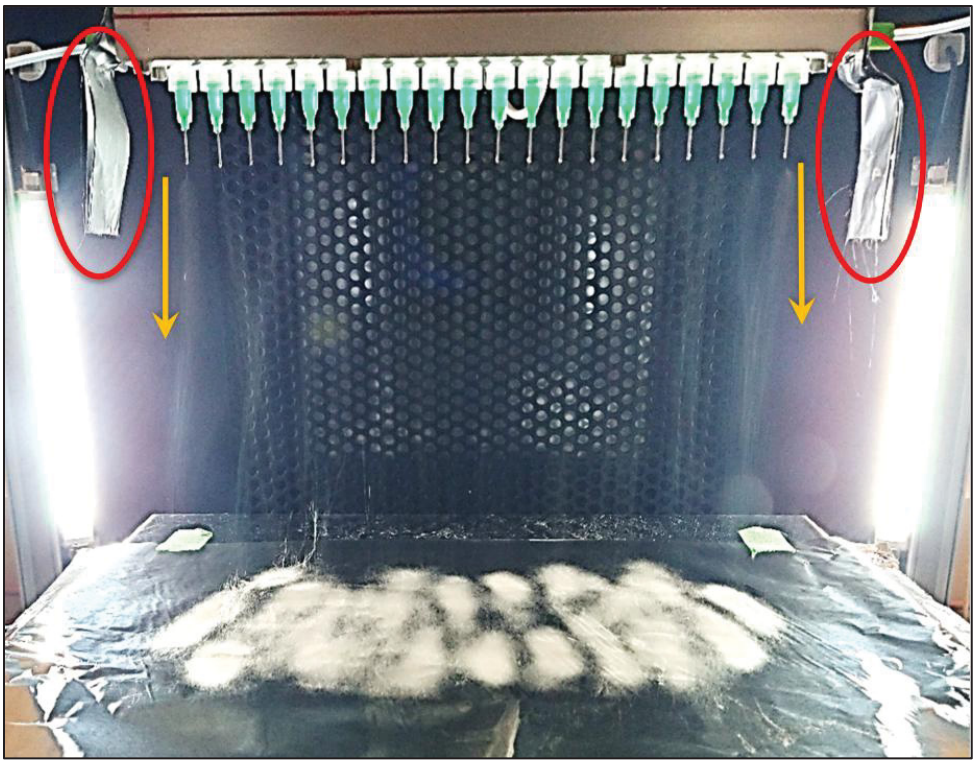

Figure 7.5 Multi-needle electrospinning with parallel plate auxiliary electrodes (indicated in red)

Figure 7.5 also shows, as indicated by the orange arrows, that when parallel plate auxiliary electrodes are used, no deflection of the electrospinning jets is observed. This results in a greatly improved, uniform deposition pattern (Figure 7.6).

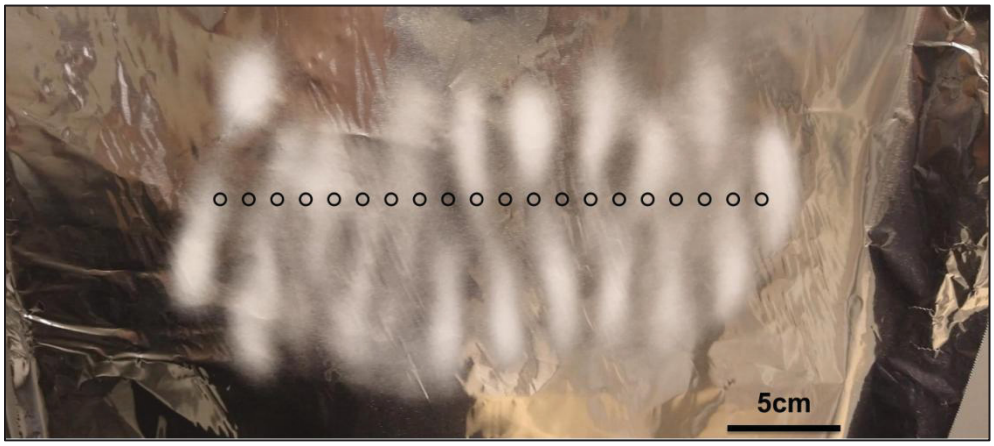

Figure 7.6 Deposition pattern with parallel plate auxiliary electrodes; black circles represent needle position

After the introduction of the parallel plate auxiliary electrodes, the deposition pattern no longer shows distinctive middle and side sections. It is at this point relevant to mention that, since most scaled-up electrospinning systems use either a conveyor belt or a rotative drum as the collector, fiber deposition will be uniform over both the width and the length of the produced membranes, due to the motion of the collector. Representative SEM images are shown in Figure 7.7, confirming that the diameters of the produced fibers no longer vary significantly across the deposition width.

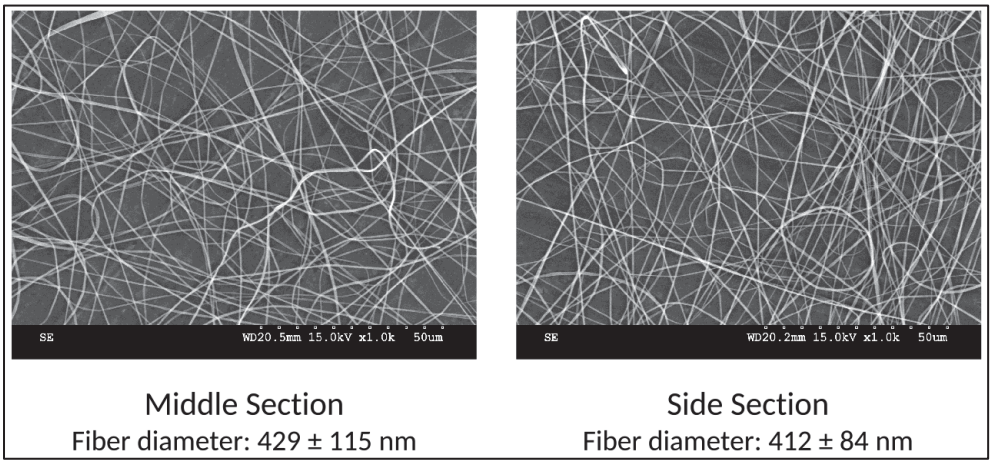

Figure 7.7 Example of the fibers from the middle and from the side with parallel plate auxiliary electrodes

Using this optimized fiber-producing technique that includes the parallel plate auxiliary electrodes, large nonwoven polymer nanofiber membranes were electrospun using a conveyor as the collector, as shown in Figure 7.8. The thickness profile along the width of the membrane, presented in Figure 7.9, shows that fibers were contained within a narrower span and uniform thickness was obtained.

Figure 7.8 Production of large nonwoven membranes

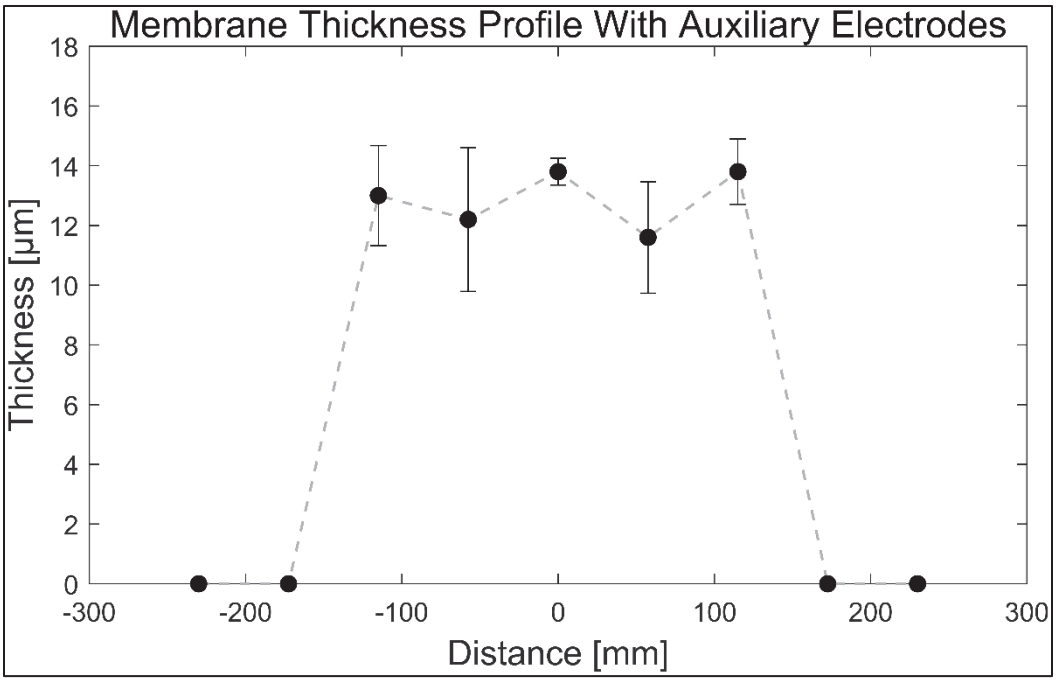

Figure 7.9 Thickness along the width of the membrane with parallel plate auxiliary electrodes, the dashed line is only a guide for the eyes

7.4 Discussion

To better understand the experimental observations, the electric field intensity across the needle array was computed using COMSOL. To do so, a 3D geometry was used, as presented in Figure 7.10. Cylinders were used to model the needles, as presented in the geometry shown in isometric perspective, Figure 7.10. The same applied voltage, inter-needle distance, and needle-to-collector distance were used as for the experiment, which is to say 30 kV, 13 mm, and 20 cm, respectively. An air domain of 400 × 150 × 250 mm (width × depth × height) was used to surround the needles and the collector. The size of the collector was 350 × 100 × 10 mm. The electric field was calculated 1 mm below the array of needles, consistent to what is customarily reported in the literature (Zhu et al., 2019; Zhu et al., 2018). The results of the simulation are presented in Figure 7.11, where each peak corresponds to a needle.

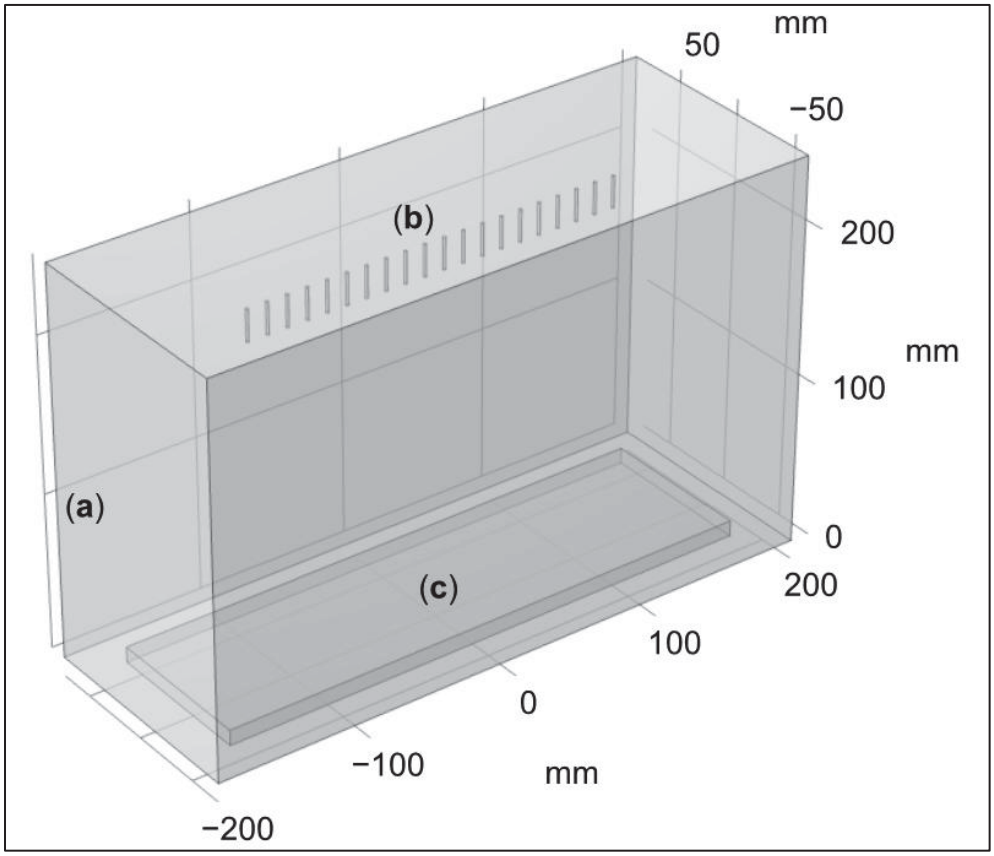

Figure 7.10 COMSOL 3D geometry, (a) air domain, (b) needles, (c) collector

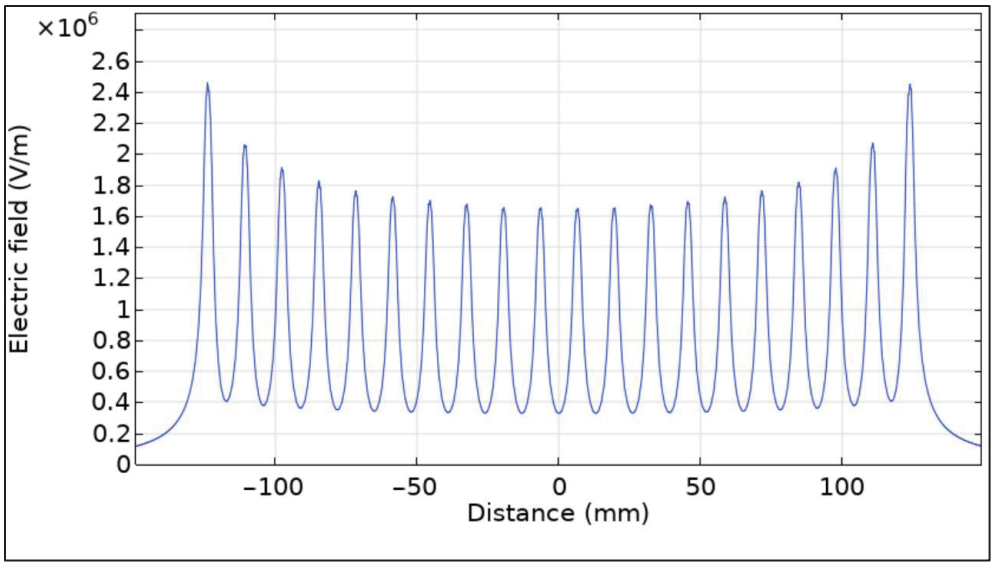

Figure 7.11 COMSOL electric field simulation initial setup (without auxiliary electrodes), showing the electric field 1 mm below the needle tips

Perhaps counterintuitively, the electric field near each needle depends greatly on the relative position of the needle along the needle array, as illustrated in Figure 7.11. Indeed, the model calculations confirm that the magnitude of the electric field 1 mm directly below the needle is approximately 50% greater for the needles located at the extremes of the needle array compared with the needles at the center of the array. This non-uniformity of the electric field is due to the interaction between needles: each needle acting as a positively charged electrode, imposing an electric field on its neighbor. A needle located in the center of the array will undergo the effect of these imposed electric fields from a similar number of needles on the right and left sides; the sum of these imposed electric fields of opposite directions will then cancel each other out. The situation will be different for needles located far from the center: in this case, the electric fields imposed from the neighboring needles on either side of a given needle will no longer cancel out, resulting in a net electric field greater than zero. This will, along with the electrical field toward the collector, result in an electric field of higher total magnitude.

This non-uniformity of the electric field due to the interaction between the needles explains the non-uniformities observed experimentally: indeed, during the electrospinning process, the electric field is responsible for pulling the polymeric jets out from the needles. An

inhomogeneous electric field will, therefore, result in unstable jets pulled at a deflected angle: the jets on the sides are pushed outward and are more dispersed, unlike the jets in the middle, that are constrained by their nearest neighbors.

It is well known in the literature that a stronger electric field causes a stronger stretching of the polymeric jet, resulting in smaller fiber diameters (Matabola & Moutloali, 2013). This explains why, in the unmodified multi-needle apparatus that lacks the auxiliary electrodes, the diameter of the fibers deposited away from the center of the needle array is smaller than of those deposited in the middle.

To resolve these issues, parallel plate auxiliary electrodes were implemented, as presented in the experimental section. This improved setup was modeled by adding lateral conducting plates that were subjected to the same voltage as the needles, as shown in the new geometry presented in Figure 7.12. The electric field was also computed 1 mm below the needle array, and the results are presented in Figure 7.13, where the peaks corresponding to the parallel plate auxiliary electrodes are shown within the red circles.

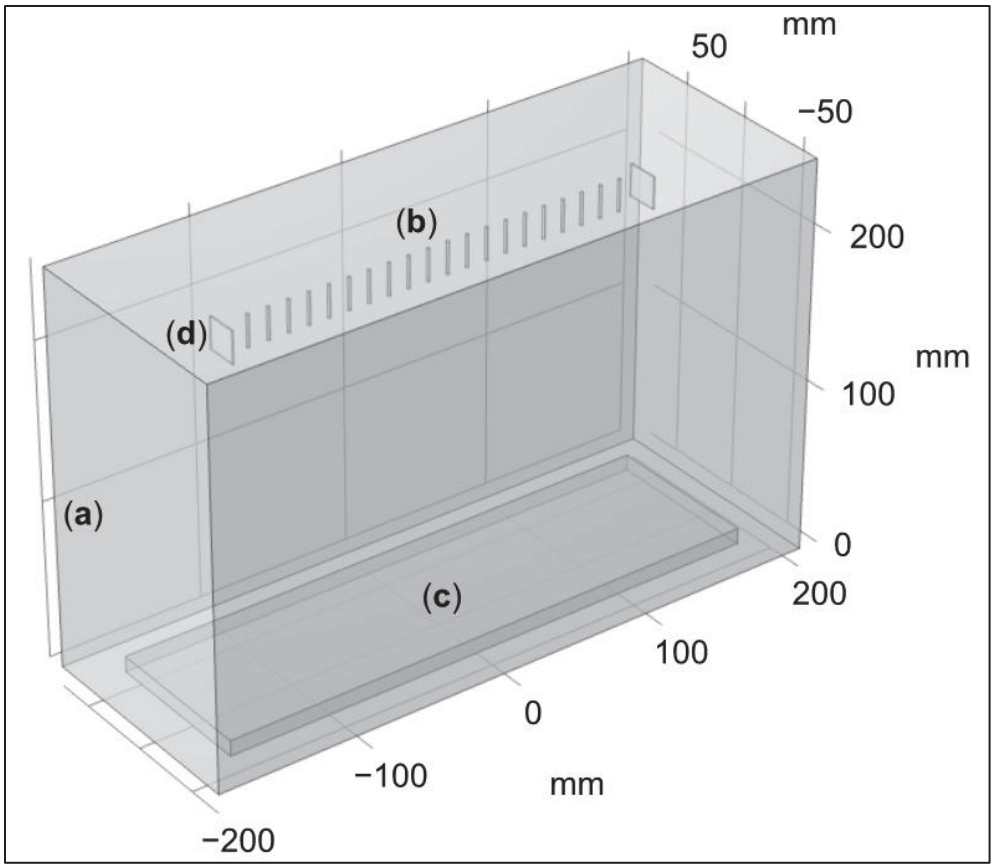

Figure 7.12 COMSOL Geometry with auxiliary electrodes (a) air domain, (b) needles, (c) collector, (d) auxiliary electrodes plate

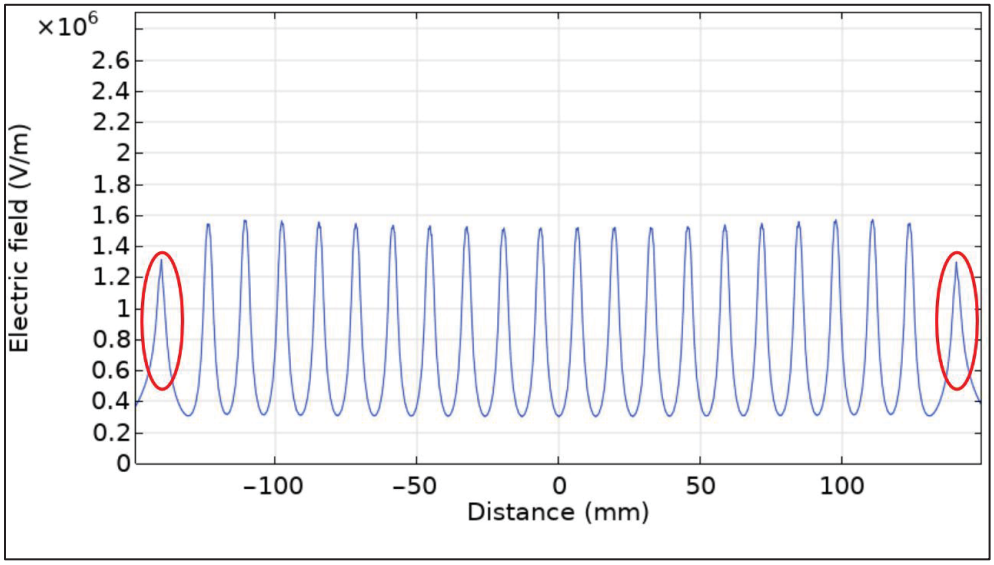

Figure 7.13 COMSOL electric field simulation with auxiliary electrodes, where the peaks corresponding to the parallel plates auxiliary electrodes are shown within the red circles

As illustrated in Figure 7.13, an almost perfectly uniform electric field distribution can be obtained using this parallel plate auxiliary electrode geometry. This uniformization can be explained by considering that the lateral auxiliary electrodes impose an additional electric field on the needles. If the strength of the imposed electric field coming from these auxiliary electrodes is equal to the strength of the imposed electric field coming from the neighboring needles, both sets of electric fields will cancel each other out. The strength and direction of the electric field imposed by the auxiliary electrodes can be optimized by changing the distance between the auxiliary electrodes and the needles, and by changing the auxiliary electrode geometry. Finite element modeling shows that a uniformly distributed electric field along the needle array can be achieved by using parallel auxiliary electrode plates of 20 × 20 mm placed at a distance of 16 mm from the nearest needles.

Experimentally, it was found that the auxiliary electrode plates had to be made a little longer (approximatively 3.5 cm) to compensate for the Coulombic repulsion of the charged jets. Since any electrical charge on the polymeric jets was unaccounted for in the equilibrium-state finite element model, this was to be expected.

When properly optimized, the lateral auxiliary electrode plates repel the side jets with the same strength as the other needles, realigning the jets toward the collector and eliminating the deflection angle. Since all the electrospinning jets are now vertically oriented directly toward the collector, the fibers are deposited uniformly. We, therefore, find that the uniformity of the electric field obtained across the needles using parallel auxiliary electrode plates creates the necessary stable processing conditions for the production of high-quality fibers of homogeneous diameter.

Parallel plate auxiliary electrodes have, therefore, proven to be a simple and efficient way to optimize the multi-needle electrospinning process. The simulation results were found to be in agreement with the experimental results. Since no semi-vertical jets were observed, a uniform deposition pattern was produced. Since fiber diameter along the needle array was found to be

uniform, it can be, reasonably, concluded that the electric field is quite uniform, which indicates steady processing conditions.

7.5 Conclusion

The use of a multi-needle apparatus seems an obvious way to scale up the electrospinning process to increase production yields. However, as numerous researchers have found, such an implementation suffers from unstable processing parameters due to the non-uniformity of the electric field, resulting in the deflection of electrospinning jets that cause heterogenous fiber deposition and membrane thickness, as well as poor fiber diameter control.

We found that this challenge can be readily overcome by introducing parallel auxiliary electrode plates that confine the needle array. Experimental observations and finite element computational models confirm that the introduction of these additional electrodes achieves uniformity of the electric field along the needle array. This greatly improves the process parameter controls, thereby enabling the scaled-up high-yield production of good quality, homogeneous polymeric nanofibers using the electrospinning technique.

CONCLUSION

This thesis investigated strategies to scale up electrospinning by combining rheological characterization of polymer solutions with electric field optimization in multi-needle systems. Together, these two approaches addressed the central limitations that have long hindered the translation of electrospinning from laboratory studies to industrially relevant production.

On the rheology side, a custom Capillary Breakup Extensional Rheometer (CaBER) was designed and constructed to enable precise characterization of low-viscosity, viscoelastic solutions representative of electrospinning formulations. By integrating controlled-humidity experiments and an evaporation–diffusion model, it was shown that solvent loss during filament thinning can artificially increase apparent viscosity and relaxation times, thereby conflating intrinsic elasticity with evaporation-induced effects. This demonstrated that environmental control is essential for reliable interpretation of extensional measurements on volatile polymer solutions. Beyond this, systematic studies of polymer formulations revealed the critical role of molecular weight distribution and long-chain content in governing extensional rheology and fiber formation. In particular, elastic doping with trace amounts of high-molecular-weight chains enabled fiber formation from otherwise unspinnable low-molecular-weight matrices, while simultaneously permitting a fivefold increase in polymer throughput for this system.

On the process engineering side, the thesis addressed the challenge of scaling up electrospinning using multi-needle arrays. While such arrays promise linear increases in production capacity, they are plagued by non-uniform electric fields that destabilize jets and compromise fiber quality. Through combined experiments and finite element simulations, this work demonstrated that introducing parallel plates auxiliary electrodes can homogenize the electric field across a twenty-needle array, thereby stabilizing jet trajectories and enabling consistent fiber deposition. As a result, multi-needle electrospinning was shown to achieve a twentyfold increase in yield while maintaining fiber uniformity comparable to single-needle operation.

Taken together, these results demonstrate that scaling up electrospinning requires an integrated strategy that addresses both the solution physics (through extensional rheology and formulation design) and the process physics (through electric field uniformization in multi-needle setups). By bridging these two complementary paths, this thesis provides both fundamental insights into the physics of electrospinning scale-up and practical design rules for enabling high-throughput production of nanofiber membranes without sacrificing quality.

RECOMMENDATIONS

The results presented in this thesis advance the understanding of rheology–electrospinning interactions and propose strategies for multi-needle scale-up. At the same time, they open several avenues for further investigation, both to deepen the scientific understanding and to address practical challenges on the path to industrial implementation. The following recommendations are organized according to the main research objectives of the thesis.

Objective A – Rheology for Electrospinning

- **Refinement of solvent evaporation modeling**
  Future models should account for a concentration-dependent diffusion coefficient and refine the evaporation coefficient to reflect the influence of a moving and continuously stretched surface. Such refinements would better capture solvent transport dynamics during high-speed deformations.

- **Exploration of surface phenomena**
  Extending CaBER and electrospinning studies to a wider range of polymer–solvent systems would help generalize the conclusions. Particular attention should be given to interfacial phenomena in CaBER, since polymer–solvent interactions and solvent quality may promote or hinder chain or additive migration to the surface. Such effects can lead to skin formation, which would significantly alter the rheological behavior of the filament. A deeper understanding of these mechanisms could, in turn, be exploited to further optimize the electrospinning process.

- **Chain recruitment and relaxation dynamics**
  Further work, both theoretical and experimental, is recommended to elucidate the relationship between molecular weight distribution, deformation history, and relaxation time. In particular, the progressive recruitment of progressively shorter chains during filament thinning means that elastic stresses accumulate until they collectively balance the capillary stress, as described by Calabrese et al. (2025) (Calabrese et al., 2025).

Once this balance is reached, thinning proceeds on a timescale governed by the relaxation spectrum of the recruited chains (Entov & Hinch, 1997). This mechanism implies that the relaxation time measured in CaBER is not solely determined by molecular weight distribution, as shown in this work, but is also influenced by filament geometry and experimental conditions, which in turn shape the total deformation history and the deformation rate profile experienced by the filament. Comparisons between extremely fast deformation in electrospinning and slower deformation in CaBER may reveal new scaling relationships linking relaxation time to the deformation profile.

Objective B – Scale-Up with Multi-Needle Systems

- **Alternative geometries and configurations**

  The auxiliary electrode strategy demonstrated here could be extended to larger arrays, with square multi-needle configurations providing a simple yet effective route to further scale up fiber production.

- **Long-term stability and industrial robustness**

  Industrial adoption of the electrospinning technique would benefit from a stable long-term continuous operation. Future studies should therefore address practical issues such as needle clogging, continuous solution dispensing, solvent accumulation, and charge buildup.

Beyond Electrospinning: Potential of Solution Blowspinning

Finally, beyond the scope of the specific objectives of this thesis, solution blow spinning (SBS) merits consideration as a complementary route toward industrial-scale nanofiber production. SBS has been demonstrated to achieve fiber production rates on the order of ten times higher than electrospinning, making it attractive for industrial translation. However, the technique is more sensitive to nozzle geometry and processing conditions, perhaps requiring precise tuning for each polymer–solvent system. Moreover, SBS faces limitations compared to electrospinning, including broader fiber diameter distributions, reduced control over

morphology, and an inability to produce complex architectures such as core–shell fibers. Future work should therefore address the sensitivity of SBS to processing parameters and nozzle geometry, with the aim of improving fiber uniformity and enabling more versatile architectures. Despite these constraints, its markedly higher throughput per nozzle highlights SBS as a promising technology to help bridge the gap between laboratory-scale research and industrial-scale nanofiber manufacturing.

APPENDIX I

CaBER Parts List

This appendix provides the bill of materials (BOM) for the custom Capillary Breakup Extensional Rheometer (CaBER). Figure-A I-1 and Figure-A I-2 show the mechanical assembly and the complete system, respectively, with numbered callouts identifying the main components. Table-A I-1 presents the full list of parts, with detailed information. Some components are not represented in the figures but are included in the table as they are essential to the operation of the system.

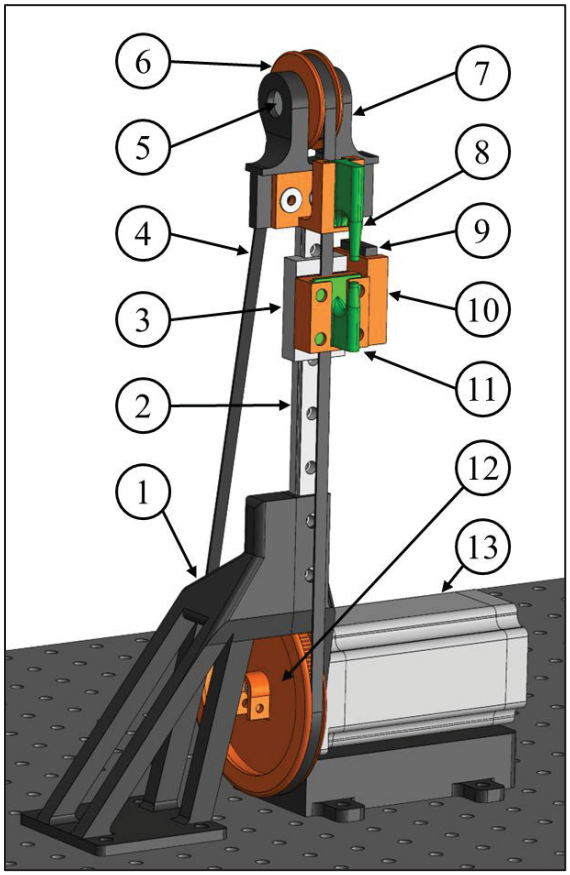

Figure-A I-1 Mechanical assembly of the custom Capillary Breakup Extensional Rheometer (CaBER); numbered callouts identify the main mechanical components, with detailed information provided in Table-A I-1

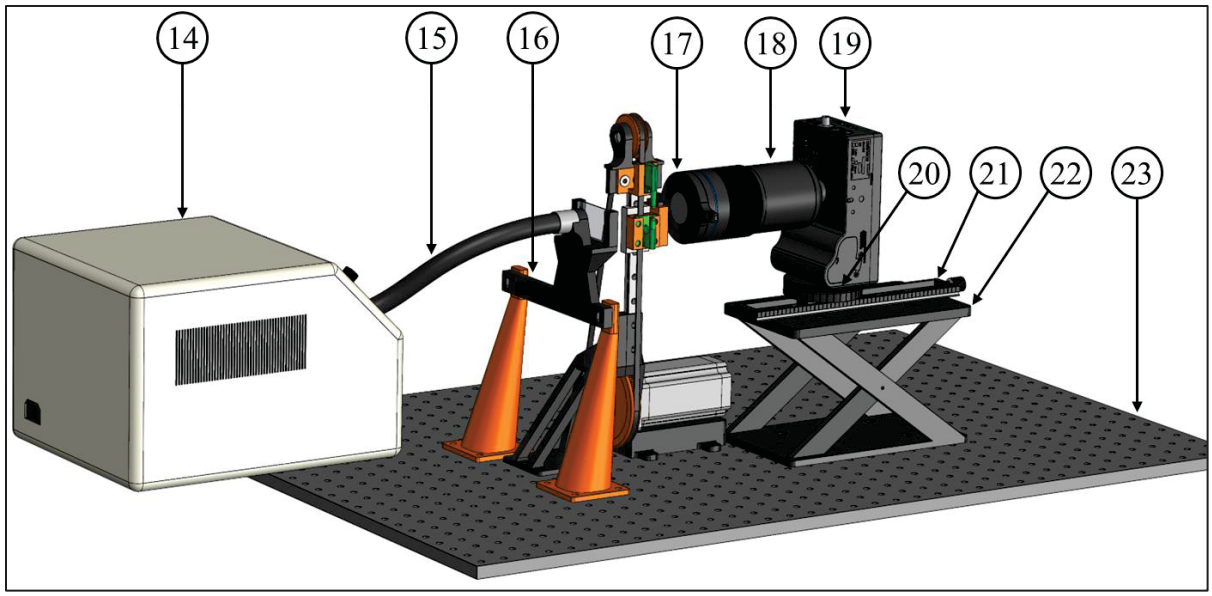

Figure-A I-2 Complete CaBER system, including the optical subsystem; numbered callouts identify the main components, with detailed information provided in Table-A I-1

Table-A I-1 Bill of materials for the custom CaBER

Part No.	**Name**	**Specification**	**Notes / Function**
1	Custom mounting support	3D printed, PLA, SolidWorks custom design	Secures rail, motor and breadboard together
2	Linear translation rail	200mm MGN12 Linear Rail Guide, steel	
3	Carriage (slider)	MGN12H Carriage, steel bearing	
4	Timing belt	6mm timing belt GT2, made of PU with steel core	
5	Ball bearing	Bearing ½ inch bore R8-2RS double rubber sealed roller, alloy steel	
6	Top gear	3D printed, PLA, SolidWorks custom design	
7	Upper rail assembly	3D printed, PLA, SolidWorks custom design	Secures bearing, top gear and rail together

Part No.	Name	Specification	Notes / Function
8	Top plate	3D printed, PLA, SolidWorks custom design	
9	Limit switch	Twidec micro limit Switch KW11-3Z-04, 5A, normally open	Provides to electronic the "Zero" (topmost) position of the carriage
10	Carriage assembly	3D printed, PLA, SolidWorks custom design	Secures carriage, belt, switch and bottom plate together
11	Bottom plate	3D printed, PLA, SolidWorks custom design	
12	Bottom gear	3D printed, PLA, SolidWorks custom design	Transfer motor motion to belt
13	Stepper motor	Stepperonline stepper motor nema 23, 3Nm	
14	Illuminator	MI-152 fiber optic illuminator	Provide light
15	Optical fiber	Flexible fiber optic light guide ½" x 48"	Transport light
16	Light holder and diffuser	3D printed, PLA, SolidWorks custom design	Hold optical fiber aligned and diffuse light
17	Snap-on lens	Raynox DCR-250 super macro snap-on lens, 250mm	Provides extra magnification
18	Lens	Laowa 100 mm f/2.8 2:1 ultra-macro APO lens	Provides adjustable magnification, aperture and focal point

Part No.	Name	Specification	Notes / Function
19	Camera	Chronos 2.1-HD high speed camera, 4/3" colour sensor, max resolution 1920x1080 @ 1000fps, min 640x96 @ 24,046fps, 32GB	
20	Geared tripod head	Sunwayfoto GC-01 geared head,	Rotational adjustment of the camera
21	Focusing rail	NiSi NM180S macro focusing rail, 180mm	Forward/backward adjustment of camera, used for precise focus
22	Z-axis platform	Huanyu Z-Axis Manual Lift Platform 60mm	Height adjustment of camera
23	Optical breadboard	36" x 24", Breadboard, 0.5" thickness, mounting threads ¼-20 on 1"	Steady base of the machine
24	Arduino board	Arduino mega 2460 REV3, 16MHz	Motion control
25	Motor driver	StepperOnline digital stepper driver 1.8-5.6A 20-50VDC	Drive motor from Arduino control
26	Power supply	InShareplus 24V 6.5A 150W, DC universal regulated switching power supply	
27	Emergency Stop	xuteuk 22mm Red Mushroom Emergency Stop Push Button Switch with Light 440V 10A LAY37-11ZSD	

APPENDIX II

CaBER Arduino Program

This appendix presents the Arduino program developed to control the custom Capillary Breakup Extensional Rheometer (CaBER). The program manages the step displacement of the lower plate by controlling the total number of steps performed by the stepper motor. The actual travel distance of the bottom plate depends on the "step per turn" defined on the motor's driver, as well as the exact dimensions of the mechanical parts. Calibration was therefore performed for precise actuation. Arduino IDE 2.2.1 was used.

The program waits for user input in the serial monitor. Input "0" raises the carrier until the limit switch is activated, defining the zero position. Once at position 0, inputs "1" and "2" are available: input "1" performs the accelerated step stretch, while input "2" moves the carrier slowly to a lower position, typically used for cleaning.

The complete source code is reproduced below, for readability, indentation was removed.

```
// Arduino program for controlling the CaBER stretching unit.
// Functions: homing (zero), step displacement to top/low positions,
// controlled acceleration/deceleration.
// Uses stepper motor with configurable step delay for speed control.

#define directionPin 2
#define stepPin 3
#define stepsPerRevolution 6400
#define switchPin 4

#include <math.h>

int position = 5;
int switchValue = 0;
int low_pos = 2000;
int bot_pos = 1000;

int speed_0 = 750;
int speed_1 = 200;

int speed_a = 1000;
int speed_2_1 = 300;
int speed_2_2 = 300;

double total_steps = 200;        // Total number of steps
double acceleration_length = 15; // Length of acceleration (number of steps)
double deceleration_length = 20; // Length of deceleration (number of steps)
```

```
double slow_delay = 800;
double fast_delay = 150;
double delay_a = slow_delay;

double acceleration_factor = 0;
double deceleration_factor = 0;

void setup() {
pinMode(directionPin, OUTPUT);
pinMode(stepPin, OUTPUT);
Serial.begin(9600);
switchValue = digitalRead(switchPin);
while (!Serial);
Serial.println("\r\n\r\n\r\n\r\n\r\n\r\n*******************************");
Serial.println("Initialisation done correctly!");
Serial.println("*******************************\r\n\r\n\r\n\r\n\r\n\r\n");
}

void loop() {
Serial.println("*******************************");
Serial.println("Choose a function: zero (0), top (1) or low (2)");
Serial.println("*******************************\r\n\r\n\r\n\r\n\r\n\r\n");
while (!Serial.available()); // wait for user input
String input = Serial.readStringUntil('\n'); // read input text

if (input == "0" || input == "zero" || input == "top") {
Serial.println("pos 0 \r\n\r\n\r\n\r\n\r\n\r\n");
switchValue = digitalRead(switchPin);
while (switchValue == 1) {
MoveOneStep(HIGH, speed_0);
switchValue = digitalRead(switchPin);
}
delay(200);
MoveOneStep(LOW, speed_0);
position = 0;

} else if (input == "1" || input == "top") {
Serial.println("pos 1 \r\n\r\n\r\n\r\n\r\n\r\n");
if (position == 0) {
unsigned long startTime = micros(); // Record the start time
for (int i = 0; i <= total_steps; i++) {
if (i < acceleration_length) {
acceleration_factor = i / acceleration_length;
delay_a = slow_delay - ((slow_delay - fast_delay) * pow(acceleration_factor, 0.5));
} else if (i > acceleration_length && i <= (total_steps - deceleration_length)) {
delay_a = fast_delay;
} else if (i > (total_steps - deceleration_length)) {
deceleration_factor = (i - (total_steps - deceleration_length)) / deceleration_length;
delay_a = fast_delay + (slow_delay - fast_delay) * pow(deceleration_factor, 2);
}
MoveOneStep(LOW, delay_a);
}
unsigned long endTime = micros(); // Record the end time
unsigned long executionTime = endTime - startTime; // Calculate the execution time
Serial.print("Execution time: ");
Serial.print(executionTime / 1000);
Serial.println(" miliseconds");
position = 2;
}
}

else if (input == "2" || input == "low") {
Serial.println("pos 2 \r\n\r\n\r\n\r\n\r\n\r\n");
if (position == 0) {
for (int i = 0; i < low_pos; i++) {
MoveOneStep(LOW, speed_2_1);
}
position = 2;
delay(400);
```

```
for (int i = 0; i < (bot_pos - low_pos); i++) {
MoveOneStep(LOW, speed_2_2);
}
}
}

else {
Serial.println("invalid input\r\n\r\n\r\n\r\n\r\n\r\n");
}
}

int MoveOneStep(int dir, long wait) {
digitalWrite(directionPin, dir);
digitalWrite(stepPin, HIGH);
delayMicroseconds(wait);
digitalWrite(stepPin, LOW);
}
```

APPENDIX III

CaBER MATLAB Programs

This appendix presents the MATLAB programs developed to extract filament diameter $D(t)$ from high-speed image sequences acquired during CaBER experiments. The workflow processes each frame sequentially, converts images to grayscale, binarizes using a calibrated threshold, detects left and right edges row-wise within a user-defined region of interest (ROI), and derives a representative filament diameter per frame (either the minimum or the mode, depending on the fluid behavior). Processing automatically stops once the measured diameter falls below 10 pixels (~34 μm at maximum magnification).

Requirements and file structure

The programs assume that all images from each sample are stored in a dedicated folder named after the sample number (e.g., for sample #550: `D:\CaBER_data_SSD_2\550\`). Within this folder, image files must be named sequentially as `frame_000001.tiff`, `frame_000002.tiff`, and so forth, as automatically generated by the Chronos camera. The base path is defined directly in the code of `Boucle_v3.m` and can be modified if necessary. Each program reads all frames between the selected start and end indices, while parameters such as the camera frame rate, intensity threshold, and ROI rows must be specified by the operator at the beginning of the main scripts.

Program architecture

The source code is organized into three operator-facing main scripts, supported by a set of helper functions:

- `Image_caber.m` — Processes a single image interactively to test ROI placement and threshold values before running full sequence analyses.
- `Rheology_newtonian.m` — Analyzes full image sequences, extracts D(t), and fits the Papageorgiou visco–capillary equation to calculate the solution viscosity within a user-defined time window `[Ts,Te]`.

- `Rheology_elastic.m` — Analyzes full image sequences, extracts $D(t)$, and fits an exponential thinning law to determine the relaxation time (λ) within a user-defined time window `[Ts,Te]`.

The three main scripts rely on the following helper functions:

- `count_num_frames.m` — Counts the number of frames (frame_*.tiff) in a given sample folder.
- `Boucle_v3.m` — Batch loop that processes all frames in a sequence and returns representative diameters in pixels (min or mode).
- `thickness_measure_v2.m` — For a single image: loads and orients, converts to grayscale, thresholds, detects edges row-wise, computes local filament thickness profile within the ROI, and returns the profile in pixels.
- `edge_threshold.m` — Converts a grayscale image into a binary edge map based on a calibrated intensity threshold (used by `thickness_measure_v2`).

The complete source code of the three main scripts is reproduced below, followed by the helper functions. Each listing is provided in full as implemented during this project. For readability, indentation was removed.

`Image_caber.m`

```
clc;
clear;
clf;

% Parameters
sample_number = 550;
file_number = 80;
start_row = 400;
end_row = 1000;
scale_mm = 880.5942 / 3; % pixels per mm
threshold = 80;

% Load image
filename = sprintf('D:\\CaBER_data_SSD_2\\%d\\frame_%06d.tiff', sample_number, file_number);
input_img = imread(filename);

% Rotate if landscape
[height, width, ~] = size(input_img);
if width > height
img = imrotate(input_img, -90);
else
img = input_img;
end
```

```
% Convert to grayscale
gray = im2gray(img);

% === FIGURE 1: Grayscale image ===
figure(1);
imshow(gray);
title('Grayscale Image');

% === Apply edge detection ===
edges = edge_threshold(gray, threshold);

% === FIGURE 2: Edges ===
figure(2);
imshow(edges, []);
title('Edge Detection');

% === EDGE DETECTION TABLES ===
for y = 1:size(edges, 1)
i = 1;
while edges(y, i) == 0
i = i + 1;
if i >= size(edges, 2), break; end
end
table_left(y) = i;

i = size(edges, 2);
while edges(y, i) == 0
i = i - 1;
if i <= 1, break; end
end
table_right(y) = i;
end

% === FIGURE 3: Edge profile ===
figure(3);
set(gcf, 'Units', 'centimeters', 'Position', [5, 5, 7, 12]);
line([1, size(edges, 2)], [start_row, start_row], 'Color', 'red', 'LineStyle', '--');
line([1, size(edges, 2)], [end_row, end_row], 'Color', 'red', 'LineStyle', '--');
hold on;
x = 1:size(edges, 1);
plot(table_left, x, 'b');
plot(table_right, x, 'g');
set(gca, 'YDir', 'reverse');
xlabel('Distance from Image Side [pixels]');
ylabel('Vertical Position [pixels]');
ylim([0, size(edges, 1)]);
xlim([0, size(edges, 2)]);
box on;
title('Detected Edge Position');

% === THICKNESS COMPUTATION ===
for i = start_row:end_row
thickness(i - start_row + 1) = table_right(i) - table_left(i);
end

% === FIGURE 4: Thickness ===
figure(4);
set(gcf, 'Units', 'centimeters', 'Position', [5, 5, 7, 12]);
plot(thickness, 'k');
ylim([30, 110]);
xlim([0, end_row - start_row]);
xlabel('Vertical Position in ROI [pixels]');
ylabel('Filament Diameter [pixels]');
box on;
title('Filament Diameter Profile');

% === Display thickness value ===
th = min(thickness);
```

```
disp([num2str(th) ' pixels = ' num2str(th / scale_mm) ' mm = ' num2str(th * 1000 / scale_mm) '
µm']);

% Export options
%exportgraphics(figure(1), 'Name1.tif', 'Resolution', 1200);
%exportgraphics(figure(2), 'Name2.tif', 'Resolution', 1200);
%exportgraphics(figure(3), 'Name3.tif', 'Resolution', 1200);
%exportgraphics(figure(4), 'Name4NarrowYajusted.tif', 'Resolution', 1200);
```

Rheology_newtonian.m

```
clc
clear
clf

%Informations needed
sample_number = 2222;
fps = 2000;
scale_mm = 541.1854/6; %pixels
threshold = 200;
st_mm = 20.1; %mN/m
start_frame = 1;
finish_frame = 4000;
start_row = 250;
end_row = 1000;

Ts = 0.00; % Time to start modeling [sec], automatic if 0
Te = 0.015; %Time to stop modeling [sec], automatic if 0
min_pixel = 9; %stop the data string for diameter smaller than "mi_pixel" pixels.;

scale = scale_mm * 1000;% convert to meters
st = st_mm/1000;

%Count the qt of pictures to select them all
num_frames = count_num_frames(sample_number);

% measure_mode : mode = 1, min = 2
measure_mode = 2;

[datas] = Boucle_v3(sample_number, start_frame, num_frames, threshold, start_row, end_row,
measure_mode);

i = 1;
while datas(i) > min_pixel && i < size(datas, 1)
data_m(i, 1) = datas(i) / scale;
i = i + 1;
end

%creat time table
for i = 1:size(data_m)
time_table(i, 1) = i * (1/fps) - 1/fps;
end

if Te == 0
Te = size(data_m, 1)/fps;
end

% Equation
equation = @(n, tc, t) 2 * 0.0709 * st * (tc - t) / n;

% Initial guess for parameters
n0 = 1;   % Initial guess for viscosity [Pa*s]
tc0 = 0.1; % Initial guess for pinch-off time [s]
% Define lower boundary and upper boundary for n and tc
lb_n = 0.0001;
lb_tc = 0.0001;
ub_n = 1000;
ub_tc = 100;
```

```
x0 = [n0, tc0];
lb = [lb_n, lb_tc];
ub = [ub_n, ub_tc];

% Find indices corresponding to the specified time range
start_idx = find(time_table >= Ts, 1);
end_idx = find(time_table <= Te, 1, 'last');

% Filter the time and data within the specified time range
time_range = time_table(start_idx:end_idx);
data_range = data_m(start_idx:end_idx);

% Perform parameter optimization
options = optimoptions('lsqcurvefit', 'OptimalityTolerance', 1e-15, 'FunctionTolerance', 1e-
15);
parameters = lsqcurvefit(@(x, time_range) equation(x(1), x(2), time_range), x0, time_range,
data_range, lb, ub, options);

% Extract optimized parameters
n = parameters(1);
tc = parameters(2);

% Calculate fitted values using the optimized parameters
fittedData = equation(n, tc, time_table);

% Plot the experimental data and fitted curve
plot(time_table(:, 1), data_m, 'o', time_table(:, 1), fittedData(:, 1));
xline(Ts, '--b'); % Modeling Start
xline(Te, '--r'); % Modeling Stop
xlabel('Time [s]');
ylabel('Diameter [m]');
yyaxis right;
hold on
ax = gca;
ax.YColor = 'k';
legend('Experimental Data', 'Fitted Curve', 'Modeling Start', 'Modeling Stop');
mean_data = mean(data_m);
TSS = sum((data_m - mean_data).^2);
RSS = sum((data_m - fittedData(:, 1)).^2);
R_squared = 1 - (RSS / TSS);
nu = length(data_m);
RMSE = sqrt(RSS / (nu - 1));
info_str = sprintf("n = %.4f [Pa*s], Sample number : %.0f", n, sample_number);
title(info_str);

n*1000

% % SAVE DATA (optional)
% dataMatrix = [time_table(:), data_m(:)];
% [filename, filepath] = uiputfile('*.csv', 'Save As');
% if ~(isequal(filename,0) || isequal(filepath,0))
% fullFilePath = fullfile(filepath, filename);
% writematrix(dataMatrix, fullFilePath);
% disp(['Data saved to: ', fullFilePath]);
% end
```

Rheology_elastic.m

```
clc
clear
clf

%Informations needed
sample_number = 434;
fps = 500;
%sample_number = 1251;
TS_number = 0;

Ts = TS_number / fps; % Time to start modeling [sec]
```

```
Ts = 0.2;

Te = 0; %Time to stop modeling [sec], Te=0 : stop at the end of data set

scale_mm = 1254.5984/7; %pixels / mm
threshold = 46;

st_mm = 46.7; %mN/m
start_frame = 1;
finish_frame = 10000;
start_row = 200;
end_row = 800;

min_pixel = 9; %stop the data string for diameter smaller than "mi_pixel" pixels.;

scale = scale_mm * 1000;% convert to meters
st = st_mm/1000;

%Count the qt of pictures to select them all
num_frames = count_num_frames(sample_number);

% measure_mode : mode = 1, min = 2
measure_mode = 1;

[datas] = Boucle_v3(sample_number, start_frame, num_frames, threshold, start_row, end_row,
measure_mode);
i = 1;
while datas(i) > min_pixel && i < size(datas, 1)
data_m(i, 1) = datas(i) / scale;
i = i + 1;
end

%creat time table
for i = 1:size(data_m)
time_table(i, 1) = i * (1/fps) - 1/fps;
end

e_dot = zeros(size(data_m));
%deformation rate
for i = 3:size(data_m) - 2
e_dot(i) = (data_m(i-2) - data_m(i+2))/((time_table(i+2) - time_table(i - 2))*data_m(i));
end

if Te == 0
Te = size(data_m, 1)/fps;
end

% Find the index in time_table closest to Ts
[~, idx_Ts] = min(abs(time_table - Ts));

% Retrieve the value of data_m at Ts
R0 = data_m(idx_Ts)/2;

% Equation
%equation = @(L, G, t) R0*(R0*G/(2*st))^(1/3)*exp(-t/(3*L));
equation = @(L, G, t) G*exp(-t/(3*L));

% Initial guess for parameters
L0 = 0.1;  % Initial guess for parameter L
G0 = 150;  % Initial guess for parameter G
lb_L = 0.0001;
lb_G = 0.000001;
ub_L = 10;
ub_G = 100000000;
x0 = [L0, G0];  % Initial guess for parameters L and G
lb = [lb_L, lb_G];
ub = [ub_L, ub_G];

% Find indices corresponding to the specified time range
```

```
start_idx = find(time_table >= Ts, 1);
end_idx = find(time_table <= Te, 1, 'last');

% Filter the time and data within the specified time range
time_range = time_table(start_idx:end_idx);
data_range = data_m(start_idx:end_idx);

% Shift time to start at Ts (i.e., reset time to zero at Ts)
time_shifted = time_range - Ts;

% Perform parameter optimization
options = optimoptions('lsqcurvefit', 'StepTolerance', 1e-6, 'OptimalityTolerance', 1e-20,
'FunctionTolerance', 1e-20);
parameters = lsqcurvefit(@(x, time_shifted) equation(x(1), x(2), time_shifted), x0,
time_shifted, data_range, lb, ub, options);

% Extract optimized parameters
L = parameters(1)
G = parameters(2);

% Calculate fitted values using the optimized parameters
fittedData_range = equation(L, G, time_shifted);

plot(time_table(:, 1), data_m, 'o', time_range, fittedData_range);
xline(Ts, '--b'); % Adds a dashed line at Ts
xline(Te, '--r'); % Adds a dashed line at Te
xlabel('Time [s]');
ylabel('Diameter [m]');
yyaxis right;
hold on;
ylabel('Deformation Rate');
ax = gca; % Get current axis handle
ax.YColor = 'k'; % Set the color of the y-axis to black

legend('Experimental Data', 'Fitted Curve', 'Modeling Start','Modeling Stop');
info_str = sprintf("λ = %.4f [s], G'' = %.3f [Pa], Sample # : %.0f", L, G, sample_number);
title(info_str);

L_ms = L*1000

% % SAVE DATA (optional)
% dataMatrix = [time_table(:), data_m(:)];
% [filename, filepath] = uiputfile('*.csv', 'Save As');
% if ~(isequal(filename,0) || isequal(filepath,0))
% fullFilePath = fullfile(filepath, filename);
% writematrix(dataMatrix, fullFilePath);
% disp(['Data saved to: ', fullFilePath]);
% end
```

count_num_frames.m

```
function num_frames = count_num_frames (sample_number)

file_pattern = 'frame_*.tiff'; % Replace with the pattern of your file names
folder_path = sprintf('D:\\CaBER_data_SSD_2\\%d\\', sample_number);

% List files in the folder that match the specified pattern
files = dir(fullfile(folder_path, file_pattern));

% Count the number of frames
num_frames = length(files);

end
```

Boucle_v3.m

```
function [datas] = Boucle_v3(sample_number, start_frame, finish_frame, threshold, start_row,
end_row, measure_mode)
```

```
a = zeros(finish_frame - start_frame, 2);

for i = start_frame:finish_frame
filename = sprintf('D:\\CaBER_data_SSD_2\\%d\\frame_%06d.tiff', sample_number, i);
a(i - start_frame + 1, 1) = i;
thickness = thickness_measure_v2(filename, threshold, start_row, end_row, measure_mode);
a(i - start_frame + 1, 2) = min(thickness);
end

datas = a(:, 2);
end
```

thickness_measure_v2.m

```
function [pixels] = thickness_measure_v2(file, threshold, start_row, end_row, measure_mode)

% Load input image
input_img = imread(file);

% Get the size of the image
[height, width, ~] = size(input_img);

% Check if the image is wider than it is tall
if width > height
% Rotate the image clockwise by 90 degrees
img = imrotate(input_img, -90);
else
img = input_img;
end

% Convert to grayscale
gray = im2gray(img);
%imshow(gray);

% Apply edge detection
edges = edge_threshold(gray, threshold);
% subplot(1, 4, 1);
% imshow(gray);
% subplot(1, 4, 2);
% imshow(edges, []);

%left side
for y = 1:size(edges, 1)
i=1;
pixel_intensity = 0;
while pixel_intensity == 0
pixel_intensity = edges(y, i);
i = i + 1;
if i == size(edges, 2)
pixel_intensity = 1;
i = 0;
end
end
table_left(y) = i;
end

%right side
for y = 1:size(edges, 1)
i = size(edges, 2);
pixel_intensity = 0;
while pixel_intensity == 0
pixel_intensity = edges(y, i);
i = i - 1;
if i == 0
pixel_intensity = 1;
i = 0;
end
end
table_right(y) = i;
```

```
end

%size of the filament
thickness = 0;
for i = start_row:end_row
thickness(i - start_row + 1) = table_right(i) - table_left(i);
i = i + 1;
end

% measure_mode : mode = 1, min = 2
if measure_mode == 1
th = mode(thickness);
elseif measure_mode == 2
th = min(thickness);
end

pixels = thickness;
end
```

edge_threshold.m

```
function edges = edge_threshold(gray_image, threshold)

clear edge
edges = zeros(size(gray_image, 1), size(gray_image, 2));

for y = 1:size(gray_image, 1)
for x = 1:size(gray_image, 2)
if gray_image(y, x) <= threshold
edges(y, x) = 1;
end
x = x + 1;
end
y = y + 1;
end
end
```

APPENDIX IV

Supplementary information for Chapter 5

Solvent Evaporation Induces Stiffening in CaBER and Electrospinning of Volatile Polymer Solutions

Étienne J. Beaudoin[a], Ricardo J. Zednik[a] and Nicole R. Demarquette[a],

[a]Department of Mechanical Engineering, École de Technologie Supérieure,
1100 Notre-Dame West, Montreal, Quebec, Canada H3C 1K3

Paper submitted for publication, August 2025

This appendix reproduces the supplementary information associated with Chapter 5, which was submitted as supplementary material for the article *Solvent Evaporation Induces Stiffening in CaBER and Electrospinning of Volatile Polymer Solutions*, submitted to *Rheologica Acta* in August 2025. The material consists of additional figures and data that complement the results presented in the main text. Figure captions provide the necessary details for interpretation.

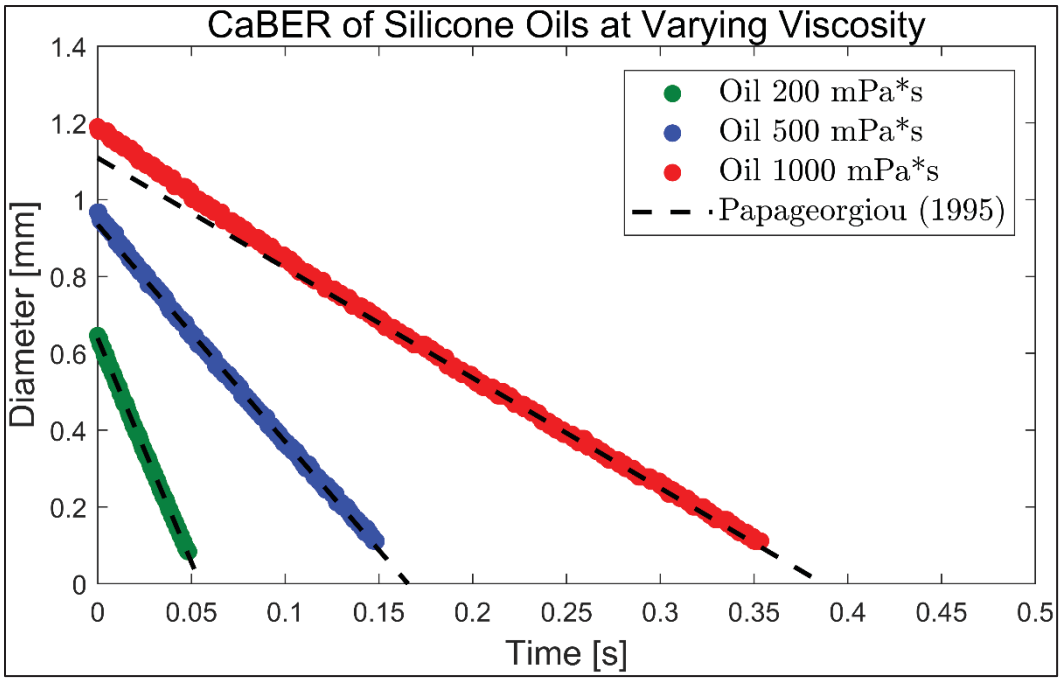

Figure-A IV-1 Calibration of the custom-build CaBER using Newtonian silicone oils. Three silicone oils exhibited progressively slower filament thinning with increasing viscosity. The dashed lines represent fits to Papageorgiou's analytical solution for the viscous-dominated regime [Papageorgiou, 1995], which predicts that the minimum filament diameter decreases linearly with time in the final approach to pinch-off. The resulting viscosities, obtained from these fits, are compiled in Table S1, together with the nominal grade values and the shear viscosities measured by rotational rheometry. This calibration serves as a validation of the performance and accuracy of the custom-built CaBER, demonstrating that the measured thinning dynamics agree with the theoretical viscocapillary scaling for Newtonian fluids. Silicone oils were kindly provided free of charge by Dow Chemical (Midland, MI, USA) under the trade name XIAMETER™ PMX-200. Three grades were used without further modification: 200 cSt, 350 cSt, and 1000 cSt.

Table-A IV-1 Viscosity of Newtonian silicone oils determined by CaBER compared with their nominal grade values and shear viscosities measured using a rotational rheometer

Oil grade [mPa*s]	**Shear viscosity [mPa*s]**	**CaBER shear equivalent [mPa*s]**
200	213	244 ± 32
500	537	514 ± 34
1000	1078	1034 ± 68

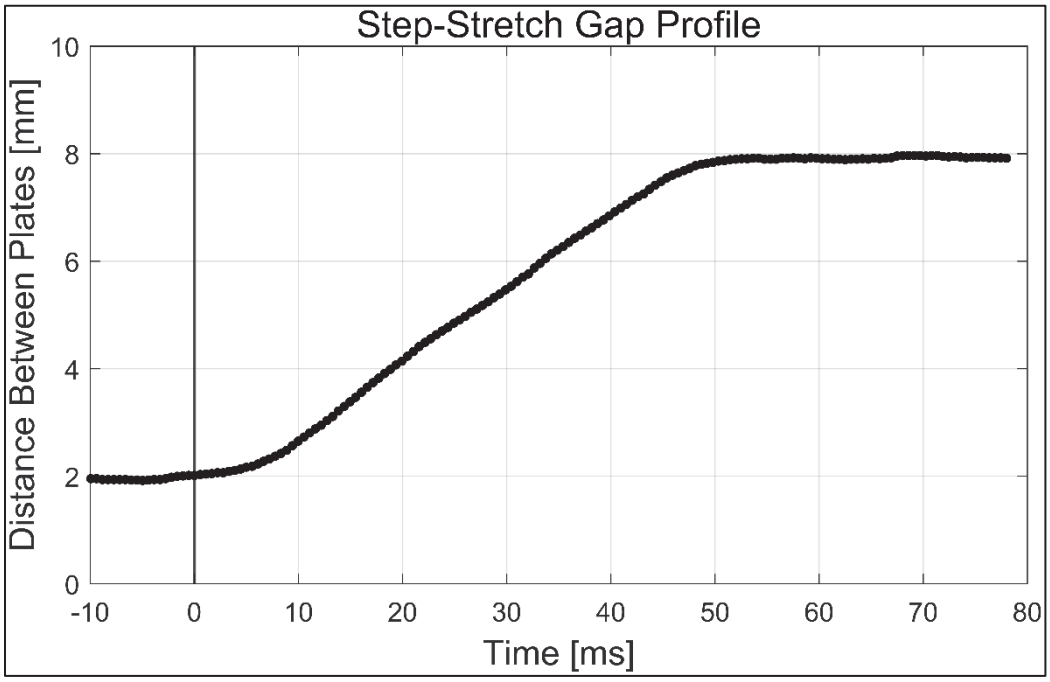

Figure-A IV-2 Example of a step-stretch profile performed with the custom-build CaBER. The motion profile was recorded without a liquid sample, and the plate separation was determined from image analysis. In this example, the initial gap was 2 mm, and the final gap was 8 mm, corresponding to a total displacement of 6 mm. The motion was driven by a stepper motor, which enables fine control of the displacement amplitude by adding or removing individual motor steps.

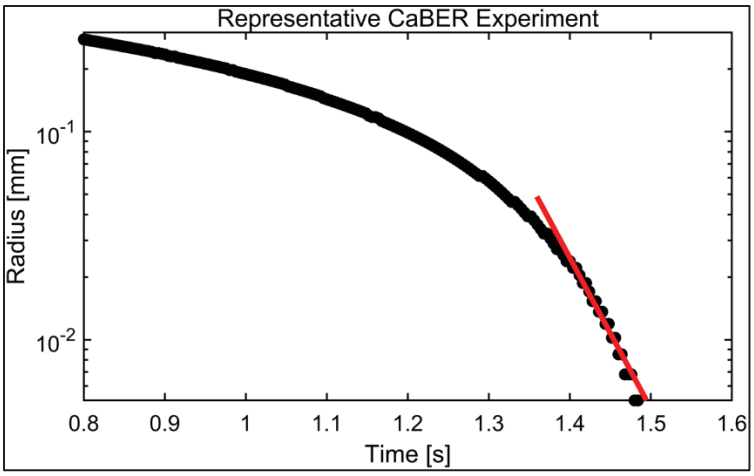

Figure-A IV-3 Representative CaBER measurement of a 22 wt% aqueous pullulan solution at 25 % relative solvent vapor pressure. The data correspond to the same measurement presented in Figure 3a of the main text, here shown on a semi-logarithmic scale. The red line represents the exponential fit used to extract the apparent relaxation time; the fit was performed from the end of the visco-capillary regime, which is more evident in the linear (non-logarithmic) plot.

Table-A IV-2 Raw relaxation time data corresponding to Figure 4 in the main text. The table lists all measured relaxation times obtained from CaBER experiments performed at 25 %, 50 %, 75 %, and 90 % relative humidity. For each condition, five plate displacement amplitudes (4.5, 5.0, 5.5, 6.0, and 6.5 mm) were tested, with two replicates per displacement. The average and standard deviation values plotted in Figure 4 were calculated from these measurements.

CaBER Gap [mm]	**Relaxation time [s], at 25% RH**	**Relaxation time [s], at 50% RH**	**Relaxation time [s], at 75% RH**	**Relaxation time [s], at 90% RH**
4.5	21.15	28.30	20.33	18.21
5	26.43	22.51	20.10	19.91
5.5	27.02	19.88	21.35	16.60
6	24.30	21.67	18.49	16.73
6.5	27.50	25.70	22.44	19.80

CaBER Gap [mm]	Relaxation time [s], at 25% RH	Relaxation time [s], at 50% RH	Relaxation time [s], at 75% RH	Relaxation time [s], at 90% RH
6.5	32.45	24.46	21.67	19.67
6	25.85	22.40	19.67	17.29
5.5	30.60	25.34	21.58	17.41
5	32.60	21.69	20.48	20.54
4.5	31.50	20.80	19.36	17.29
Average	27.94	23.28	20.55	18.35
STD	3.78	2.60	1.21	1.49

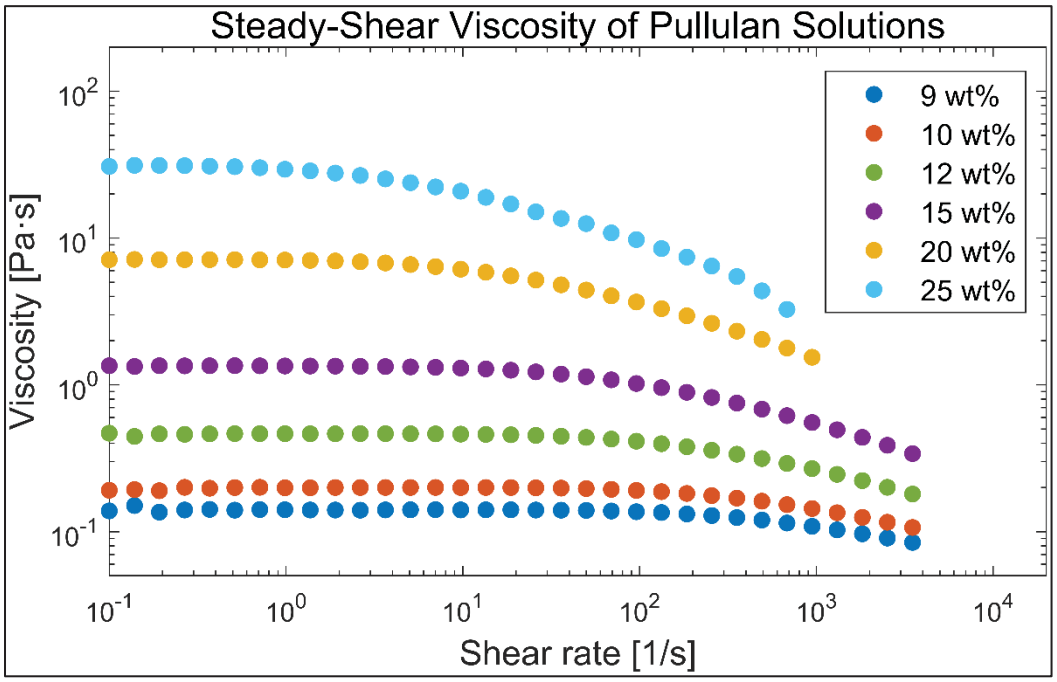

Figure-A IV-4 Steady-shear viscosity of aqueous pullulan solutions measured using a rotational rheometer. Each data series corresponds to a pullulan solution of the indicated concentration. The zero-shear viscosities used in Figure 5 of the main text were taken at a shear rate of 1 s^{-1}. For the 20 wt % and 25 wt % solutions, high-shear-rate data were truncated due to vortex formation in the measuring cup, which limited the reliability of the viscosity measurements.

APPENDIX V

Supplementary information for Chapter 6

Tuning Polymer Solution Elasticity for Electrospinning: Effects of Molecular Weight Distribution and Elastic Doping

Étienne J. Beaudoin[a], Ricardo J. Zednik[a] and Nicole R. Demarquette[a],

[a]Department of Mechanical Engineering, École de Technologie Supérieure,
1100 Notre-Dame West, Montreal, Quebec, Canada H3C 1K3

Paper submitted for publication, August 2025

This appendix reproduces the supplementary information associated with Chapter 6, which was submitted as supplementary material for the article *Tuning Polymer Solution Elasticity for Electrospinning: Effects of Molecular Weight Distribution and Elastic Doping*, submitted to *Rheologica Acta* in August 2025. The material consists of additional figures and data that complement the results presented in the main text. Figure captions provide the necessary details for interpretation.

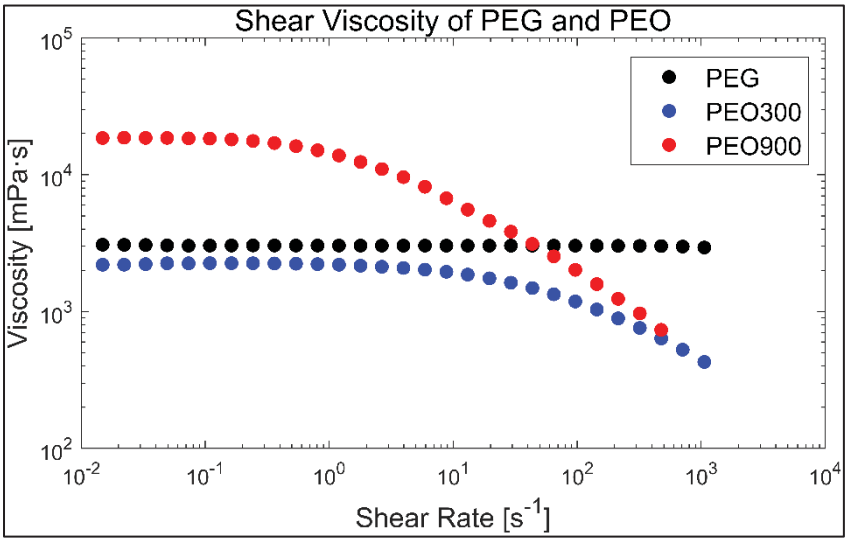

Figure-A V-1 Shear viscosity of PEG (40 wt%, 35,000 g/mol) and PEO (6 wt%, 300,000 g/mol and 900,000 g/mol) solutions as a function of shear rate; both PEO samples display pronounced shear, with stronger shear thinning behavior for the higher molecular weight sample, while PEG remains Newtonian across the measured range

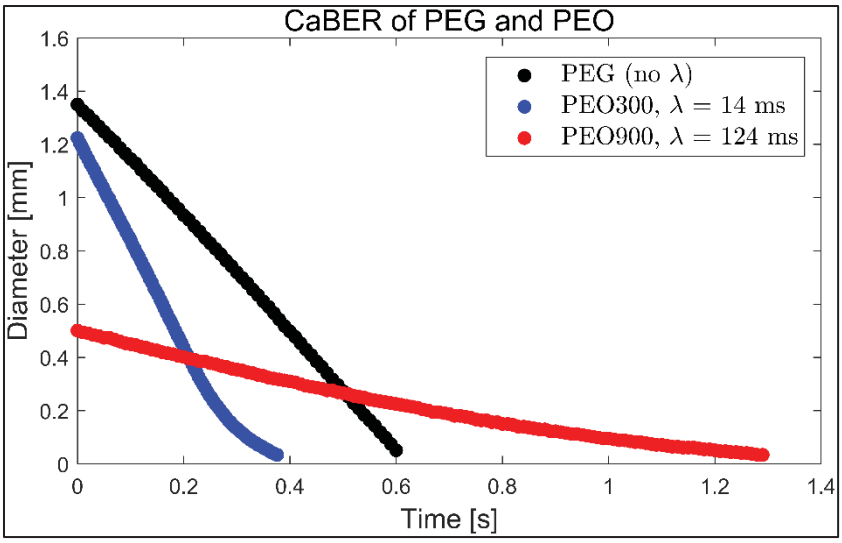

Figure-A V-2 Filament diameter evolution in CaBER for PEG (40 wt%, 30 000 g/mol), PEO (6 wt%, 300 000 g/mol), and PEO (6 wt%, 900 000 g/mol) solutions; for PEO 300k, the transition from Newtonian-like thinning to the elasto-capillary regime occurs at approximately 0.3 s; for PEO 900k, the curve is shifted by −1 s for clarity; only the latter stage of thinning is shown, but it remains clear that breakup occurs over a much longer time compared to the other samples

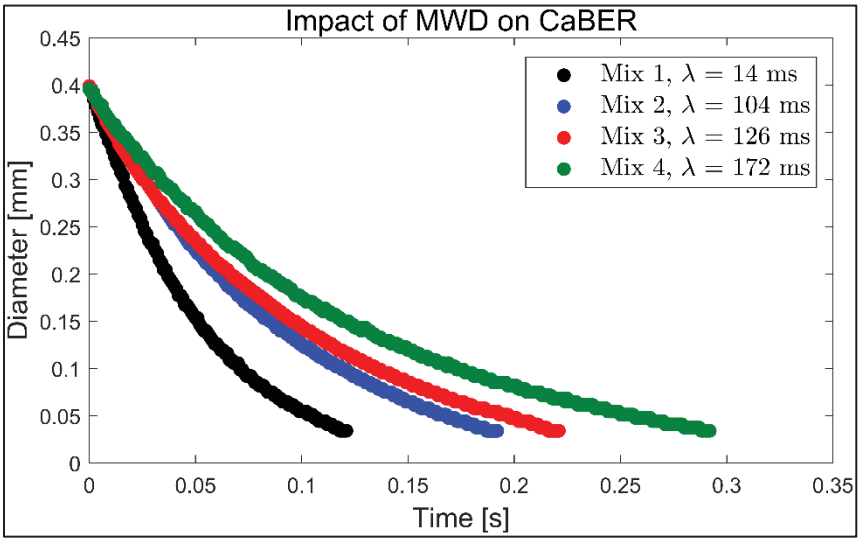

Figure-A V-3 CaBER thinning behavior of Mix1 to Mix4, with time zero defined at the start of the elasto-capillary regime for each sample; the extensional relaxation times extracted are indicated in the legend, showing a progressive increase in relaxation time as MWD increases

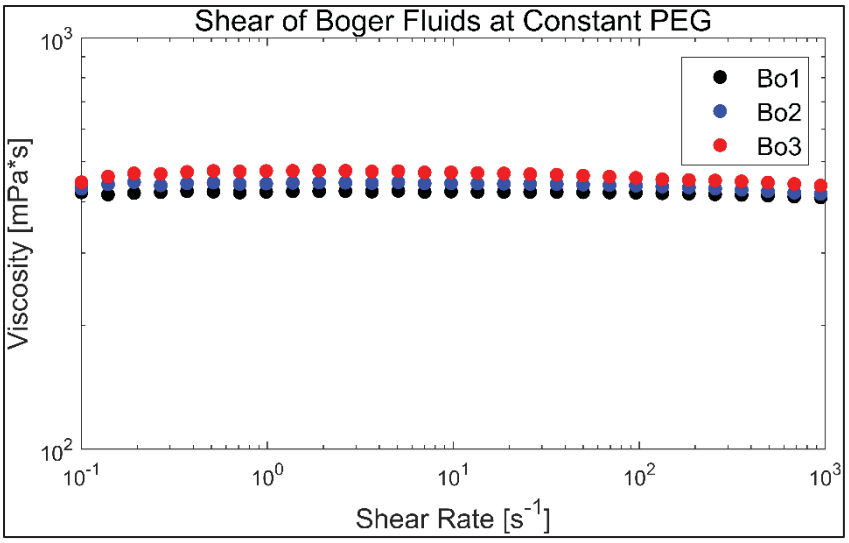

Figure-A V-4 Shear viscosity of Boger-fluids #1 to #3 as a function of shear rate; all formulations contain the same wt% PEG, and despite different PEO concentrations, the samples exhibit very similar shear viscosities overall, confirming that PEG concentration dominates the viscous behavior of these formulations

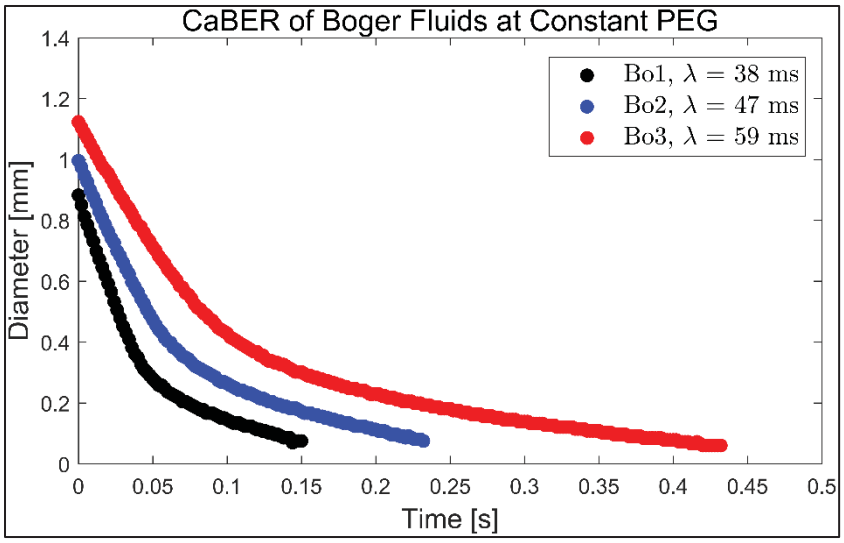

Figure-A V-5 CaBER filament thinning of Boger-fluids #1 to #3, with time zero defined as the moment immediately after the step stretch of the CaBER machine; relaxation times obtained by fitting the elasto-capillary regime are indicated in the legend; increasing the quantity of high-molecular-weight PEO leads to slower thinning and longer relaxation times

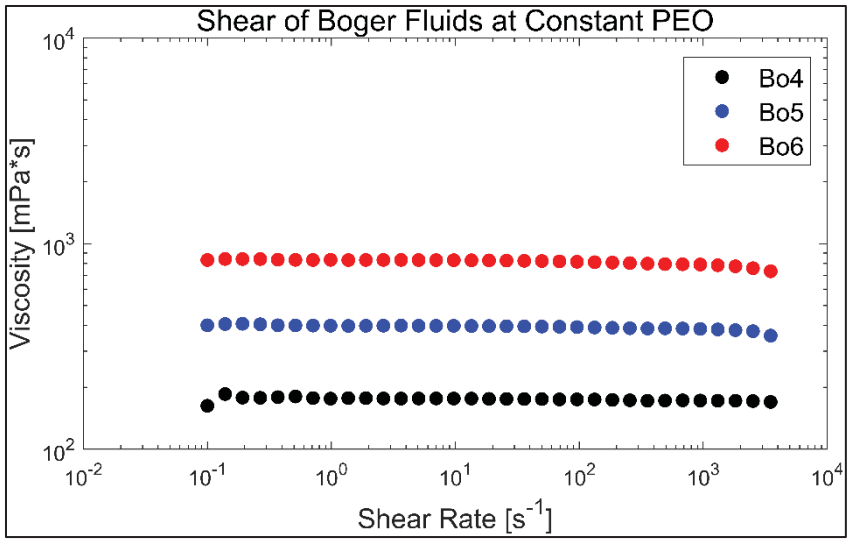

Figure-A V-6 Shear viscosity of Boger-fluids #4 to #6 as a function of shear rate; increasing PEG concentration results in higher shear viscosity, suggesting that background viscosity increases with PEG content

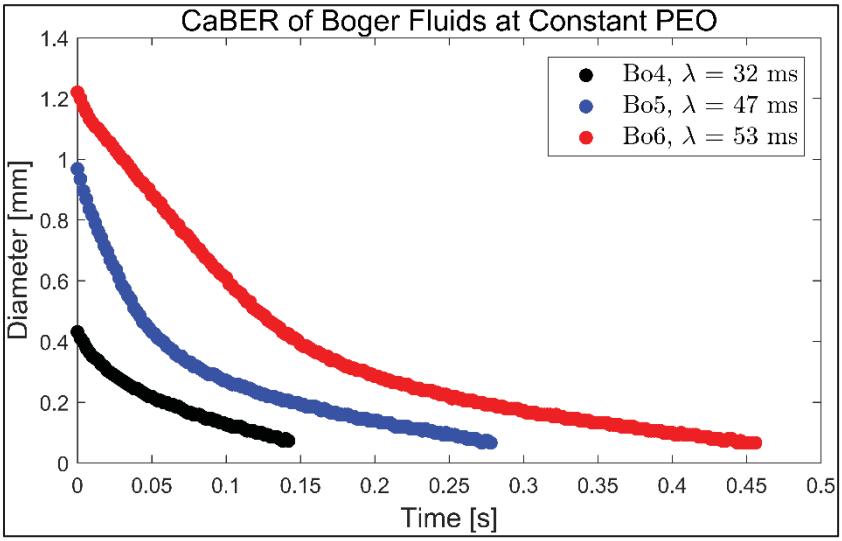

Figure-A V-7 CaBER filament thinning of Boger-fluids #4 to #6, with time zero defined immediately after the step stretch of the CaBER machine; relaxation times extracted from exponential fits are shown in the legend; increasing PEG content prolongs thinning and increases relaxation time, indicating that background viscosity affects the elastic response at constant PEO concentration; it is worth noting that PEG tested alone displayed no measurable elasticity in CaBER

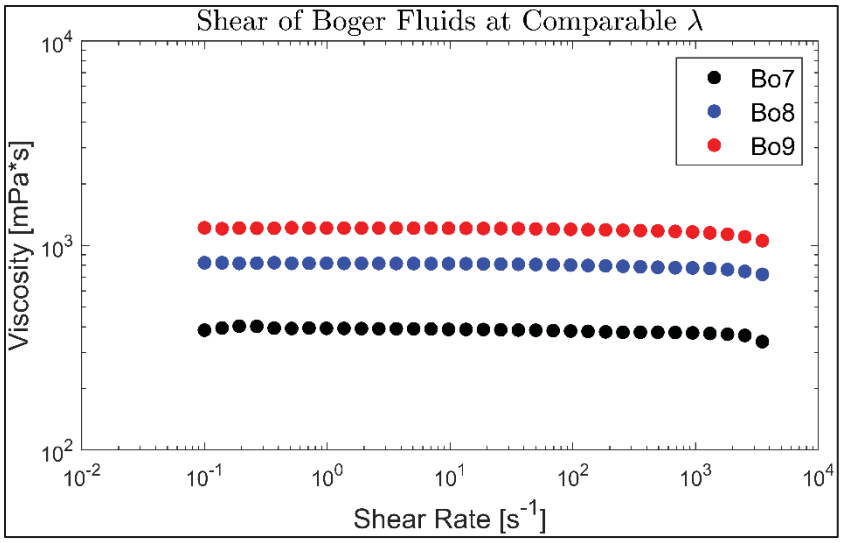

Figure-A V-8 Shear viscosity of Boger-fluids #7 to #9 as a function of shear rate; increasing PEG concentration and decreasing PEO concentration led to progressively higher viscosities, showing that PEG predominantly governs the viscosity of these formulations, even at relatively high PEO content

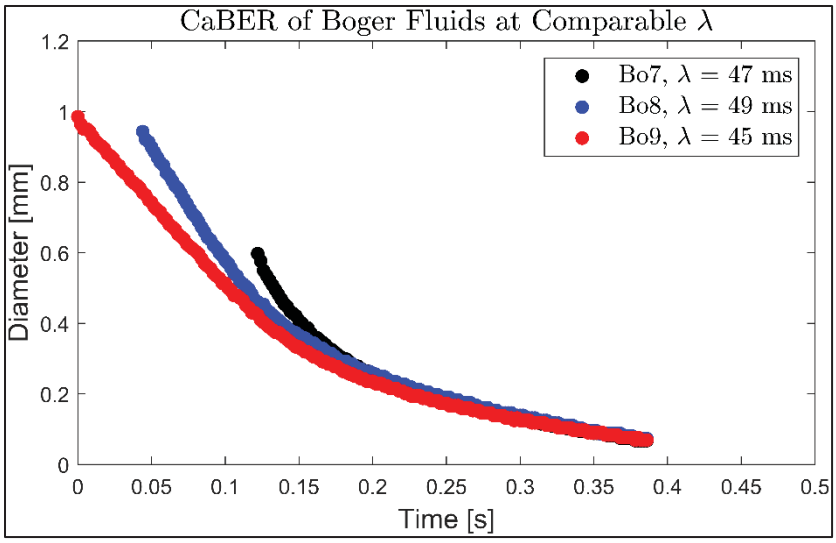

Figure-A V-9 CaBER filament thinning of Boger-fluids #7 to #9, with curves aligned so that the final measurable point coincides for all samples; despite different concentrations of both PEG and PEO, the curves converge to similar exponential decay regimes; relaxation times indicated in the legend confirm comparable extensional elasticity across all samples, demonstrating that increased background viscosity can compensate for reduced PEO concentration to yield the same elastic behavior

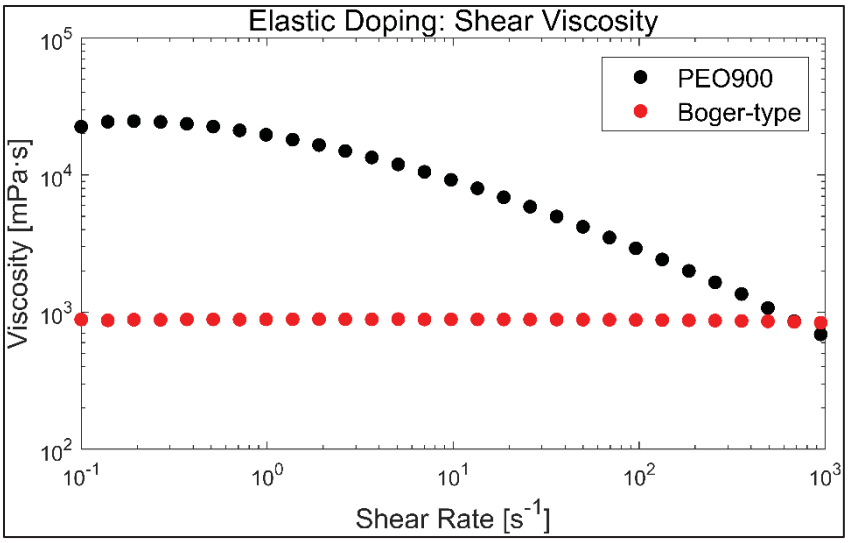

Figure-A V-10 Shear viscosity of the 6 wt% PEO solution (900,000 g/mol) and the PEG-PEO Boger-type blend as a function of shear rate; the PEO solution shows pronounced shear thinning, whereas the PEG–PEO blend remains nearly Newtonian over the measured range, with viscosity dominated by the PEG-rich matrix despite the small fraction of high–molecular-weight PEO

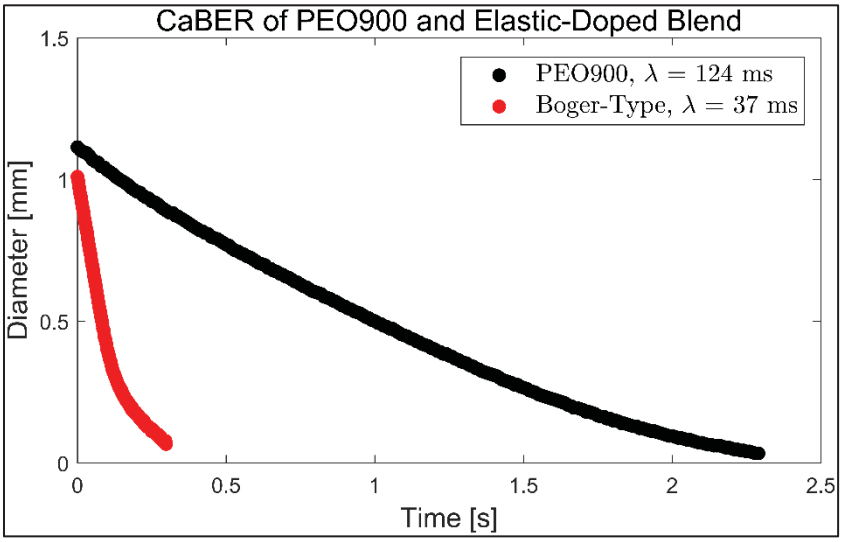

Figure-A V-11 CaBER filament thinning of the 6 wt% PEO solution (900,000 g/mol) and the PEG–PEO Boger-type blend, with time zero defined immediately after the step stretch of the CaBER machine; the PEO solution displays a long-lived elasto-capillary regime, indicative of a high extensional relaxation time; the PEG–PEO blend exhibits a shorter relaxation time but still maintains elastic thinning behavior, enabled by the small fraction of high–molecular-weight PEO; relaxation times are indicated in the legend

APPENDIX VI

VITA

EDUCATION

- *Doctor of Philosophy (Ph. D)* – École de Technologie Supérieure (ÉTS). Supervisor: Prof. Nicole R. Demarquette, Co-supervisor: Prof. Ricardo Zednik. From September 2021 to November 2025, Montréal, QC – Canada.
- *Master of Applied Science (M.A.Sc.)* in Mechanical engineering (with thesis, accelerated fast-track) – École de Technologie Supérieure (ÉTS). Supervisor: Prof. Nicole R. Demarquette, Co-supervisor: Prof. Ricardo Zednik. From January 2021 to September 2021, Montréal, QC – Canada.
- *Bachelor of Engineering (B.Eng.)* in Mechanical Engineering – École de Technologie Supérieure (ÉTS). From September 2015 to December 2020, Montréal, QC – Canada.
- *Diploma of College Studies (DEC)* in Engineering Physics Technology – Cégep Antré-Laurendeau. From September 2012 to May 2015, Lasalle, QC – Canada.

AWARDS AND SCHOLARSHIP

- Graduate Study Scholarships (Master's and Doctorate) – École de technologie supérieure (ÉTS), Montréal, Canada, 2021–2025.
- Conference Travel Award – Society of Plastics Engineers (SPE), Montréal, Canada, 2025. CAD 1,000.
- Conference Travel Award (International Mobility Grant) – École de technologie supérieure (ÉTS), Montréal, Canada, 2025. CAD 1,000.
- Conference Travel Award (Event Participation Grant) – Society of Plastics Engineers (SPE), Montréal, Canada, 2024. CAD 500.

- Conference Travel Award (International Mobility Grant) – École de technologie supérieure (ÉTS), Montréal, Canada, 2024. CAD 500.
- Conference Travel Award (Research Outreach Grant) – École de technologie supérieure (ÉTS), Montréal, Canada, 2024. CAD 1,000.
- Youth Scholarship (Bourses jeunesse) – Caisse Desjardins, Montréal, Canada, 2024. CAD 1,500.
- Photo Contest – Jury Prize (*La preuve par l'image*) – Association francophone pour le savoir (ACFAS), Biodôme de Montréal, 2024. Sponsored by NSERC. CAD 2,000.
- Photo Contest – Research Activity Category Winner – École de technologie supérieure (ÉTS), Montréal, Canada, 2023. CAD 100.
- Graduate Student Involvement Award (Bourse d'implication aux cycles supérieurs) – École de technologie supérieure (ÉTS), Montréal, Canada, 2023. CAD 2,500.
- First Place Winner – Three-Minute Thesis Competition (Ma thèse en 180 secondes) – Society of Plastics Engineers (SPE), 2021. CAD 500.
- "Une bourse pas comme les autres, 2e dose" Scholarship – Caisse Desjardins, November 2020. CAD 1,500.

JOURNAL PUBLICATIONS

- Beaudoin, E. J., Zednik, R. J., & Demarquette, N. R. Solvent evaporation drives strain hardening in CaBER and electrospinning of volatile polymer solutions. *Rheologica Acta* (submitted, under review, August 2025).
- Beaudoin, E. J., Zednik, R. J., & Demarquette, N. R. Tuning polymer solution elasticity for electrospinning: Effects of molecular weight distribution and elastic doping. *Rheologica Acta* (submitted, under review, August 2025).
- Beaudoin, E. J., Kubaski, M. M., Samara, M., Zednik, R. J., & Demarquette, N. R. (2022). Scaled-up multi-needle electrospinning process using parallel plate auxiliary electrodes. *Nanomaterials*, 12(8). https://doi.org/10.3390/nano12081356

CONFERENCE PRESENTATIONS

- Beaudoin, E. J., Zednik, R. J., & Demarquette, N. R. *Impact of Polydispersity on Polymer Solutions and Electrospun Nanofibers.* Oral presentation at CSME–CFDSC–CSR 2025, Canadian Society for Mechanical Engineering International Congress / 32nd Annual CFD Society of Canada Conference / Canadian Society of Rheology Symposium. Canada, 2025.
- Beaudoin, E. J., Zednik, R. J., & Demarquette, N. R. *Solvent Volatility in CaBER.* Oral presentation at AERC 2025 (Annual European Rheology Conference). Lyon, France, 2025.
- Beaudoin, E. J., Kubaski, M. M., Zednik, R. J., & Demarquette, N. R. *Exploring Fluids' Behavior: Lab-Scale Capillary Breakup Extensional Rheometer and Its Applications in Polymer Processing.* Keynote presentation at PPS 2024 (Polymer Processing Society Conference). Cartagena, Colombia, 2024.
- Beaudoin, E. J., Kubaski, M. M., Zednik, R. J., & Demarquette, N. R. *Exploring Fluids' Behavior: Lab-Scale Capillary Breakup Extensional Rheometer and Its Applications in Polymer Processing.* Poster presented at AERC 2024 (Annual European Rheology Conference). Leeds, UK, 2024.
- Beaudoin, E. J., Kubaski, M. M., Samara, M., Zednik, R. J., & Demarquette, N. R. *Scaled-Up Multi-Needle Electrospinning Process Using Parallel Plate Auxiliary Electrodes.* Poster presented at CREPEC Annual Colloquium. Montréal, Canada, 2022.
- Beaudoin, E. J., Kubaski, M. M., Samara, M., Zednik, R. J., & Demarquette, N. R. *Multi-Needle Electrospinning: Towards the Production of Large Nonwoven Membranes.* Oral presentation at PPS 36th Conference. Montréal, Canada, 2021.

LIST OF BIBLIOGRAPHICAL REFERENCES

Ahmadi Bonakdar, M., & Rodrigue, D. (2024). Electrospinning: Processes, Structures, and Materials. *Macromol, 4*(1), 58-103. doi: 10.3390/macromol4010004

Al-Abduljabbar, A., & Farooq, I. (2022). Electrospun Polymer Nanofibers: Processing, Properties, and Applications. *Polymers (Basel), 15*(1). doi: 10.3390/polym15010065. Repéré à https://www.ncbi.nlm.nih.gov/pubmed/36616414

Albrecht, W., Fuchs, H., & Kittelmann, W. (2003). *Nonwoven Fabrics: Raw Materials, Manufacture, Applications, Characteristics, Testing Processes*. doi: 10.1002/3527603344

Alfaro De Prá, M. A., Ribeiro-do-Valle, R. M., Maraschin, M., & Veleirinho, B. (2017). Effect of collector design on the morphological properties of polycaprolactone electrospun fibers. *Materials Letters, 193*, 154-157. doi: 10.1016/j.matlet.2017.01.102

Amarouchene, Y., Bonn, D., Meunier, J., & Kellay, H. (2001). Inhibition of the finite-time singularity during droplet fission of a polymeric fluid. *Phys Rev Lett, 86*(16), 3558-3561. doi: 10.1103/PhysRevLett.86.3558. Repéré à https://www.ncbi.nlm.nih.gov/pubmed/11328022

Anna, S. L., & McKinley, G. H. (2001). Elasto-capillary thinning and breakup of model elastic liquids. *Journal of Rheology, 45*(1), 115-138. doi: 10.1122/1.1332389

Ardekani, A. M., Sharma, V., & McKinley, G. H. (2010). Dynamics of bead formation, filament thinning and breakup in weakly viscoelastic jets. *Journal of Fluid Mechanics, 665*, 46-56. doi: 10.1017/s0022112010004738

Basu, S., Agrawal, A. K., & Jassal, M. (2011). Concept of minimum electrospinning voltage in electrospinning of polyacrylonitrile N,N-dimethylformamide system. *Journal of Applied Polymer Science, 122*(2), 856-866. doi: 10.1002/app.34083

Basu, S., Jassal, M., & Agrawal, A. K. (2013). Effect of bipolar configuration on morphology of electrospun webs. *Journal of the Textile Institute, 104*(10), 1071-1079. doi: 10.1080/00405000.2013.774133

Baumgarten, P. K. (1971). Electrostatic Spinning of Acrylic Microfibers. *Journal of Colloid and Interface Science, 36*(1), 71-79. doi: 10.1016/0021-9797(71)90241-4

Bazilevsky, A. V., Entov, V. M., Lerner, M. M., & Rozhkov, A. N. (1996). Failure of Polymer Solution Filaments. *Polymer Science, Series A, 39*(3), 316-324.

Bazilevsky, A. V., Entov, V. M., & Rozhkov, A. N. (1990). Liquid Filament Microrheometer and Some of Its Applications. Dans *Third European Rheology Conference and Golden Jubilee Meeting of the British Society of Rheology* (pp. 41-43). doi: 10.1007/978-94-009-0781-2_21

Beaudoin, E. J., Kubaski, M. M., Samara, M., Zednik, R. J., & Demarquette, N. R. (2022). Scaled-Up Multi-Needle Electrospinning Process Using Parallel Plate Auxiliary Electrodes. *Nanomaterials (Basel), 12*(8). doi: 10.3390/nano12081356. Repéré à https://www.ncbi.nlm.nih.gov/pubmed/35458064

Cai, Y., & Gevelber, M. (2013). The effect of relative humidity and evaporation rate on electrospinning: fiber diameter and measurement for control implications. *Journal of Materials Science, 48*(22), 7812-7826. doi: 10.1007/s10853-013-7544-x

Calabrese, V., Shen, A. Q., & Haward, S. J. (2025). Effects of Polydispersity and Concentration on Elastocapillary Thinning of Dilute Polymer Solutions. *Physical Review X, 15*(2). doi: 10.1103/PhysRevX.15.021025

Campo-Deaño, L., & Clasen, C. (2010). The slow retraction method (SRM) for the determination of ultra-short relaxation times in capillary breakup extensional rheometry experiments. *Journal of Non-Newtonian Fluid Mechanics, 165*(23-24), 1688-1699. doi: 10.1016/j.jnnfm.2010.09.007

Clasen, C., Eggers, J., Fontelos, M. A., Li, J. I. E., & McKinley, G. H. (2006). The beads-on-string structure of viscoelastic threads. *Journal of Fluid Mechanics, 556*, 283-308. doi: 10.1017/s0022112006009633

Clasen, C., Plog, J. P., Kulicke, W.-M., Owens, M., Macosko, C., Scriven, L. E., . . . McKinley, G. H. (2006). How dilute are dilute solutions in extensional flows? *Journal of Rheology, 50*, 849-881. doi: https://doi.org/10.1122/1.2357595

Cogswell, F. N. (1968). Rheology of polymer melts under tension *Plastics & Polymers, 36*(122), 109-111.

Cogswell, F. N. (1981). *Polymer Melt Rheology. A Guide for Industrial Practice*. Woodhead.

Colby, R. H. (2023). Fiber spinning from polymer solutions. *Journal of Rheology, 67*(6), 1251-1255. doi: 10.1122/8.0000726

Collett, C., Ardron, A., Bauer, U., Chapman, G., Chaudan, E., Hallmark, B., . . . Wilson, D. I. (2015). A portable extensional rheometer for measuring the viscoelasticity of pitcher plant and other sticky liquids in the field. *Plant Methods, 11*, 16. doi: 10.1186/s13007-015-0059-5. Repéré à https://www.ncbi.nlm.nih.gov/pubmed/25798183

Colman P. Carroll, Y. L. J. (2006). Electrospinning of viscoelastic Boger fluids: Modeling and experiments. *Physics of Fluids, 18*(053102). doi: 10.1063/1.2200152

Crank, J. (1975). *The Mathematics of Diffusion* (2nd éd.). Oxford University Press.

De Vrieze, S., Van Camp, T., Nelvig, A., Hagström, B., Westbroek, P., & De Clerck, K. (2009). The effect of temperature and humidity on electrospinning. *Journal of Materials Science, 44*(5), 1357-1362. doi: 10.1007/s10853-008-3010-6

Dealy, J. M., Read, D. J., & Larson, R. G. (2018). *Structure and Rheology of Molten Polymers*. doi: https://doi.org/10.3139/9781569906125

Deshawar, D., Gupta, K., & Chokshi, P. (2020). Electrospinning of polymer solutions: An analysis of instability in a thinning jet with solvent evaporation. *Polymer, 202*. doi: 10.1016/j.polymer.2020.122656

Dinic, J., Biagioli, M., & Sharma, V. (2017). Pinch-off dynamics and extensional relaxation times of intrinsically semi-dilute polymer solutions characterized by dripping-onto-substrate rheometry. *Journal of Polymer Science Part B: Polymer Physics, 55*(22), 1692-1704. doi: 10.1002/polb.24388

Dinic, J., Jimenez, L. N., & Sharma, V. (2017). Pinch-off dynamics and dripping-onto-substrate (DoS) rheometry of complex fluids. *Lab Chip, 17*(3), 460-473. doi: 10.1039/c6lc01155a. Repéré à https://www.ncbi.nlm.nih.gov/pubmed/28001165

Dinic, J., Zhang, Y., Jimenez, L. N., & Sharma, V. (2015). Extensional Relaxation Times of Dilute, Aqueous Polymer Solutions. *ACS Macro Lett, 4*(7), 804-808. doi: 10.1021/acsmacrolett.5b00393. Repéré à https://www.ncbi.nlm.nih.gov/pubmed/35596480

Doi, M., & Edwards, S. F. (1986). *The Theory of Polymer Dynamics*. Oxford Science Publications.

Eggers, J. (1997). Nonlinear dynamics and breakup of free-surface flows. *Reviews of Modern Physics, 69*(3), 865-930. doi: https://doi.org/10.1103/RevModPhys.69.865

Entov, V. M. (1986). The Effects of Elastic Deformations in the Flow of Polymer Solution. *Heat Transfer, Soviet Research, 18*.

Entov, V. M., & Hinch, E. J. (1997). Effect of a spectrum of relaxation times on the capillary thinning of a filament of elastic liquid. *Journal of Non-Newtonian Fluid Mechanics, 72*(1), 31-53. doi: 10.1016/s0377-0257(97)00022-0

Entov, V. M., & Shmaryan, L. E. (1997). Numerical modeling of the capillary breakup of jets of polymeric liquids. *Fluid Dynamics, 32*(5), 696-703.

Entov, V. M., & Yarin, A. L. (1984). Influence of elastic stresses on the capillary breakup of jets of dilute polymer solutions. *Fluid Dynamics, 19*, 21-29. doi: https://doi.org/10.1007/BF01090901

Ewaldz, E., Randrup, J., & Brettmann, B. (2022). Solvent Effects on the Elasticity of Electrospinnable Polymer Solutions. *ACS Polym Au, 2*(2), 108-117. doi: 10.1021/acspolymersau.1c00041. Repéré à https://www.ncbi.nlm.nih.gov/pubmed/36855340

Fong, H., Chun, I., & Reneker, D. H. (1999). Beaded nanofibers formed during electrospinning. *Polymer, 40*(16), 4585-4592. doi: https://doi.org/10.1016/S0032-3861(99)00068-3

Formhals, A. (1934). *Brevet USA*.

Galindo-Rosales, F. J., Alves, M. A., & Oliveira, M. S. N. (2012). Microdevices for extensional rheometry of low viscosity elastic liquids: a review. *Microfluidics and Nanofluidics, 14*(1-2), 1-19. doi: 10.1007/s10404-012-1028-1

Gennes, P.-G. d. (1979). *Scaling Concepts in Polymer Physics*. Cornell University Press.

Gennes, P.-G. d. (1990). *Introduction to Polymer Dynamics*. Cambridge University Press. doi: https://doi.org/10.1017/CBO9780511569463

Gennes, P.-G. d., Brochard-Wyart, F., & Quéré, D. (2004). *Capillarity and Wetting Phenomena*. Springer Science & Business Media.

Graessley, W. W. (1980). Polymer chain dimensions and the dependence of viscoelastic properties on concentration, molecular weight and solvent power. *Polymer, 21*(3), 258-262. doi: https://doi.org/10.1016/0032-3861(80)90266-9

Guarino, V., Cirillo, V., Taddei, P., Alvarez-Perez, M. A., & Ambrosio, L. (2011). Tuning size scale and crystallinity of PCL electrospun fibres via solvent permittivity to address hMSC response. *Macromol Biosci, 11*(12), 1694-1705. doi: 10.1002/mabi.201100204. Repéré à https://www.ncbi.nlm.nih.gov/pubmed/22052674

Gupta, D., Jassal, M., & Agrawal, A. K. (2015). Electrospinning of Poly(vinyl alcohol)-Based Boger Fluids To Understand the Role of Elasticity on Morphology of Nanofibers. *Industrial & Engineering Chemistry Research, 54*(5), 1547-1554. doi: 10.1021/ie504141c

H.A. Barnes, J. F. H. a. K. W. (1993). *An Introduction to Rheology*. Elsevier Science Publishers B.V.

Hallmark, B., Bryan, M., Bosson, E., Butler, S., Hoier, T., Magens, O., . . . Wilson, D. I. (2016). A portable and affordable extensional rheometer for field testing. *Measurement Science and Technology, 27*(12). doi: 10.1088/0957-0233/27/12/125302

Herbert Leaderman; Robert G. Smith; L. C. Williams. (1959). Rheology of polyisobutylene. III. Elastic Recovery,Non-Newtonian Flow, and Molecular Weight Distribution. *Journal of Polymer Science, XXXVI*, 233-257.

Huang, Q. (2022). When Polymer Chains Are Highly Aligned: A Perspective on Extensional Rheology. *Macromolecules, 55*(3), 715-727. doi: 10.1021/acs.macromol.1c02262. Repéré à https://doi.org/10.1021/acs.macromol.1c02262

Huang, Z.-M., Zhang, Y. Z., Kotaki, M., & Ramakrishna, S. (2003). A review on polymer nanofibers by electrospinning and their applications in nanocomposites. *Composites Science and Technology, 63*(15), 2223-2253. doi: 10.1016/s0266-3538(03)00178-7

Incropera, DeWitt, Bergman, & Lavine. (2006). *Fundamentals of Heat and Mass Transfer* (6th éd.). Wiley.

J.M. Deitzel, J. K., D. Harris, N.C. Beck Tan. (2000). The effect of processing variables on the morphology of electrospun nanofibers and textiles. *Polymer,* (42), 261-272. doi: https://doi.org/10.1016/S0032-3861(00)00250-0

Jayesh Doshi, & Reneker, D. H. (1995). Electrospinning Process and Applications of Electrospun Fibers. *Journal of Electrostatics, 35*(2-3), 151-160. doi: https://doi.org/10.1016/0304-3886(95)00041-8

John M. Dealy, K. F. W. (1990). *Melt Rheology and Its Role in Plastics Processing Theory and Applications* Springer, Boston, MA.

Joy, N., Anuraj, R., Viravalli, A., Dixit, H. N., & Samavedi, S. (2021). Coupling between voltage and tip-to-collector distance in polymer electrospinning: Insights from analysis of regimes, transitions and cone/jet features. *Chemical Engineering Science, 230*. doi: 10.1016/j.ces.2020.116200

Keshavarz, B., Sharma, V., Houze, E. C., Koerner, M. R., Moore, J. R., Cotts, P. M., . . . McKinley, G. H. (2015). Studying the effects of elongational properties on atomization of weakly viscoelastic solutions using Rayleigh Ohnesorge Jetting Extensional Rheometry (ROJER). *Journal of Non-Newtonian Fluid Mechanics, 222*, 171-189. doi: 10.1016/j.jnnfm.2014.11.004

Kim, G., Cho, Y.-S., & Kim, W. D. (2006). Stability analysis for multi-jets electrospinning process modified with a cylindrical electrode. *European Polymer Journal, 42*(9), 2031-2038. doi: 10.1016/j.eurpolymj.2006.01.026

Kim, I. G., Lee, J.-H., Unnithan, A. R., Park, C.-H., & Kim, C. S. (2015). A comprehensive electric field analysis of cylinder-type multi-nozzle electrospinning system for mass production of nanofibers. *Journal of Industrial and Engineering Chemistry, 31*, 251-256. doi: 10.1016/j.jiec.2015.06.033

Kuru, F. (2025). Comparative Study on the Impact of Collector Geometry on Electrospun Nanofiber Morphology and Porosity Using Multiple Polymers. *Usak University Journal of Engineering Sciences, 8*(1), 26-37. doi: 10.47137/uujes.1694511

L. Larrondo, & Manley, R. S. J. (1981a). Electrostatic fiber spinning from Polymer Melts. I. Experimental Observations on Fiber Formation and Properties. *Journal of Polymer Science: Polymer Physics Edition, 19*(6), 909-920. doi: https://doi.org/10.1002/pol.1981.180190601

L. Larrondo, & Manley, R. S. J. (1981b). Electrostatic fiber spinning from Polymer Melts. II. Examination of the Flow Field in an Electrically Driven Jet. *Journal of Polymer Science: Polymer Physics Edition, 19*(6), 921-932. doi: https://doi.org/10.1002/pol.1981.180190602

L. Larrondo, & Manley, R. S. J. (1981c). Electrostatic fiber spinning from Polymer Melts. III. Electrostatic Deformation of a Pendant Drop of Polymer Melt. *Journal of Polymer Science: Polymer Physics Edition, 19*(6), 933-940. doi: https://doi.org/10.1002/pol.1981.180190603

Li, D., & Xia, Y. (2004). Electrospinning of Nanofibers: Reinventing the Wheel? *Advanced Materials, 16*(14), 1151-1170. doi: 10.1002/adma.200400719

Li, Y., Zhu, J., Cheng, H., Li, G., Cho, H., Jiang, M., . . . Zhang, X. (2021). Developments of Advanced Electrospinning Techniques: A Critical Review. *Advanced Materials Technologies, 6*(11). doi: 10.1002/admt.202100410

Lindner, A., & Wagner, C. (2009). Viscoelastic surface instabilities. *Comptes Rendus Physique, 10*(8), 712-727. doi: 10.1016/j.crhy.2009.10.017

Liu, Y., & Guo, L. (2013). Homogeneous field intensity control during multi-needle electrospinning via finite element analysis and simulation. *J Nanosci Nanotechnol, 13*(2), 843-847. doi: 10.1166/jnn.2013.6017. Repéré à https://www.ncbi.nlm.nih.gov/pubmed/23646527

Mailley, D., Hébraud, A., & Schlatter, G. (2021). A Review on the Impact of Humidity during Electrospinning: From the Nanofiber Structure Engineering to the Applications. *Macromolecular Materials and Engineering, 306*(7). doi: 10.1002/mame.202100115

Marshall, K. A. (2017). *Extensional Characterization of Weakly-Viscoelastic Fluids: Methods & Applications* (M.S. thesis, Oregon State University, Corvallis, OR).

Marshall, K. A., Liedtke, A. M., Todt, A. H., & Walker, T. W. (2017). Extensional rheometry with a handheld mobile device. *Experiments in Fluids, 58*(6). doi: 10.1007/s00348-017-2351-9

Matabola, K. P., & Moutloali, R. M. (2013). The influence of electrospinning parameters on the morphology and diameter of poly(vinyledene fluoride) nanofibers- effect of sodium chloride. *Journal of Materials Science, 48*(16), 5475-5482. doi: 10.1007/s10853-013-7341-6

Mathues, W., Formenti, S., McIlroy, C., Harlen, O. G., & Clasen, C. (2018). CaBER vs ROJER—Different time scales for the thinning of a weakly elastic jet. *Journal of Rheology, 62*(5), 1135-1153. doi: 10.1122/1.5021834

McCrum, N. G., Buckley, C. P., & Bucknall, C. B. (1988). *Principles of Polymer Engineering* Oxford Science Publications.

McKinley, G. H. (2005). Visco-Elasto-Capillary Thinning and Break-Up of Complex Fluids. *Annual Rheology Reviews*. doi: http://hdl.handle.net/1721.1/18085

McKinley, G. H., & Tripathi, A. (2000). How to extract the Newtonian viscosity from capillary breakup measurements in a filament rheometer. *Journal of Rheology, 44*(3), 653-670. doi: 10.1122/1.551105

Meissner, J. (1972). Development of a Universal Extensional Rheometer for the Uniaxial Extension of Polymer Melts. *Transactions of the Society of Rheology, 16*(3), 405-420. doi: 10.1122/1.549258

Meissner, J. (1984). Polymer melt rheology - a challenge for the polymer scientist and engineer. *Pure and Applied Chemistry, 56*(3), 369-384. doi: doi:10.1351/pac198456030369. Repéré à https://doi.org/10.1351/pac198456030369

Mieras, H. J. M. A., & Van Rijn, C. F. H. (1969). Influence of molecular weight distribution on the elasticity and processing properties of polypropylene melts. *Journal of Applied Polymer Science, 13*(2), 309-322. doi: https://doi.org/10.1002/app.1969.070130204

Miller, E., Clasen, C., & Rothstein, J. P. (2009). The effect of step-stretch parameters on capillary breakup extensional rheology (CaBER) measurements. *Rheologica Acta, 48*(6), 625-639. doi: 10.1007/s00397-009-0357-9

Minoshima, W., White, J. L., & Spruiell, J. E. (1980). Experimental Investigation of the Influence of Molecular Weight Distribution of the Rheological Properties of Polypropylene Melts. *Polymer Engineering and Science, 20*(17), 1166 - 1176. doi: https://doi.org/10.1002/pen.760201710

Moon, J. D., Webber, T. R., Brown, D. R., Richardson, P. M., Casey, T. M., Segalman, R. A., . . . Han, S. (2024). Nanoscale water-polymer interactions tune macroscopic diffusivity of water in aqueous poly(ethylene oxide) solutions. *Chem Sci, 15*(7), 2495-2508. doi: 10.1039/d3sc05377f. Repéré à https://www.ncbi.nlm.nih.gov/pubmed/38362435

Ng, H. C. H., & Poole, R. J. (2021). Highlighting the need for high-speed imaging in capillary breakup extensional rheometry. *Measurement Science and Technology, 32*(9). doi: 10.1088/1361-6501/abeea8

Ohring, M. (2002). Chapter 3 - Thin-Film Evaporation Processes. Dans M. Ohring (Éd.), *Materials Science of Thin Films (Second Edition)* (pp. 95-144). Academic Press. doi: https://doi.org/10.1016/B978-012524975-1/50006-9

Okuzono, T., Ozawa, K., & Doi, M. (2006). Simple model of skin formation caused by solvent evaporation in polymer solutions. *Phys Rev Lett, 97*(13), 136103. doi: 10.1103/PhysRevLett.97.136103. Repéré à https://www.ncbi.nlm.nih.gov/pubmed/17026050

Omer, S., Forgach, L., Zelko, R., & Sebe, I. (2021). Scale-up of Electrospinning: Market Overview of Products and Devices for Pharmaceutical and Biomedical Purposes. *Pharmaceutics, 13*(2). doi: 10.3390/pharmaceutics13020286. Repéré à https://www.ncbi.nlm.nih.gov/pubmed/33671624

Papageorgiou, D. T. (1995). On the breakup of viscous liquid threads. *Physics of Fluids, 7*(7), 1529-1544. doi: 10.1063/1.868540

Pelipenko, J., Kristl, J., Jankovic, B., Baumgartner, S., & Kocbek, P. (2013). The impact of relative humidity during electrospinning on the morphology and mechanical properties of nanofibers. *Int J Pharm, 456*(1), 125-134. doi: 10.1016/j.ijpharm.2013.07.078. Repéré à https://www.ncbi.nlm.nih.gov/pubmed/23939535

Plateau, J. (1873). *Experimental and Theoretical Statics of Liquids Subject to Molecular Forces Only*

Plog, J. P., Kulicke, W. M., & Clasen, C. (2005). Influence of the Molar Mass Distribution on the Elongational Behaviour of Polymer Solutions in Capillary Breakup. *Applied Rheology, 15*(1), 28-37. doi: 10.1515/arh-2005-0002

Ramakrishna, S., Fujihara, K., Teo, W.-E., Lim, T.-C., & Ma, Z. (2005). Chapter 3 Electrospinning Process. Dans *An Introduction to Electrospinning and Nanofibers* (pp. 90-154). doi: 10.1142/9789812567611_0003. Repéré à https://www.worldscientific.com/doi/abs/10.1142/9789812567611_0003

Rayleigh, L. (1878). On The Instability Of Jets. *Proceedings of the London Mathematical Society, s1-10*(1). doi: https://doi.org/10.1112/plms/s1-10.1.4

Reneker, D. H., & Yarin, A. L. (2008). Electrospinning jets and polymer nanofibers. *Polymer, 49*(10), 2387-2425. doi: 10.1016/j.polymer.2008.02.002

Reneker, D. H., Yarin, A. L., Fong, H., & Koombhongse, S. (2000). Bending instability of electrically charged liquid jets of polymer solutions in electrospinning. *Journal of Applied Physics, 87*(9), 4531-4547. doi: 10.1063/1.373532

Riazi, K., Abbasi, M., Klein, C. O., Naue, I. F. C., & Wilhelm, M. (2020). Quantifying separation energy with a modified Capillary Break-up Extensional Rheometer (CaBER) to study polymer solutions. *Soft Materials, 19*(2), 199-212. doi: 10.1080/1539445x.2020.1792929

Robertson, B. P., & Calabrese, M. A. (2022). Evaporation-controlled dripping-onto-substrate (DoS) extensional rheology of viscoelastic polymer solutions. *Sci Rep, 12*(1), 4697. doi: 10.1038/s41598-022-08448-x. Repéré à https://www.ncbi.nlm.nih.gov/pubmed/35304499

Robinson, A. J., Perez-Nava, A., Ali, S. C., Gonzalez-Campos, J. B., Holloway, J. L., & Cosgriff-Hernandez, E. M. (2021). Comparative Analysis of Fiber Alignment Methods in Electrospinning. *Matter, 4*(3), 821-844. doi: 10.1016/j.matt.2020.12.022. Repéré à https://www.ncbi.nlm.nih.gov/pubmed/35757372

Rodd, L. E., Scott, T. P., Cooper-White, J. J., & McKinley, G. H. (2005). Capillary Break-up Rheometry of Low-Viscosity Elastic Fluids. *Applied Rheology, 15*(1), 12-27. doi: 10.1515/arh-2005-0001

Rozali, S. N. M., Paterson, A. H. J., Hindmarsh, J. P., & Huffman, L. M. (2019). Understanding the shear and extensional properties of pomace-fibre suspensions prior to the spray drying process. *Lwt, 99*, 138-147. doi: 10.1016/j.lwt.2018.09.061

Rubinstein, M., & Colby, R. H. (2003). *Polymer Physics*. Oxford.

Rudd, J. F. (1960). The Effect of Molecular Weight Distribution on the Rheological Properties of Polystyrene. *Journal of Polymer Science, XLIV*, 459-474. doi: https://doi.org/10.1002/pol.1960.1204414417

Russell, S. J. (2007). *Handbook of Nonwovens*. The Textile Institute.

Sentmanat, M. L. (2004). Miniature universal testing platform: from extensional melt rheology to solid-state deformation behavior. *Rheologica Acta, 43*(6), 657-669. doi: 10.1007/s00397-004-0405-4

Shabaniverki, S., Alvarez-Valdivia, A., & Juárez, J. J. (2019). Portable imaging viscometry for quantitative complex fluid measurements. *Experimental Thermal and Fluid Science, 107*, 29-37. doi: 10.1016/j.expthermflusci.2019.05.009

Sousa, P. C., Vega, E. J., Sousa, R. G., Montanero, J. M., & Alves, M. A. (2017). Measurement of relaxation times in extensional flow of weakly viscoelastic polymer solutions. *Rheol Acta, 56*(1), 11-20. doi: 10.1007/s00397-016-0980-1. Repéré à https://www.ncbi.nlm.nih.gov/pubmed/32355366

Struglinski, M. J., & Graessley, W. W. (1985). Effects of polydispersity on the linear viscoelastic properties of entangled polymers. 1. Experimental observations for binary mixtures of linear polybutadiene. *Macromolecules, 18*(12), 2630-2643. doi: https://doi.org/10.1021/ma00154a046

Swift, A. (2018). *Development of a Smartphone App to Easily Measure Extensional Viscosity* (Honors Baccalaureate of Science in Chemical Engineering (Honors Scholar) thesis, Oregon State University, Honors College, Corvallis, OR).

Tang, X.-P., Si, N., Xu, L., & Liu, H.-Y. (2014). Effect of flow rate on diameter of electrospun nanoporous fibers. *Thermal Science, 18*(5), 1447-1449. doi: 10.2298/tsci1405447t

Taylor, S. G. (1964). Disintegration of water drops in an electric field. *Royal Society, 280*(1382). doi: https://doi.org/10.1098/rspa.1964.0151

Thermo Fisher Scientific Inc. (2007). *Thermo Scientific HAAKE CaBER™ 1: Quantifying extensional properties of fluids*. Karlsruhe, Germany.

Theron, S. A., Yarin, A. L., Zussman, E., & Kroll, E. (2005). Multiple jets in electrospinning: experiment and modeling. *Polymer, 46*(9), 2889-2899. doi: 10.1016/j.polymer.2005.01.054

Theron, S. A., Zussman, E., & Yarin, A. L. (2004). Experimental investigation of the governing parameters in the electrospinning of polymer solutions. *Polymer, 45*(6), 2017-2030. doi: 10.1016/j.polymer.2004.01.024

Thompson, C. J., Chase, G. G., Yarin, A. L., & Reneker, D. H. (2007). Effects of parameters on nanofiber diameter determined from electrospinning model. *Polymer, 48*(23), 6913-6922. doi: 10.1016/j.polymer.2007.09.017

Trijet Ltd. (2025). TriMaster Extensional Rheometer. Repéré le September 12, 2025 à https://trijet.co.uk/

Tripatanasuwan, S., Zhong, Z., & Reneker, D. H. (2007). Effect of evaporation and solidification of the charged jet in electrospinning of poly(ethylene oxide) aqueous solution. *Polymer, 48*(19), 5742-5746. doi: 10.1016/j.polymer.2007.07.045

Varesano, A., Carletto, R. A., & Mazzuchetti, G. (2009). Experimental investigations on the multi-jet electrospinning process. *Journal of Materials Processing Technology, 209*(11), 5178-5185. doi: 10.1016/j.jmatprotec.2009.03.003

Vinogradov, G. V., Yanovsky, Y. G., Titkova, L. V., Barancheeva, V. V., Sergeenkov, S. I., & Borisenkova, E. K. (1980). Viscoelastic properties of linear polymers in the fluid state and their transition to the high-elastic state. *Polymer Engineering & Science, 20*(17), 1138-1146. doi: https://doi.org/10.1002/pen.760201705

Wasserman, S. H., & Graessley, W. W. (1992). Effects of polydispersity on linear viscoelasticity in entangled polymer melts. *Journal of Rheology, 36*(4), 543-572. doi: 10.1122/1.550363

Wu, X.-F., Salkovskiy, Y., & Dzenisc, Y. A. (2011). Modeling of solvent evaporation from polymer jets in electrospinning. *Applied Physics Letters, 98*(22). doi: https://doi.org/10.1063/1.3585148

Xie, S., & Zeng, Y. (2012). Effects of Electric Field on Multineedle Electrospinning: Experiment and Simulation Study. *Industrial & Engineering Chemistry Research, 51*(14), 5336-5345. doi: 10.1021/ie2020763

Yan, G., Niu, H., & Lin, T. (2019). Needle-less Electrospinning. Dans *Electrospinning: Nanofabrication and Applications* (pp. 219-247). doi: 10.1016/b978-0-323-51270-1.00007-8

Yarin, A. L., Koombhongse, S., & Reneker, D. H. (2001a). Bending instability in electrospinning of nanofibers. *Journal of Applied Physics, 89*(5), 3018-3026. doi: 10.1063/1.1333035

Yarin, A. L., Koombhongse, S., & Reneker, D. H. (2001b). Taylor cone and jetting from liquid droplets in electrospinning of nanofibers. *Journal of Applied Physics, 90*(9), 4836-4846. doi: 10.1063/1.1408260

Yarin, A. L., Pourdeyhimi, B., & Ramakrishna, S. (2014a). *Fundamentals and Applications of Micro- and Nanofibers*. Cambridge University Press. doi: https://doi.org/10.1017/CBO9781107446830

Yarin, A. L., Pourdeyhimi, B., & Ramakrishna, S. (2014b). Melt- and solution blowing. Dans *Fundamentals and Applications of Micro and Nanofibers* (pp. 89-178). doi: 10.1017/cbo9781107446830.005

Ye, X., & Sridhar, T. (2005). Effects of the Polydispersity on Rheological Properties of Entangled Polystyrene Solutions. *Macromolecules, 38*(8), 3442-3449. doi: 10.1021/ma049642n

Ying Yang, Zhidong Jia, Qiang Li, Lei Hou, Jianan Liu, Liming Wang, . . . Markus Zahn. (2010). A Shield Ring Enhanced Equilateral Hexagon Distributed Multi-needle Electrospinning Spinneret. *IEEE Transactions on Dielectrics and Electrical Insulation, 17*(5), 1592-1601. doi: 1070-9878/10/

Yu, J. H., Fridrikh, S. V., & Rutledge, G. C. (2006). The role of elasticity in the formation of electrospun fibers. *Polymer, 47*(13), 4789-4797. doi: 10.1016/j.polymer.2006.04.050

Zheng, G., Jiang, J., Chen, D., Liu, J., Liu, Y., Zheng, J., . . . Li, W. (2019). Multinozzle high efficiency electrospinning with the constraint of sheath gas. *Journal of Applied Polymer Science, 136*(22). doi: 10.1002/app.47574

Zheng, G., Jiang, J., Wang, X., Li, W., Liu, J., Fu, G., & Lin, L. (2020). Nanofiber membranes by multi-jet electrospinning arranged as arc-array with sheath gas for electrodialysis applications. *Materials & Design, 189*. doi: 10.1016/j.matdes.2020.108504

Zhou, Y., Hu, Z., Du, D., & Tan, G. Z. (2018). The effects of collector geometry on the internal structure of the 3D nanofiber scaffold fabricated by divergent electrospinning. *The International Journal of Advanced Manufacturing Technology, 100*(9-12), 3045-3054. doi: 10.1007/s00170-018-2899-4

Zhu, Z., Wu, P., Wang, Z., Xu, G., Wang, H., Chen, X., . . . Liu, Z. (2019). Optimization of electric field uniformity of multi-needle electrospinning nozzle. *AIP Advances, 9*(10). doi: 10.1063/1.5111936

Zhu, Z., Xu, G., Chen, R., Wang, Z., Huang, J., Chen, X., . . . Li, Y. (2018). Uniform electric field enabled multi-needles electrospinning head based on trapezoid arrangement. *AIP Advances, 8*(8). doi: 10.1063/1.5026908

Zinelis, K., Abadie, T., McKinley, G. H., & Matar, O. K. (2024). The fluid dynamics of a viscoelastic fluid dripping onto a substrate. *Soft Matter, 20*(41), 8198-8214. doi: 10.1039/d4sm00406j. Repéré à https://www.ncbi.nlm.nih.gov/pubmed/39365107

Zuo, W., Zhu, M., Yang, W., Yu, H., Chen, Y., & Zhang, Y. (2005). Experimental study on relationship between jet instability and formation of beaded fibers during electrospinning. *Polymer Engineering & Science, 45*(5), 704-709. doi: 10.1002/pen.20304